Patrick Lainer, BSc

Numerical Treatment of Linearly Perturbed Ideal Magnetohydrodynamic Equilibria in a Tokamak

MASTER'S THESIS

to achieve the university degree of
Diplom-Ingenieur

Master's degree programme: Technische Physik

submitted to
Graz University of Technology

Supervisor
Ass.-Prof. Dipl.-Ing. Dr.techn. Winfried Kernbichler

Institute of Theoretical and Computational Physics

Co-Supervisor
Dipl.-Ing. Dr.rer.nat. Christopher Albert

Graz, September 2019

Eidesstattliche Erklärung

Ich erkläre an Eides statt, dass ich die vorliegende Arbeit selbstständig verfasst, andere als die angegebenen Quellen/Hilfsmittel nicht benutzt, und die den benutzten Quellen wörtlich und inhaltlich entnommenen Stellen als solche kenntlich gemacht habe. Das in TUGRAZonline hochgeladene Textdokument ist mit der vorliegenden Masterarbeit identisch.

Datum

Unterschrift

Affidavit

I declare that I have authored this thesis independently, that I have not used other than the declared sources/resources, and that I have explicitly indicated all material which has been quoted either literally or by content from the sources used. The text document uploaded to TUGRAZonline is identical to the present master's thesis.

Date

Signature

Kurzfassung

Plasmainstabilitäten sind von hoher Relevanz für Fusion mittels magnetischen Einschlusses. Von besonderer Bedeutung sind „edge-localized modes“ (ELMs) bei Tokamaks, die im „H mode“ betrieben werden. Ein Lösungsansatz zur Unterbindung dieser Art von Instabilitäten sind eigene Spulen („ELM mitigation coils“), die resonante magnetische Störungen erzeugen. Der damit verbundene erhöhte radiale Transport reduziert die Anzahl auftretender ELMs.

In der vorliegenden Arbeit wird das Modell der idealen Magnetohydrodynamik zugrundegelegt, um die Auswirkungen der „ELM mitigation coils“ auf eine gegebene Gleichgewichtskonfiguration zu simulieren. Mit Teilschritten basierend auf den Finite-Elemente-, Finite-Differenzen- und Finite-Volumen-Methoden wird ein vorkonditioniertes Iterationsschema zum Auffinden einer selbstkonsistenten Lösung entwickelt. Fourier-Entwicklung in toroidale Moden ermöglicht die Reduktion auf eine zweidimensionale Darstellung.

Ausgewählte Vergleichsfälle zeigen die Gültigkeit des iterativen Ansatzes und die Reproduzierbarkeit zuvor veröffentlichter Resultate, die unter Verwendung anderer Methoden entstanden sind. In Zukunft ist die Ergänzung kinetischer Codes mit dieser Methode denkbar, wodurch sich die Berechnungsdauer erheblich reduzieren ließe.

Abstract

Plasma instabilities constitute a significant concern in magnetic confinement fusion devices. The class of instabilities known as edge-localized modes (ELMs) is of particular importance to tokamaks operating in high-confinement mode. One approach to suppress these instabilities is the use of resonant magnetic perturbations (RMPs), enhancing radial transport and thus reducing the occurrence of ELMs. These RMPs are produced by separate ELM mitigation coils.

In this thesis, we use ideal magnetohydrodynamics to model the effect of ELM mitigation coils on a given equilibrium configuration. We develop a preconditioned iterative scheme that incorporates the finite element, finite difference, and finite volume methods to find a self-consistent solution. Fourier expansion in the toroidal direction allows us to reduce calculations to two dimensions.

Selected test cases demonstrate the validity of the iterative scheme and the reproduction of previously published results using different methods. In the future, this approach may be used to complement kinetic code, thereby reducing computation time considerably.

Contents

Introduction

The need for nuclear fusion energy has been well established. The tokamak concept, which is the basis of flagship projects like JET and ITER, still has problems controlling plasma instabilities like the *edge-localized modes* (ELMs). Application of *resonant magnetic perturbations* (RMPs) is one way to mitigate ELMs. To model RMPs fast and reliably, we need to understand how *magnetohydrodynamics* (MHD) and the more physically correct kinetics can complement each other. In this thesis, an iterative MHD approach based on the finite element, finite volume, and finite difference methods is used to self-consistently calculate the plasma response to an external perturbation. The resulting code with the tentative designation NEO-EQ may be used as a drop-in replacement of kinetic code where applicable, and conceivably as validation.

The content of this thesis is as follows. Chapter 1 serves as a short overview of the basic plasma physics concepts relevant to this thesis. The theory of MHD and its use in the description of specific plasma instabilities are introduced. In chapter 2, the task of this thesis is established, which is to compute the perturbation of a magnetohydrodynamic equilibrium. To this end, an iterative scheme including a preconditioner is developed. Chapter 3 describes the geometry of the tokamak device and discusses the consequences to the mathematical formalism. In this context, the substeps of the iterative scheme are elaborated in chapters 4 and 5. In chapter 6, some implementation choices and data sources for NEO-EQ code are described. Chapter 7 adds some special configurations which are used to test the validity of the presented approach. Chapter 8 shows selected results and their interpretation, including the aforementioned test cases. Finally, in chapter 9, the results and the possible applications are summarized.

Acknowledgement

First and foremost, I want to thank my supervisors Winfried Kernbichler and Christopher Albert whose perpetual advice, guidance, and patience made this thesis possible in the first place. I also want to thank Sergei Kasilov for sharing his immense knowledge, Rico Buchholz for the fruitful discussions, Philipp Ulbl for his support with test cases, and the other members of the plasma physics group for their input during group discussions. Furthermore, I am indebted to Admira Jaskić and Asmir Hrnić for additional proofreading, and my friends and family for moral support, especially when things did not work as intended (which was, frankly, quite often).

Без муке нема науке.

Chapter 1

Basic Plasma Physics

This chapter contains a short overview of plasma physics concepts that form the basis of this thesis. Since plasma physics is a broad field and derivations can be longwinded, we restrict ourselves to sketches and refer to literature instead of giving details here. As such, this chapter is based mostly on the monograph by Freidberg [5], albeit written in Gaussian units instead of SI units.

Plasma in the physical sense may be defined as matter that is made up of free ions and electrons that is nonetheless electrically neutral on a macroscopic scale. Besides this condition of *quasineutrality*, the *weak coupling* condition demands that the electrostatic Coulomb energy between the particles is lower than their kinetic energy so that Debye screening limits the influence of the local electric field to within the Debye length. This conditions can be fulfilled by a large set of values for density and temperature, ranging from rarefied astrophysical plasmas like the interstellar medium to the dense electron gas in metals. Typical values for thermonuclear plasmas in fusion devices are $n \approx 10^{14}\,\mathrm{cm}^{-3}$ and $k_\mathrm{B}T \approx 10^4\,\mathrm{eV}$.

The collective behavior arising from the interactions of the moving charged particles mediated by electric and magnetic fields becomes quite complex – no single theory can describe all plasma phenomena and is computationally tractable at the same time. The present thesis considers the theory of ideal *magnetohydrodynamics* (MHD), which is useful to determine the macroscopic stability of a plasma. To see how it relates to other models, we sketch its derivation via *kinetic theory*. In the non-relativistic limit, Newton's equations of motion describe the single-particle motion under the influence of the Lorentz force originating from external fields generated by other particles in the plasma. This picture already allows a description of particle drifts and confinement in toroidal geometry by consideration of their trajectories for a given configuration of magnetic and electric fields. While it is theoretically possible to set up the system of equations to fully describe the interaction of all particles among each other and with external fields, this approach is neither computationally feasible nor desirable – knowing the exact positions and velocities of each particle is not helpful in understanding their large-scale collective behavior. Instead, we opt for the same level of abstraction as in statistical

mechanics: We take ensemble averages of the electric and magnetic fields and describe the particles' positions and velocities by a *distribution function* $f_s(\boldsymbol{r}, \boldsymbol{v}, t)$. Here, $\boldsymbol{r}$ is position, $\boldsymbol{v}$ is velocity, and t is time, while s designates the particle species (ions and electrons). The distribution function is normalized to

$$\int_\Omega \mathrm{d}^3 r \int_{\mathbb{R}^3} \mathrm{d}^3 v f_s(\boldsymbol{r}, \boldsymbol{v}, t) = 1 \tag{1.1}$$

for any given time t. The time evolution of f_s is given by the kinetic equation

$$\frac{\partial f_s(\boldsymbol{r}, \boldsymbol{v}, t)}{\partial t} + \boldsymbol{v} \cdot \nabla_{\boldsymbol{r}} f_s(\boldsymbol{r}, \boldsymbol{v}, t) + \frac{q_s}{m_s}\left(\boldsymbol{E} + \frac{1}{c}\boldsymbol{v} \times \boldsymbol{B}\right) \cdot \nabla_{\boldsymbol{v}} f_s(\boldsymbol{r}, \boldsymbol{v}, t) = \left(\frac{\partial f_s(\boldsymbol{r}, \boldsymbol{v}, t)}{\partial t}\right)_{\text{coll}}, \tag{1.2}$$

where the term on the right-hand side is the *collision term* modelling Coulomb collisions. q_s and m_s are the charge and mass of the particle species s, respectively. The plasma kinetic equations forms the basis for kinetic theory which is able to account for a wide array of particle effects within the plasma. To derive the fluid description of magnetohydrodynamics, we have to take moments of the distribution function, i.e., we integrate over velocity space with appropriate weights.

1.1 Ideal Magnetohydrodynamics

With the total number n_{0s} of particles of species s, we derive the number density as a zeroth moment:

$$n_s(\boldsymbol{r}, t) = n_{0s} \int_{\mathbb{R}^3} f_s(\boldsymbol{r}, \boldsymbol{v}, t)\, \mathrm{d}^3 v. \tag{1.3}$$

The charge density and mass density simply follow as $\rho_{ms} = m_s n_s$ and $\rho_{qs} = q_s n_s$, respectively. As a first moment, we get the particle flux density

$$\boldsymbol{\Gamma}_s(\boldsymbol{r}, t) = n_{0s} \int_{\mathbb{R}^3} f_s(\boldsymbol{r}, \boldsymbol{v}, t) \boldsymbol{v}\, \mathrm{d}^3 v, \tag{1.4}$$

from which the particle velocity

$$\boldsymbol{V}_s(\boldsymbol{r}, t) = \frac{\boldsymbol{\Gamma}_s(\boldsymbol{r}, t)}{n_s(\boldsymbol{r}, t)} \tag{1.5}$$

and current density

$$\boldsymbol{J}_s(\boldsymbol{r}, t) = q_s \boldsymbol{\Gamma}_s = q_s n_s \boldsymbol{V}_s \tag{1.6}$$

follow. Taking the second moment gives the pressure tensor as

$$\boldsymbol{p}_s(\boldsymbol{r}, t) = n_{0s} m_s \int_{\mathbb{R}^3} f_s(\boldsymbol{r}, \boldsymbol{v}, t)(\boldsymbol{v} - \boldsymbol{V}_s)(\boldsymbol{v} - \boldsymbol{V}_s)\, \mathrm{d}^3 v = n_{0s} m_s \int_{\mathbb{R}^3} f_s(\boldsymbol{r}, \boldsymbol{v}, t) \boldsymbol{v}\boldsymbol{v}\, \mathrm{d}^3 v - m_s n_s \boldsymbol{V}_s \boldsymbol{V}_s, \tag{1.7}$$

which reduces to $p_s = p_s I$ in an isotropic medium, where I is the unit tensor. The latter is assumed when the plasma is dominated by collisions so that the distribution function takes the form of the Maxwell distribution in velocity space. While most plasmas of interest are not in thermodynamic equilibrium, the approximation is good enough for our needs and ideal MHD also gives reasonable results when the assumption does not apply. Now, taking moments of the kinetic equation yields the time evolution of the fluid quantities derived above. Taking the zeroth moment gives

$$\frac{\partial}{\partial t}\int_{\mathbb{R}^3} f_s \,\mathrm{d}^3v + \nabla_{\boldsymbol{r}} \cdot \int_{\mathbb{R}^3} \boldsymbol{v} f_s \,\mathrm{d}^3v + \frac{q_s}{m_s}\int_{\mathbb{R}^3} \nabla_{\boldsymbol{v}} \cdot \left(\boldsymbol{E} + \frac{1}{c}\boldsymbol{v}\times\boldsymbol{B}\right) f_s \,\mathrm{d}^3v = \int_{\mathbb{R}^3}\left(\frac{\partial f_s}{\partial t}\right)_{\text{coll}} \mathrm{d}^3v. \quad (1.8)$$

The third integral term on the left-hand side vanishes after application of the divergence theorem because the distribution function vanishes at infinite velocity. Likewise, the integral of the collision term vanishes due to particle conservation. Expressing the remaining two integrals by fluid quantities yields

$$\frac{\partial n_s}{\partial t} + \nabla\cdot(n_s \boldsymbol{V}_s) = 0, \quad (1.9)$$

which we identify as continuity equation. Taking the first moment results in

$$\frac{\partial}{\partial t}\int_{\mathbb{R}^3} \boldsymbol{v} f_s \,\mathrm{d}^3v + \nabla_{\boldsymbol{r}} \cdot \int_{\mathbb{R}^3} \boldsymbol{v}\boldsymbol{v} f_s \,\mathrm{d}^3v + \frac{q_s}{m_s}\int_{\mathbb{R}^3} \boldsymbol{v}\nabla_{\boldsymbol{v}} \cdot \left(\boldsymbol{E} + \frac{1}{c}\boldsymbol{v}\times\boldsymbol{B}\right) f_s \,\mathrm{d}^3v = \\ = \int_{\mathbb{R}^3} \boldsymbol{v}\left(\frac{\partial f_s}{\partial t}\right)_{\text{coll}} \mathrm{d}^3v = \boldsymbol{R}_s. \quad (1.10)$$

Here, $\boldsymbol{R}_s$ is constrained by $\sum_s \boldsymbol{R}_s = \boldsymbol{0}$. Using integration by parts for the third integral on the left-hand side and some more rearrangement, we get the momentum equation

$$m_s n_s\left(\frac{\partial \boldsymbol{V}_s}{\partial t} + \boldsymbol{V}_s\cdot\nabla\boldsymbol{V}_s\right) + \nabla\cdot p_s - q_s n_s\left(\boldsymbol{E} + \frac{1}{c}\boldsymbol{V}_s\times\boldsymbol{B}\right) = \boldsymbol{R}_s. \quad (1.11)$$

Now, the continuity equation connects a zeroth moment (n_s) to a first moment ($\boldsymbol{V}_s$), the momentum equation connects both to a second moment (p_s), and so on. This hierarchy of equations has to be truncated at some point to give a closed set of equations, which will be discussed later. To complete the picture of two-fluid MHD, we have to consider Maxwell's equations:

$$\nabla\cdot\boldsymbol{E} = 4\pi\rho_q = 4\pi e(n_i - n_e), \quad (1.12)$$

$$\nabla\cdot\boldsymbol{B} = 0, \quad (1.13)$$

$$\nabla\times\boldsymbol{E} = -\frac{1}{c}\frac{\partial\boldsymbol{B}}{\partial t}, \quad (1.14)$$

$$\nabla\times\boldsymbol{B} = \frac{4\pi}{c}\boldsymbol{J} + \frac{1}{c}\frac{\partial\boldsymbol{E}}{\partial t} = \frac{4\pi}{c}e(n_i\boldsymbol{V}_i - n_e\boldsymbol{V}_e) + \frac{1}{c}\frac{\partial\boldsymbol{E}}{\partial t}. \quad (1.15)$$

Here, we already used fluid quantities with indices i and e for ions (with an implicit atomic number of $Z = 1$) and electrons, respectively. Now, we can make some simplifications. First, quasineutrality implies $n_e = n_i = n$, so the right-hand side of eq. (1.12) vanishes. Second, on the time scale considered in MHD, the fields are assumed to be static – such simulations typically recalculate fields from kinetic theory after a given time increment –, so we can neglect the time derivatives in Maxwell's equations. As a consequence, the current density is also divergence-free: $\nabla \cdot \boldsymbol{J} = 0$. Third, we reduce the two-fluid picture to a single-fluid picture:

$$\rho_m = m_e n_e + m_i n_i, \tag{1.16}$$

$$\boldsymbol{v} = \frac{m_e \boldsymbol{V}_e + m_i \boldsymbol{V}_i}{m_e + m_i}, \tag{1.17}$$

$$\boldsymbol{J} = \boldsymbol{J}_e + \boldsymbol{J}_i \tag{1.18}$$

$$T = \frac{T_e + T_i}{2}, \tag{1.19}$$

$$p = p_e + p_i = 2nT. \tag{1.20}$$

This also leads to a version of Ohm's law,

$$\boldsymbol{E} + \frac{1}{c}\boldsymbol{v} \times \boldsymbol{B} = \boldsymbol{0}. \tag{1.21}$$

Fourth, we close the moment equations by the adiabatic condition

$$\frac{\mathrm{d}}{\mathrm{d}t}\frac{p}{\rho_m^\gamma} = 0, \tag{1.22}$$

where γ is the adiabatic index. For a monoatomic gas, as is considered in fusion experiments, we have $\gamma = \frac{5}{3}$. Fifth, assuming electrons redistribute much faster than the timescale considered, no essential electric fields can build up in the plasma, and resistivity is effectively zero[1]. When we furthermore neglect the inertial term (the first term in eq. (1.11)), i.e., we assume a static solution, we finally arrive at the ideal MHD *force balance* equation:

$$c\nabla p = \boldsymbol{J} \times \boldsymbol{B}. \tag{1.23}$$

The interpretation is that the force resulting from the thermodynamic pressure gradient is balanced by the Lorentz force. This equation is the basis of the calculations in chapter 5.

[1] This is where the designation *ideal* comes from – non-ideal MHD considers effects caused by finite resistivity.

1.2 Flux Surfaces

Scalar multiplication of eq. (1.23) with the magnetic field or current density yields the important relations

$$\boldsymbol{B} \cdot \nabla p = \boldsymbol{J} \cdot \nabla p = 0, \tag{1.24}$$

which means that the current density and magnetic field lines lie on surfaces of constant pressure. They are in general not parallel to each other, but neither do they have a component perpendicular to these surfaces. By casting the magnetic field in Clebsch form given by eq. (3.25), we see that $\boldsymbol{B} \cdot \nabla \psi = 0$, so they are also surfaces of constant magnetic flux[1] ψ, which is why they are commonly called *flux surfaces*. Any quantity that is constant on a flux surface is called a *flux surface quantity* accordingly. Application of Hamiltonian theory to the differential equation determining magnetic field lines shows that *nested* flux surfaces appear in systems with axisymmetry, such as tokamaks. In the poloidal plane, these curves are described by the Grad–Shafranov equation

$$\Delta^* \psi = -B_\varphi \frac{\mathrm{d}B_\varphi}{\mathrm{d}\psi} - R^2 \frac{\mathrm{d}p}{\mathrm{d}\psi}, \tag{1.25}$$

where the differential operator Δ^* is defined as

$$\Delta^* \psi = R \frac{\partial}{\partial R} \left(\frac{1}{R} \frac{\partial \psi}{\partial R} \right) + \frac{\partial^2 \psi}{\partial R^2}, \tag{1.26}$$

making eq. (1.25) a nonlinear partial differential equation of second order. Note that due to the Shafranov shift, the nested flux surfaces are not concentric, but the *magnetic axis* – the innermost flux surface, degenerated to a point in the poloidal plane – is shifted outwards from the geometric center of the torus. Furthermore, usual tokamak configurations also have an *X point*[2], where the magnetic field lines cross, so that the flux surface is not closed. This flux surface is called the *separatrix*, and in our calculations, we only consider the plasma volume contained within the separatrix. We also speak of the *last closed flux surface* (LCFS) because we count the nested flux surfaces starting from the magnetic axis, going outward.

Now we shall consider an important flux surface quantity, the *safety factor* q. For every toroidal transit ($\Delta\varphi = 2\pi$), the magnetic field line traverses the poloidal angle $\Delta\vartheta$. The latter is averaged over a number of toroidal transits k to give the average rotational transform ι (lowercase iota):

$$\iota = \lim_{n \to \infty} \frac{1}{N} \sum_{k=1}^{N} \Delta\vartheta_k. \tag{1.27}$$

[1] For a detailed discussion, see section 3.1.

[2] The magnetic axis is also called *O point* by analogy.

The safety factor q is then defined by

$$q = \frac{2\pi}{\iota} \tag{1.28}$$

When the magnetic field line closes on itself after a finite number of toroidal transits, q is rational and the flux surface on which it attains that value is called a rational flux surface. In this case, more than one magnetic field line is necessary to trace out the flux surface. If q is irrational, the magnetic field line never closes on itself and will trace out the entire flux surface (given infinite time and ergodicity). Since the rational numbers are a dense subset of the real numbers, an irrational flux surface may be approximated arbitrarily close by a rational flux surface and vice versa. The actual values of q are relevant to the macroscopic stability of the plasma: q has to be larger than one over the entire plasma volume, and it has to be larger than two on the plasma edge. Otherwise, kink instabilities will appear. This shows that despite all the simplifications and assumptions, ideal MHD is useful to estimate macroscopic stability of the plasma.

Of particular concerns are the *edge-localized modes* (ELMs) that can appear in high-confinement mode or *H-mode*, the most common mode of tokamak operation. The radial pressure profile will steepen, and when it becomes too steep, the pressure gradient force ejects particles which are then lost from confinement and can damage the reactor wall. One approach to handle these instabilities is to utilize ELM mitigation coils which induce *resonant magnetic perturbations* (RMPs). These are non-axisymmetric perturbations to an otherwise axisymmetric MHD equilibrium configuration. A resonance appears at a flux surface with rational q corresponding to the ratio of the poloidal and toroidal mode numbers of the perturbation; for details see section 7.1. At the resonance, *tearing modes* and chains of narrow *magnetic islands* appear, across which particle transport is enhanced. This avoids the build-up of pressure and could be used to control ELMs. Ideal MHD cannot describe tearing modes and magnetic islands, but the inclusion of *sheet currents* from tearing mode theory, which we touch upon in section 5.3, alleviates this shortcoming somewhat.

Chapter 2

Stationary Linear Perturbation of Ideal MHD Equilibrium

In this chapter, we develop the equations that model the effect of a non-axisymmetric perturbation on an axisymmetric ideal MHD equilibrium, setting up the tasks for the next chapters. Section 2.1 introduces an iterative scheme to solve the equations in a self-consistent manner, while section 2.2 discusses its solution employing a preconditioner.

For the intended application on stationary (compared to MHD mode eigenfrequencies) non-axisymmetric magnetic perturbations by external coils, we consider a perturbed ideal MHD equilibrium for pressure p, currents $\boldsymbol{J}$ and magnetic field $\boldsymbol{B}$ fulfilling

$$\nabla p = \frac{1}{c}\boldsymbol{J} \times \boldsymbol{B}, \tag{2.1}$$

$$\nabla \times \boldsymbol{B} = \frac{4\pi}{c}\boldsymbol{J}, \tag{2.2}$$

$$\nabla \cdot \boldsymbol{B} = 0. \tag{2.3}$$

Starting with a given MHD equilibrium fulfilling eqs. (2.1) and (2.3) denoted by subscripts "0", linear order equations for an external magnetic perturbation (denoted by δ) split into a vacuum and a plasma part (subscript v and p, respectively) are

$$\nabla \delta p = \frac{1}{c}\left(\boldsymbol{J}_0 \times \delta\boldsymbol{B} + \delta\boldsymbol{J} \times \boldsymbol{B}_0\right), \tag{2.4}$$

$$\delta\boldsymbol{B} = \delta\boldsymbol{B}_\mathrm{v} + \delta\boldsymbol{B}_\mathrm{p}\,, \tag{2.5}$$

$$\delta\boldsymbol{B}_\mathrm{v} = \frac{1}{c}\oint \frac{I_\mathrm{c}(\boldsymbol{r}')\,\mathrm{d}\boldsymbol{l}' \times \boldsymbol{r}}{|\boldsymbol{r} - \boldsymbol{r}'|^3}, \tag{2.6}$$

$$\delta\boldsymbol{B}_\mathrm{p} = \nabla \times \delta\boldsymbol{A}, \tag{2.7}$$

$$\nabla \times (\nabla \times \delta\boldsymbol{A}) = \frac{4\pi}{c}\delta\boldsymbol{J}, \tag{2.8}$$

$$\Rightarrow \nabla \cdot \delta\boldsymbol{B} = \nabla \cdot \delta\boldsymbol{J} = 0. \tag{2.9}$$

Here the perturbation field in vacuum, $\delta \boldsymbol{B}_\mathrm{v}$, is pre-evaluated by a Biot–Savart integral over external[1] coil currents $I_\mathrm{c}(\boldsymbol{r}')$. This induces a plasma response, resulting in the current density perturbation $\delta \boldsymbol{J}$. The perturbation field from currents within the plasma, $\delta \boldsymbol{B}_\mathrm{p}$, is in turn computed from $\delta \boldsymbol{J}$, again giving rise to a plasma response current. Now, the linearized force balance eq. (2.4) is used to compute $\delta \boldsymbol{J}$ for given $\delta \boldsymbol{B}$ whereas eq. (2.8) yields $\delta \boldsymbol{B}_\mathrm{p}$ for given $\delta \boldsymbol{J}$.

The solution of eq. (2.4) can further be split into two steps: First the pressure perturbation δp is found, and then the plasma current density $\delta \boldsymbol{J}$ is computed using the condition $\nabla \cdot \delta \boldsymbol{J} = 0$. For an unperturbed equilibrium with nested flux surfaces, both steps can be performed in a radially local manner if a field-aligned computational grid is used, which will become clear in the following sections. Radial coupling happens by the combination of the two individual steps since their effective radial locations of computation are shifted by a half-step in radial grid distance.

Equation (2.4) and eq. (2.8) are solved in an alternating way until convergence is reached, as described in section 2.1. In addition, a preconditioner is used to enhance convergence, which we discuss in section 2.2. This approach is also used by Albert et al. [1].

2.1 Iteration Scheme

From eq. (2.4), we calculate the current perturbation[2] from a given magnetic field perturbation. This can be done with kinetic code (e.g., NEO-2) or with MHD, as is discussed in chapter 5. In either case, we can write the computation in compact form,

$$\delta \boldsymbol{J} = \hat{P} \delta \boldsymbol{B} = \hat{P} \left(\delta \boldsymbol{B}_\mathrm{v} + \delta \boldsymbol{B}_\mathrm{p} \right), \tag{2.10}$$

with an abstract operator $\hat{P}$ representing the computation. It acts on the full magnetic perturbation, that is the contribution from the vacuum field $\delta \boldsymbol{B}_\mathrm{v}$ produced by external coils and the plasma response field $\delta \boldsymbol{B}_\mathrm{p}$.

From a given current perturbation, eq. (2.8) is used to compute the plasma response field $\delta \boldsymbol{B}_\mathrm{p}$. This kind of problem is commonly solved with a finite element method, as described in chapter 4. In a similar manner as before, the operator $\hat{M}$ represents this calculation step:

$$\delta \boldsymbol{B}_\mathrm{p} = \hat{M} \delta \boldsymbol{J}. \tag{2.11}$$

Since we only take the current enclosed in the plasma volume into account, only the plasma response field $\delta \boldsymbol{B}_\mathrm{p}$ is affected. The external coils whose current produces the vacuum perturbation $\delta \boldsymbol{B}_\mathrm{v}$ are assumed to have infinite impedance so that we can neglect feedback from the plasma response. $\delta \boldsymbol{B}_\mathrm{v}$ is essentially fixed by eq. (2.6).

[1] i.e. entirely outside the plasma region

[2] and in an intermediate step, the pressure perturbation

Substituting $\delta \boldsymbol{J}$ from eq. (2.10) in eq. (2.11) and using a shorthand $\hat{K} = \hat{M}\hat{P}$ gives

$$\hat{K}\left(\delta \boldsymbol{B}_{\mathrm{v}} + \delta \boldsymbol{B}_{\mathrm{p}}\right) = \delta \boldsymbol{B}_{\mathrm{p}}, \tag{2.12}$$

$$\hat{K}\delta \boldsymbol{B}_{\mathrm{v}} = \left(\hat{1} - \hat{K}\right)\delta \boldsymbol{B}_{\mathrm{p}}, \tag{2.13}$$

$$\left(\hat{1} - \hat{K}\right)^{-1}\hat{K}\delta \boldsymbol{B}_{\mathrm{v}} = \delta \boldsymbol{B}_{\mathrm{p}}. \tag{2.14}$$

The first term can be rewritten in the form of a Neumann series, a generalisation of geometric series to operators, assuming the series converges:

$$\left(\hat{1} - \hat{K}\right)^{-1} = \sum_{k=0}^{\infty} \hat{K}^k. \tag{2.15}$$

This way a consistent solution for $\delta \boldsymbol{B}_{\mathrm{p}}$ can be computed from $\delta \boldsymbol{B}_{\mathrm{v}}$ by repeated application of $\hat{K}$, given explicitly by the infinite series

$$\delta \boldsymbol{B}_{\mathrm{p}} = \left(\hat{1} + \hat{K} + \hat{K}^2 + \cdots\right)\hat{K}\delta \boldsymbol{B}_{\mathrm{v}} = \sum_{k=1}^{\infty} \hat{K}^k \delta \boldsymbol{B}_{\mathrm{v}} = \sum_{k=1}^{\infty} \delta \boldsymbol{B}^{(k)}. \tag{2.16}$$

In eq. (2.16) each term is given by the recurrence relation

$$\delta \boldsymbol{B}^{(k+1)} = \hat{K}\delta \boldsymbol{B}^{(k)}. \tag{2.17}$$

Adding the vacuum field as the initial value,

$$\delta \boldsymbol{B}^{(0)} = \delta \boldsymbol{B}_{\mathrm{v}} \tag{2.18}$$

the series' terms are accumulated for the self-consistent solution:

$$\delta \boldsymbol{B} = \sum_{k=0}^{\infty} \delta \boldsymbol{B}^{(k)}. \tag{2.19}$$

Alternatively, eq. (2.12) can be expanded,

$$\delta \boldsymbol{B}_{\mathrm{p}} = \hat{K}\left(\delta \boldsymbol{B}_{\mathrm{v}} + \delta \boldsymbol{B}_{\mathrm{p}}\right) = \hat{K}\left(\delta \boldsymbol{B}_{\mathrm{v}} + \hat{K}\left(\delta \boldsymbol{B}_{\mathrm{v}} + \delta \boldsymbol{B}_{\mathrm{p}}\right)\right) = \cdots, \tag{2.20}$$

yielding a fixed-point iteration for $\delta \boldsymbol{B}$:

$$\delta \boldsymbol{B}^{[k+1]} = \hat{K}\delta \boldsymbol{B}^{[k]} + \delta \boldsymbol{B}_{\mathrm{v}}. \tag{2.21}$$

Compared to the previous approach, this one is cumulative, i.e., it immediately produces the next approximation of the full perturbation. In other words, it corresponds to the sequence of

partial sums of the previous infinite series:

$$\delta \boldsymbol{B}^{[\kappa]} = \sum_{k=0}^{\kappa} \delta \boldsymbol{B}^{(k)}. \tag{2.22}$$

For this to be consistent, the initial value is also given by the vacuum field,

$$\delta \boldsymbol{B}^{[0]} = \delta \boldsymbol{B}_{\mathrm{v}}. \tag{2.23}$$

For illustration, both approaches are compared side-by-side in table 2.1. Figure 2.1 additionally illustrates the substeps of each iteration step modelled by $\hat{K}$.

Table 2.1: Comparison of iteration with series (non-cumulative) and sequence (cumulative)

iteration step:	$\delta \boldsymbol{B}^{(k)} = \hat{K} \delta \boldsymbol{B}^{(k-1)}$	$\delta \boldsymbol{B}^{[k]} = \hat{K} \delta \boldsymbol{B}^{[k-1]} + \delta \boldsymbol{B}_{\mathrm{v}}$,
initial value:	$\delta \boldsymbol{B}^{(0)} = \delta \boldsymbol{B}_{\mathrm{v}}$	$\delta \boldsymbol{B}^{[0]} = \delta \boldsymbol{B}_{\mathrm{v}}$,
step 1:	$\delta \boldsymbol{B}^{(1)} = \hat{K} \delta \boldsymbol{B}^{(0)} = \hat{K} \delta \boldsymbol{B}_{\mathrm{v}}$	$\delta \boldsymbol{B}^{[1]} = \hat{K} \delta \boldsymbol{B}^{[0]} + \delta \boldsymbol{B}_{\mathrm{v}} = \hat{K} \delta \boldsymbol{B}_{\mathrm{v}} + \delta \boldsymbol{B}_{\mathrm{v}}$,
step 2:	$\delta \boldsymbol{B}^{(2)} = \hat{K} \delta \boldsymbol{B}^{(1)} = \hat{K}^2 \delta \boldsymbol{B}_{\mathrm{v}}$	$\delta \boldsymbol{B}^{[2]} = \hat{K} \delta \boldsymbol{B}^{[1]} + \delta \boldsymbol{B}_{\mathrm{v}} = \left(\hat{K}^2 + \hat{K} + \hat{I} \right) \delta \boldsymbol{B}_{\mathrm{v}}$,
explicit form:	$\delta \boldsymbol{B}^{(\kappa)} = \hat{K}^{\kappa} \delta \boldsymbol{B}_{\mathrm{v}}$	$\delta \boldsymbol{B}^{[\kappa]} = \sum_{k=0}^{\kappa} \hat{K}^k \delta \boldsymbol{B}_{\mathrm{v}}$,
full perturbation:	$\delta \boldsymbol{B} = \sum_{k=0}^{\infty} \hat{K}^k \delta \boldsymbol{B}_{\mathrm{v}}$	$\delta \boldsymbol{B} = \delta \boldsymbol{B}^{[\infty]}$,
full plasma response:	$\delta \boldsymbol{B}_{\mathrm{p}} = \sum_{k=1}^{\infty} \hat{K}^k \delta \boldsymbol{B}_{\mathrm{v}}$	$\delta \boldsymbol{B}_{\mathrm{p}} = \delta \boldsymbol{B}^{[\infty]} - \delta \boldsymbol{B}_{\mathrm{v}}$.

For the implementation of preconditioned iterations (see section 2.2), the cumulative approach is more convenient. To reproduce the intermediate summands, we use eq. (2.22) and arrive at

$$\delta \boldsymbol{B}^{(k)} = \delta \boldsymbol{B}^{[k]} - \delta \boldsymbol{B}^{[k-1]}. \tag{2.24}$$

2.2 Enhanced Convergence with Preconditioned Iterations

Both approaches outlined in section 2.1 hinge on the convergence of the Neumann series in eq. (2.15). The convergence criterion for the similar geometric series of scalars is not directly applicable to operators but to their corresponding spectrum of eigenvalues. Thus we shall now consider a discretized equation of finite dimension N.

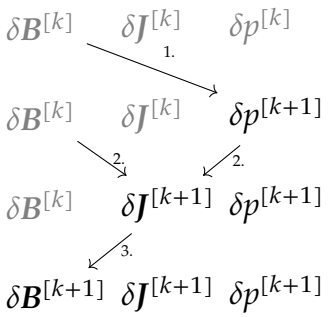

Figure 2.1: Individual steps within an iteration of $\hat{K}$. Grey symbols designate quantities from the previous iteration. Step 1 uses a finite difference method, outlined in section 5.1, to compute the next iteration of the pressure perturbation as an intermediary. Step 2 uses a finite volume method, discussed in section 5.2, to compute the next iteration of the current perturbation. Both are grouped together in $\hat{P}$ and solve the linearized MHD force balance. Step 3 then computes the magnetic field perturbation using the finite element method from chapter 4 to solve Ampère's equation represented by $\hat{M}$, completing the cycle.

We start from the fixed-point relation of the previous section which has the general form

$$\boldsymbol{x} = \hat{K}\boldsymbol{x} + \boldsymbol{x}_0. \tag{2.25}$$

$\boldsymbol{x}$ serves as a shorthand for $\delta \boldsymbol{B}$ and a reminder that the derivations in this section are not just valid for the specific problem of calculating magnetic fields. Similarly, $\boldsymbol{x}_0$ stands in for $\delta \boldsymbol{B}_\mathrm{v}$. Assuming the linear operator $\hat{K}$ is non-singular, we can formally write down an eigendecomposition

$$\hat{K} = \hat{V}\hat{\Lambda}\hat{V}^{-1}, \tag{2.26}$$

where $\hat{\Lambda}$ is a diagonal matrix with the eigenvalues,

$$\hat{\Lambda} = \begin{pmatrix} \lambda_1 & & & \\ & \lambda_2 & & \\ & & \ddots & \\ & & & \lambda_N \end{pmatrix} = \boldsymbol{\lambda}\hat{I}, \tag{2.27}$$

$\hat{V}$ contains the corresponding eigenvectors as its columns,

$$\hat{V} = (\boldsymbol{v}_1, \boldsymbol{v}_2, \dots, \boldsymbol{v}_N), \tag{2.28}$$

and $\hat{V}^{-1}$ is the inverse of $\hat{V}$. $\boldsymbol{x}$ can then be expressed in the eigenbasis with components x'_k,

$$\boldsymbol{x} = \sum_{k=1}^{N} x'_k \boldsymbol{v}_k = \hat{V}\boldsymbol{x}', \tag{2.29}$$

and transformed back to the original basis by the inverse,

$$\boldsymbol{x}' = \hat{V}^{-1}\boldsymbol{x}. \tag{2.30}$$

Rearranging eq. (2.25) to

$$\left(\hat{I} - \hat{K}\right)\boldsymbol{x} = \boldsymbol{x}_0, \tag{2.31}$$

multiplying from the left with $\hat{V}^{-1}$ and expanding in the eigenbasis yields

$$\Big(\underbrace{\hat{V}^{-1}\hat{I}\hat{V}}_{\hat{I}} - \hat{\Lambda}\Big)\boldsymbol{x}' = \boldsymbol{x}'_0. \tag{2.32}$$

Solving for $\boldsymbol{x}'$ gives

$$\boldsymbol{x}' = \left(\hat{I} - \hat{\Lambda}\right)^{-1}\boldsymbol{x}'_0 = \begin{pmatrix} \frac{1}{1-\lambda_1} & & & \\ & \frac{1}{1-\lambda_2} & & \\ & & \ddots & \\ & & & \frac{1}{1-\lambda_N} \end{pmatrix} \begin{pmatrix} x'_{01} \\ x'_{02} \\ \vdots \\ x'_{0N} \end{pmatrix}, \tag{2.33}$$

which can then be transformed back to the original basis. This approach yields a solution without resorting to series expansion and associated considerations of convergence, instead inverting the matrix directly. However, full diagonalization of $\hat{K}$ is computationally expensive, but partial diagonalization can be used to enhance convergence, or permit convergence at all, as will be seen below.

Applying the eigendecomposition to the operator series, we see that repeated application of $\hat{K}$ simplifies to

$$\hat{K}^n\boldsymbol{x}_0 = \underbrace{\left(\hat{V}\hat{\Lambda}\hat{V}^{-1}\right)\left(\hat{V}\hat{\Lambda}\hat{V}^{-1}\right)\cdots\left(\hat{V}\hat{\Lambda}\hat{V}^{-1}\right)}_{k}\boldsymbol{x}_0 = \hat{V}\hat{\Lambda}^n\hat{V}^{-1}\boldsymbol{x}_0 = \hat{V}\hat{\Lambda}^n\boldsymbol{x}'_0 = \sum_{k=1}^{N}\lambda_k^n x'_{0k}\boldsymbol{v}_k. \tag{2.34}$$

Comparing this to the solution in eq. (2.33), it becomes apparent that convergence of the Neumann operator series is equivalent to the convergence of the geometric series of all eigenvalues. Since the geometric series only converges for $|\lambda_k| < 1$ (and only reasonably fast for $|\lambda_k| \ll 1$), we need direct inversion for the largest eigenvalues, i.e. partial diagonalization. To find the largest eigenvalues, we use the Arnoldi method summarized in appendix B. This is a Krylov subspace method that reduces to the Lanczos method for Hermitian matrices and is also used as part of the generalized minimal residual method (GMRES). It does not involve matrix-matrix multiplication but only matrix-vector multiplication. Thus the linear operator needs not be given explicitly in matrix form, only its action on a given vector, which is fulfilled in our case for $\hat{K}$.

Using the Arnoldi method will give us good approximations to the largest r eigenvalues, denoted as $\boldsymbol{\lambda}_r$ or equivalently $\hat{\Lambda}_r$ and commonly called Ritz eigenvalues, as well as an or-

thonormal set of associated eigenvectors, this time arranged in an $N \times r$ matrix $\hat{V}_r$. The latter span the Krylov subspace of the full eigenspace. Instead of the eigenvalue equation of full rank,

$$\hat{K}\boldsymbol{v}_k = \lambda_k \boldsymbol{v}_k \quad \forall k = 1, 2, \dots, N, \tag{2.35}$$

or equivalently,

$$\hat{K}\hat{V} = \boldsymbol{\lambda}\hat{V} = \hat{V}\hat{\Lambda}, \tag{2.36}$$

we can write down the reduced eigenvalue equation in the Krylov subspace,

$$\hat{K}\hat{V}_r = \boldsymbol{\lambda}_r\hat{V}_r = \hat{V}_r\hat{\Lambda}_r. \tag{2.37}$$

Note that, compared to the eigenvalue equation in full space, the $r \times r$ matrix $\hat{\Lambda}_r$ has to be to the right of the $N \times r$ matrix $\hat{V}_r$.

With the largest r eigenvalues now known, we want to find a preconditioner that modifies the direct iteration step in eq. (2.25) so that the largest eigenvalues do not contribute. Usually, this is written by left-multiplying eq. (2.31) by the inverse of a full-rank linear operator:

$$\hat{\Pi}^{-1}\left(\hat{I} - \hat{K}\right)\boldsymbol{x} = \hat{\Pi}^{-1}\boldsymbol{x}_0. \tag{2.38}$$

We choose

$$\hat{\Pi}^{-1} = \hat{I} - \hat{A} \tag{2.39}$$

with some general matrix $\hat{A}$. Equation (2.38) then becomes

$$\left(\hat{I} - \hat{A} - \left(\hat{I} - \hat{A}\right)\hat{K}\right)\boldsymbol{x} = \left(\hat{I} - \hat{A}\right)\boldsymbol{x}_0, \tag{2.40}$$

which can be rearranged to resemble eq. (2.31),

$$\left(\hat{I} - \hat{\tilde{K}}\right)\boldsymbol{x} = \tilde{\boldsymbol{x}}_0, \tag{2.41}$$

with a modified iteration step

$$\hat{\tilde{K}} = \hat{A} + \left(\hat{I} - \hat{A}\right)\hat{K} \tag{2.42}$$

and a modified initial value

$$\tilde{\boldsymbol{x}}_0 = \left(\hat{I} - \hat{A}\right)\boldsymbol{x}_0. \tag{2.43}$$

By analogy, we can then write the explicit preconditioned iteration step as

$$\bar{\boldsymbol{x}}^{[k+1]} = \hat{\bar{K}}\bar{\boldsymbol{x}}^{[k]} + \bar{\boldsymbol{x}}_0. \tag{2.44}$$

Replacing the modified quantities on the right-hand side according to their definitions and rearranging gives

$$\bar{\boldsymbol{x}}^{[k+1]} = \hat{A}\bar{\boldsymbol{x}}^{[k]} + \left(\hat{I} - \hat{A}\right)\left(\hat{K}\bar{\boldsymbol{x}}^{[k]} + \boldsymbol{x}_0\right). \tag{2.45}$$

Now the last term in parentheses reproduces the direct, unmodified iteration yielding an unmodified $\boldsymbol{x}^{[k+1]}$,

$$\bar{\boldsymbol{x}}^{[k+1]} = \hat{A}\bar{\boldsymbol{x}}^{[k]} + \left(\hat{I} - \hat{A}\right)\boldsymbol{x}^{[k+1]}, \tag{2.46}$$

which can again be rearranged for a final result,

$$\bar{\boldsymbol{x}}^{[k+1]} = \boldsymbol{x}^{[k+1]} - \hat{A}\left(\boldsymbol{x}^{[k+1]} - \bar{\boldsymbol{x}}^{[k]}\right). \tag{2.47}$$

Compared to the direct iterations, only one additional matrix-vector multiplication is necessary, but see below for details.

Now, all we need is to compute $\hat{A}$. We required that the largest r eigenvalues do not contribute to iterations, so we demand

$$\hat{\bar{K}}\boldsymbol{v}_k \stackrel{!}{=} \boldsymbol{0} \quad \forall k \leq r. \tag{2.48}$$

This can be compactly rewritten and expanded via eqs. (2.37) and (2.42) to give

$$\hat{\bar{K}}\hat{V}_r = \hat{A}\hat{V}_r + \left(\hat{I} - \hat{A}\right)\hat{K}\hat{V}_r = \hat{A}\hat{V}_r + \left(\hat{I} - \hat{A}\right)\hat{V}_r\hat{\Lambda}_r \stackrel{!}{=} \hat{0}. \tag{2.49}$$

This can in turn be rearranged to

$$\hat{A}\hat{V}_r\left(\hat{\Lambda}_r - \hat{I}\right) \stackrel{!}{=} \hat{V}_r\hat{\Lambda}_r. \tag{2.50}$$

Right-multiplying with the inverse of $\hat{\Lambda}_r - \hat{I}$ yields

$$\hat{A}\hat{V}_r \stackrel{!}{=} \hat{V}_r\hat{\Lambda}_r\left(\hat{\Lambda}_r - \hat{I}\right)^{-1}. \tag{2.51}$$

Now $\hat{V}_r$ is not square and thus cannot be inverted, but we can add a unity term on the right-hand side:

$$\hat{A}\hat{V}_r \stackrel{!}{=} \hat{V}_r\hat{\Lambda}_r\left(\hat{\Lambda}_r - \hat{I}\right)^{-1}\left(\hat{V}_r^\dagger\hat{V}_r\right)^{-1}\hat{V}_r^\dagger\hat{V}_r. \tag{2.52}$$

By direct comparison it can be seen that a solution is given by

$$\hat{A} \equiv \hat{V}_r \hat{\Lambda}_r \left(\hat{\Lambda}_r - \hat{I}\right)^{-1} \left(\hat{V}_r^\dagger \hat{V}_r\right)^{-1} \hat{V}_r^\dagger. \tag{2.53}$$

The inner part can be grouped to the inverse of an $r \times r$ matrix $\hat{L}_r$,

$$\hat{L}_r = \hat{V}_r^\dagger \hat{V}_r \left(\hat{\Lambda}_r - \hat{I}\right). \tag{2.54}$$

This can then be conveniently inverted using the LAPACK routine `zgesv` to solve for $\hat{Y}$ in

$$\hat{L}_r \hat{Y} = \hat{I}. \tag{2.55}$$

Since $\hat{A}$ is constant during iterations, these computations would only need to be done once before preconditioned iterations start. Note that in practice though, $\hat{A}$ is not stored explicitly, since $r \ll N$ – in test runs, $r \approx 10^1, N \approx 10^5$. Instead of keeping N^2 entries of the dense matrix $\hat{A}$ in storage, we keep Nr entries of $\hat{V}_r$ and r^2 entries of $\hat{\Lambda}_r \hat{L}_r^{-1}$. Applying the matrices on a given $\boldsymbol{x}$ from right to left then requires additional matrix-vector multiplications, but in the worst case, this involves only $2Nr + r^2$ floating-point operations compared to N^2 for one matrix-vector multiplication with full $\hat{A}$. For an overview on matrix sizes, see table 2.2.

Table 2.2: Dimensions of quantities used in derivation of preconditioned iterations.

Quantity	Dimension
$\boldsymbol{x}$	N
$\boldsymbol{\lambda}_r$	r
$\boldsymbol{v}_k$	N
$\hat{\Lambda}_r$	$r \times r$
$\hat{V}_r$	$N \times r$
$\hat{V}_r^\dagger$	$r \times N$
$\hat{A}$	$N \times N$
$\hat{L}_r$	$r \times r$

It should be noted that the approximation error of the Ritz eigenvalues relative to the true eigenvalues decreases with the size of the Krylov subspace. This means that more Arnoldi iterations should be completed than is purely necessary for the expected number of eigenvalues with absolute value below a given threshold. Even if most of them are not used in the preconditioner, without sufficient accurcy in the largest eigenvalues the preconditioner will fail to assure convergence. As a rule of thumb, there should be 2 to 3 times as many Arnoldi iterations as there are Ritz eigenvalues used with the preconditioner.

Chapter 3

Geometrical Considerations

Even when the magnetic field is not axisymmetric, the cross-section retains its shape in tokamak devices, which stands in contrast to stellarator-type devices. It stands to reason to take the periodicity in the symmetry direction, i.e., the cylindrical angle φ, into account. The non-axisymmetric magnetic perturbation field in cylindrical coordinates (R, φ, Z) can then be expanded as a Fourier series:

$$\delta \boldsymbol{B}(R, \varphi, Z) = \sum_{n=-\infty}^{\infty} \boldsymbol{B}_n(R, Z) \mathrm{e}^{\mathrm{i}n\varphi} \tag{3.1}$$

Note that only the component functions are transformed; the basis vectors which generally depend on the transformation variable are unaffected. This means $\delta \boldsymbol{B}$ and $\boldsymbol{B}_n$ share the same geometrical basis.

As all equations are linear, a superposition of multiple harmonics is easily possible. Here we limit the analysis to an axisymmetric unperturbed equilibrium and a single toroidal perturbation harmonic

$$\delta \boldsymbol{B} = \mathrm{Re}(\boldsymbol{B}_n \mathrm{e}^{\mathrm{i}n\varphi}) \tag{3.2}$$

with fixed n and we use the same notation for other perturbed quantities. Note that $n \neq 0$; such a perturbation is necessarily small and considered part of the axisymmetric equilibrium. Thus an index 0 unambiguously refers to equilibrium quantities[1]. Also, since $\delta \boldsymbol{B}$ is real-valued, it follows that

$$\boldsymbol{B}_n = \boldsymbol{B}_{-n}^*, \tag{3.3}$$

where the asterisk denotes complex conjugation. Hence, only positive n are considered without loss of generality.

[1] This choice and further conventions are also listed in appendix A.2.

In axisymmetric coordinate systems, such as the aforementioned cylindrical system (R, φ, Z), eqs. (2.4) and (2.9) are to be solved for harmonics in the toroidal angle φ:

$$\nabla p_n + \mathrm{i}n p_n \nabla\varphi = \frac{1}{c}\left(\boldsymbol{J}_0 \times \boldsymbol{B}_n + \boldsymbol{J}_n \times \boldsymbol{B}_0\right), \tag{3.4}$$

$$\nabla \cdot \boldsymbol{J}_n^{\mathrm{pol}} + \mathrm{i}n J_n^{\varphi} = 0. \tag{3.5}$$

now with a two-dimensional ∇ operator acting in the poloidal (RZ) plane. The explicit definition depends on the coordinate system used and is outlined in section 3.1.

3.1 Coordinate Conventions

We generally follow the notational convention of D'haeseleer et al. [4], which we will succinctly summarize in this section. When using curvilinear coordinates in three-dimensional Euclidean space, two complementary vector bases can be defined. Using coordinates u^1, u^2, u^3, the basis vectors $\boldsymbol{e}_1, \boldsymbol{e}_2, \boldsymbol{e}_3$ are defined as tangent-basis vectors, which means they follow the coordinate curves at a given point $\boldsymbol{r}$:

$$\boldsymbol{e}_k(\boldsymbol{r}) = \frac{\partial \boldsymbol{r}}{\partial u^k}, \quad k = 1, 2, 3. \tag{3.6}$$

This means that the corresponding coordinate u^k is varied while the other two are held constant. Alternatively, the direction of a basis vector may be defined as a normal vector on the associated coordinate surface, i.e., where u^k is held constant, and the other two coordinates are varied. These reciprocal basis vectors are then related to the gradient:

$$\boldsymbol{e}^k(\boldsymbol{r}) = \nabla u^k(\boldsymbol{r}), \quad k = 1, 2, 3. \tag{3.7}$$

Note that with this definition, neither basis set is necessarily normalized or even orthogonal. They are however pairwise orthonormal by definition, so that

$$\boldsymbol{e}_i \cdot \boldsymbol{e}^j = \delta_i^j, \tag{3.8}$$

where the indices are kept in the same position with the Kronecker delta. As a consequence, the following relations between basis vectors are also given, where i, j, k is an even permutation:

$$\boldsymbol{e}_i = \frac{\boldsymbol{e}^j \times \boldsymbol{e}^k}{\boldsymbol{e}^i \cdot (\boldsymbol{e}^j \times \boldsymbol{e}^k)}, \quad \boldsymbol{e}^i = \frac{\boldsymbol{e}_j \times \boldsymbol{e}_k}{\boldsymbol{e}_i \cdot (\boldsymbol{e}_j \times \boldsymbol{e}_k)}. \tag{3.9}$$

An abstract vector $\boldsymbol{v}$ can be expanded in either basis, using the Einstein summation convention:

$$\boldsymbol{v} = (\boldsymbol{v} \cdot \boldsymbol{e}^k)\boldsymbol{e}_k = v^k \boldsymbol{e}_k, \quad \boldsymbol{v} = (\boldsymbol{v} \cdot \boldsymbol{e}_k)\boldsymbol{e}^k = v_k \boldsymbol{e}^k. \tag{3.10}$$

In the first case using tangent-basis vectors, the component v^k is called the contravariant component. In the second case using reciprocal basis vectors, the component v_k is called the covariant component. Conversion between the two bases is accomplished via the components of the metric tensor g,

$$v_i = g_{ij} v^j, \quad v^i = g^{ij} v_j, \tag{3.11}$$

where the summation convention is implicit and the metric tensor components are defined as

$$g_{ij} = \boldsymbol{e}_i \cdot \boldsymbol{e}_j, \quad g^{ij} = \boldsymbol{e}^i \cdot \boldsymbol{e}^j. \tag{3.12}$$

The determinant $g = \det \mathsf{g}$ of the metric tensor appears further in the following vector calculations and is related to the Jacobian J of the coordinate system defined by the u^k, again with i, j, k an even permutation:

$$J = \sqrt{g} = \sqrt{\det \mathsf{g}} = \boldsymbol{e}_i \cdot (\boldsymbol{e}_j \times \boldsymbol{e}_k). \tag{3.13}$$

With the nabla operator represented as

$$\nabla = \boldsymbol{e}^k \frac{\partial}{\partial u^k}, \tag{3.14}$$

the gradient follows:

$$\nabla \Phi = \frac{\partial \Phi}{\partial u^k} \boldsymbol{e}^k. \tag{3.15}$$

The divergence is most simply defined in terms of contravariant components,

$$\nabla \cdot \boldsymbol{v} = \frac{1}{\sqrt{g}} \frac{\partial}{\partial u^k} (\sqrt{g} v^k), \tag{3.16}$$

while the curl in its simplest form uses covariant components and returns contravariant components:

$$\nabla \times \boldsymbol{v} = \frac{\varepsilon_{ijk}}{\sqrt{g}} \frac{\partial v_j}{\partial u^i} \boldsymbol{e}_k. \tag{3.17}$$

Here, ε_{ijk} is the Levi–Cività symbol. On occasion, parallel or perpendicular components with respect to the magnetic field $\boldsymbol{B}$ are needed:

$$\boldsymbol{v}^{\parallel} = (\boldsymbol{v} \cdot \hat{\boldsymbol{B}}) \hat{\boldsymbol{B}} = (\boldsymbol{v} \cdot \boldsymbol{h}) \boldsymbol{h}, \tag{3.18}$$

$$\boldsymbol{v}^{\perp} = -\hat{\boldsymbol{B}} \times (\hat{\boldsymbol{B}} \times \boldsymbol{v}) = -\boldsymbol{h} \times (\boldsymbol{h} \times \boldsymbol{v}). \tag{3.19}$$

Here, $\hat{\boldsymbol{B}}$ denotes the unit vector of $\boldsymbol{B}$, but in the special case of the magnetic field, $\boldsymbol{h}$ may be used as well.

With these conventions set forth, we can define the necessary coordinate systems. We use two different right-handed coordinate systems, one cylindrical and one pseudotoroidal. As cylindrical coordinates we use (R, φ, Z) with φ running counter-clockwise as seen from above, so

$$x = R\cos\varphi, \quad y = R\sin\varphi, \quad z = Z. \tag{3.20}$$

These coordinates are used in computations and for meshes. They are orthogonal, as can be seen from the metric tensor, which is given by

$$g = \begin{pmatrix} 1 & 0 & 0 \\ 0 & R^2 & 0 \\ 0 & 0 & 1 \end{pmatrix}. \tag{3.21}$$

In general curvilinear coordinates, different basis vectors and vector components can have different physical dimensions depending on the coordinates used. Especially when dealing with numerical data, it would be desirable to use a representation with the "right" units and a normalized basis. In the given cylindrical coordinates, $\boldsymbol{e}_R$ and $\boldsymbol{e}_Z$ are normalized and equal to $\boldsymbol{e}^R$ and $\boldsymbol{e}^Z$ respectively, as are the corresponding components. In Cartesian coordinates, the basis vectors in toroidal direction are given by

$$\boldsymbol{e}_\varphi = R\cos\varphi\,\boldsymbol{e}_x + R\sin\varphi\,\boldsymbol{e}_y, \quad \boldsymbol{e}^\varphi = \frac{1}{R}\cos\varphi\,\boldsymbol{e}_x + \frac{1}{R}\sin\varphi\,\boldsymbol{e}_y. \tag{3.22}$$

These point in the same direction and are easily normalized. Taking into account these dimensions of the basis vectors, we can write the physical toroidal component as

$$B_{(\varphi)} = \frac{1}{R}B_\varphi = RB^\varphi, \tag{3.23}$$

where the parentheses signify that it is the physical component and not the covariant component. Note that eq. (3.23) is not necessarily true in other coordinate systems using the φ coordinate because $\boldsymbol{e}^\varphi$ and $\boldsymbol{e}_\varphi$ might not point in the same direction.

In regards to this coordinate system, we can characterize the experimental setup. When viewing the poloidal plane, $B_{0(\varphi)}$ points in the negative φ direction, the plasma current I_p points in the positive φ direction and the poloidal field $\boldsymbol{B}_0^\mathrm{pol}$ is going in the clockwise direction. Poloidal-toroidal decomposition of the equilibrium field $\boldsymbol{B}_0$ then yields the representation

$$\boldsymbol{B}_0 = \boldsymbol{B}_0^\mathrm{pol} + \boldsymbol{B}_0^\mathrm{tor}, \tag{3.24}$$

where

$$\boldsymbol{B}_0^\mathrm{pol} = \nabla\psi \times \nabla\varphi, \tag{3.25}$$

$$\boldsymbol{B}_0^\mathrm{tor} = B_{0\varphi}\nabla\varphi. \tag{3.26}$$

Here, ψ is the normalized *disc* poloidal flux, i.e.

$$\psi = \frac{1}{2\pi}\Psi_{\mathrm{pol}} = \frac{1}{2\pi}\int \boldsymbol{B}_0 \cdot \mathrm{d}\boldsymbol{S}, \tag{3.27}$$

where $\boldsymbol{S}$ is the disc that at a point of evaluation (R_S, Z_S) is given by $R \leq R_S, Z = Z_S$. The orientation of $\boldsymbol{S}$ fixes the sign[1] of ψ. Here, ψ is expected to increase towards the magnetic axis – ψ_{min} is located at the outermost flux surface and ψ_{max} is located at the magnetic axis. This leads to the following contravariant components for $\boldsymbol{B}_0^{\mathrm{pol}}$ in cylindrical coordinates (see also [12]):

$$B_0^R = (\nabla\psi \times \nabla\varphi)^R = -\frac{1}{R}\frac{\partial\psi}{\partial Z}, \tag{3.28}$$

$$B_0^Z = (\nabla\psi \times \nabla\varphi)^Z = \frac{1}{R}\frac{\partial\psi}{\partial R}. \tag{3.29}$$

Note that the toroidal field coils produce a magnetic field that is roughly proportional to $\frac{1}{R}$, so $B_{0\varphi}$ is assumed to be constant over the entire plasma volume.

The second set of coordinates represent a distorted pseudotoroidal system used as symmetry flux coordinates for derivations in sections 6.2 and 7.1. We keep the toroidal angle φ, but the poloidal plane is spanned by a pseudoradial *flux surface label* ϱ centered at the magnetic axis and a poloidal angle ϑ. ϱ and ϑ are chosen so that magnetic field lines are straight in these coordinates, requiring the solution of a *magnetic differential equation* involving $\boldsymbol{B}_0$. As a consequence, ϑ is not a geometric angle by itself, but there is a one-to-one correspondence with the poloidal angle in an elementary geometric sense. On the other hand, ϱ can be any quantity that is constant on a flux surface and strictly monotonous in the radial direction. While it is common to use ψ as the flux surface label, for derivations, we keep the more intuitive notation of D'haeseleer et al. [4] where ϱ is increasing towards the outside of the torus, i.e., $\varrho = -\psi$. With ϑ pointing in the counter-clockwise direction, $(\varrho, \varphi, \vartheta)$ constitutes a right-hand system. While this deviates from D'haeseleer et al. [4], where $\zeta = \frac{\pi}{2} - \varphi$ is used instead, it is consistent with the COCOS 3 convention of Sauter et al. [12], where an overview of possible combinations of coordinates are considered along with conversion between these choices and a procedure to check the consistency. As a consequence, the safety factor q is positive, and one of a few equivalent definitions is

$$q = \frac{B_0^\varphi}{B_0^\vartheta}. \tag{3.30}$$

The sign of q describes the sign of the helicity in (φ, ϑ) and can be explicitly computed as

[1] Since $\boldsymbol{B}_0$ is not defined outside the plasma volume and only $\nabla\psi$ enters calculations, ψ is defined up to a constant and thus could be shifted to change sign. However, the sign of $\nabla\psi$ is fixed.

described in section 6.3. The Jacobian of symmetry flux coordinates $(\varrho, \varphi, \vartheta)$ is

$$\sqrt{g} = \frac{-1}{B_0^\vartheta} = -\frac{q}{B_0^\varphi} = -\frac{qR^2}{B_{0\varphi}}. \tag{3.31}$$

The change of sign in comparison to D'haeseleer et al. [4] is due to the reversed toroidal angle. This way, $\sqrt{g}$ is still positive.

For the sake of completeness and since it will be used extensively in chapter 5, the ∇ operator shall be given explicitly for the gradient and divergence in cylindrical coordinates:

$$\nabla\Phi = \frac{\partial\Phi}{\partial R}\boldsymbol{e}^R + \frac{\partial\Phi}{\partial\varphi}\boldsymbol{e}^\varphi + \frac{\partial\Phi}{\partial Z}\boldsymbol{e}^Z, \tag{3.32}$$

$$\nabla\cdot\boldsymbol{v} = \frac{1}{R}\frac{\partial}{\partial R}(Rv^k) + \frac{\partial}{\partial\varphi}v^\varphi + \frac{1}{R}\frac{\partial}{\partial Z}(Rv^Z). \tag{3.33}$$

In the last term, a factor of R is kept for the sake of symmetry. Now, when we apply the Fourier transform $\frac{\partial}{\partial\varphi} \to \mathrm{i}n$, we get

$$\nabla\Phi = \frac{\partial\Phi_n}{\partial R}\boldsymbol{e}^R + \mathrm{i}n\Phi_n\boldsymbol{e}^\varphi + \frac{\partial\Phi_n}{\partial Z}\boldsymbol{e}^Z, \tag{3.34}$$

$$\nabla\cdot\boldsymbol{v} = \frac{1}{R}\frac{\partial}{\partial R}(Rv_n^k) + \mathrm{i}nv_n^\varphi + \frac{1}{R}\frac{\partial}{\partial Z}(Rv_n^Z). \tag{3.35}$$

For convenience, we will sometimes use the ∇ operator in two-dimensional form as a notational shorthand with the gradient:

$$\nabla\Phi = \nabla\Phi_n + \mathrm{i}n\Phi_n\boldsymbol{e}^\varphi. \tag{3.36}$$

It should be clear from context wheter ∇ is supposed to be two- or three-dimensional. For example, in $\nabla\varphi$ it is three-dimensional since $\nabla\varphi$ only has a toroidal component, while for purely poloidal quantities like $\nabla\psi$ or ∇p_n, two-dimensional and three-dimensional ∇ yield the same result.

In some derivations, we also use a Fourier series expansion for the poloidal angle ϑ with poloidal mode number m, i.e.

$$\boldsymbol{B}_n(\varrho,\vartheta) = \sum_{m=-\infty}^{\infty}\boldsymbol{B}_{mn}(\varrho)\mathrm{e}^{\mathrm{i}m\vartheta}. \tag{3.37}$$

In contrast to expansion in toroidal modes, poloidal modes are not fully linearly independent and *mode coupling* will occur due to to the toroidal geometry. Also, since the expansion is applied to generally complex Fourier coefficients $\boldsymbol{B}_n$, eq. (3.3) cannot be applied and negative m have to be considered as well. Using ϑ directly incurs solving the magnetic differential equation, whereas little is gained due to linear dependence. Nevertheless, it is useful in analytic derivations.

Lastly, we shall introduce the *flux surface average* for an arbitrary quantity Φ in a toroidal system, which D'haeseleer et al. [4] define as

$$\langle \Phi \rangle = \frac{\int_0^{2\pi} \int_0^{2\pi} \sqrt{g} \Phi \, \mathrm{d}\varphi \, \mathrm{d}\vartheta}{\int_0^{2\pi} \int_0^{2\pi} \sqrt{g} \, \mathrm{d}\varphi \, \mathrm{d}\vartheta}. \tag{3.38}$$

3.2 Discretization and Local Coordinate System

So far, we have given a fairly general description of the problem without explicit reference to numerical methods, apart maybe from the iteration scheme in section 2.1. One necessary modification is the discretization of the problem. The finite element method outlined in chapter 4 uses a discretization of the computational domain, i.e., it introduces a triangular grid. While other tilings are possible, triangulation is the simplest, and for triangles, the Delaunay algorithm is unique. The latter maximizes the triangles' minimal interior angle, which is desirable because a more elongated triangle shape reduces the quality of approximations on it. However, we choose to align the grid on flux surfaces in order to use the associated special properties.

We choose a set of nested flux surfaces, e.g., a number n_{flux} of curves of constant ψ, which are equidistant between the magnetic axis and the X point. These are then intersected by rays originating from the magnetic axis. Note that these rays are not curves of constant ϑ, as these are generally not straight in (R, Z) coordinates. As a result, between any two flux surfaces there is a *ring* or *strip* of quadrangles going around in poloidal direction. These quadrangles are then diagonally split into triangles, yielding two different types of triangles: One has two points on the outer and one point on the inner flux surface, the other has one point on the inner and two points on the outer flux surface. An exception is the innermost ring containing the magnetic axis, where there is only one type of triangles and no quadrangles to split. This kind of grid is depicted in fig. 3.1 where concentric circles are used to illustrate the nested flux surfaces.

For reasons that will become more apparent in sections 5.2 and 7.1, we use symbolic names instead of numbers to refer to edges and nodes. In the implementation, these names are mapped to their numerical index (see chapter 6). The label f designates the edge that approximates the flux surface, i.e., it is parallel to the flux surface in the infinitesimal limit. The labels i and o are chosen so that some flux is imagined to enter the triangle at edge i and exit at edge o, again entering the next triangle through edge i and so on, going around the ring in poloidal direction. The nodes are labeled by the corresponding uppercase letter of the opposite edge. These labels are also annotated in fig. 3.1. Note that the labels are necessarily local to each triangle.

Furthermore, for each edge we use a local orthogonal coordinate system on each triangle edge with $\boldsymbol{l}$ the vector of length l along the edge in counter-clockwise orientation, $\boldsymbol{n}$ the outward

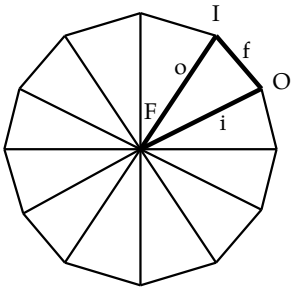

(a) The innermost triangle strip of the grid with the magnetic axis at its center. Edge f lies on the flux surface in the infinitesimal limit.

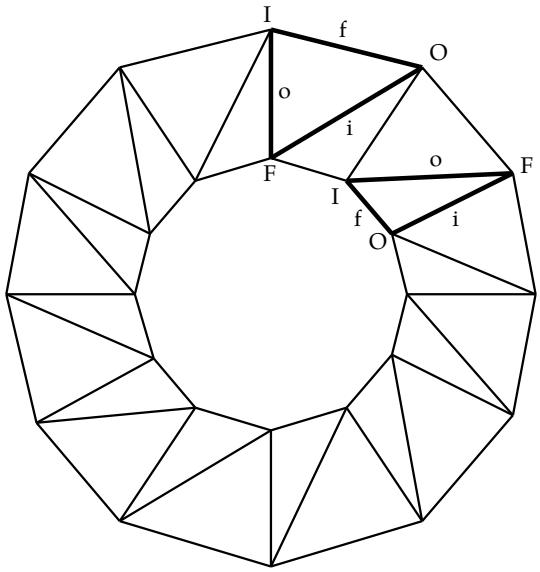

(b) One of the outer triangle strips of the grid with two alternating kinds of triangles with edge f lying on the inner and outer flux surface respectively.

Figure 3.1: The 2D mesh is given by a triangulation of poloidal cross-sections of the nested flux surfaces, resulting in rings. The cross-sections are assumed to be circular for illustration purposes.

normal of length l and $\nabla\varphi$ pointing inside the plane. We obtain relations

$$\boldsymbol{l} \times \boldsymbol{n} = l^2 R \nabla\varphi, \tag{3.39}$$

$$\boldsymbol{n} \times R\nabla\varphi = \boldsymbol{l}, \tag{3.40}$$

$$R\nabla\varphi \times \boldsymbol{l} = \boldsymbol{n}. \tag{3.41}$$

This is illustrated for a small sector on one ring in fig. 3.2.

Since edge f is approximated to lie on the flux surface, some properties carry over. In particular, since flux surfaces are surfaces of constant ψ and p_0, in the infinitesimal limit we have

$$\boldsymbol{n}_\mathrm{f} \parallel \nabla\psi \parallel \nabla p_0, \tag{3.42}$$

as well as

$$\boldsymbol{B}_0 \cdot \boldsymbol{n}_\mathrm{f} = 0, \quad \boldsymbol{J}_0 \cdot \boldsymbol{n}_\mathrm{f} = 0. \tag{3.43}$$

Likewise, it should be noted that $\nabla\varphi$ is perpendicular to all purely poloidal quantities which includes, apart from those designated with superscript "pol", all local coordinate vectors $\boldsymbol{l}$ and $\boldsymbol{n}$, Fourier coefficients with subscript n, as well as $\nabla\psi$ and ∇p_0.

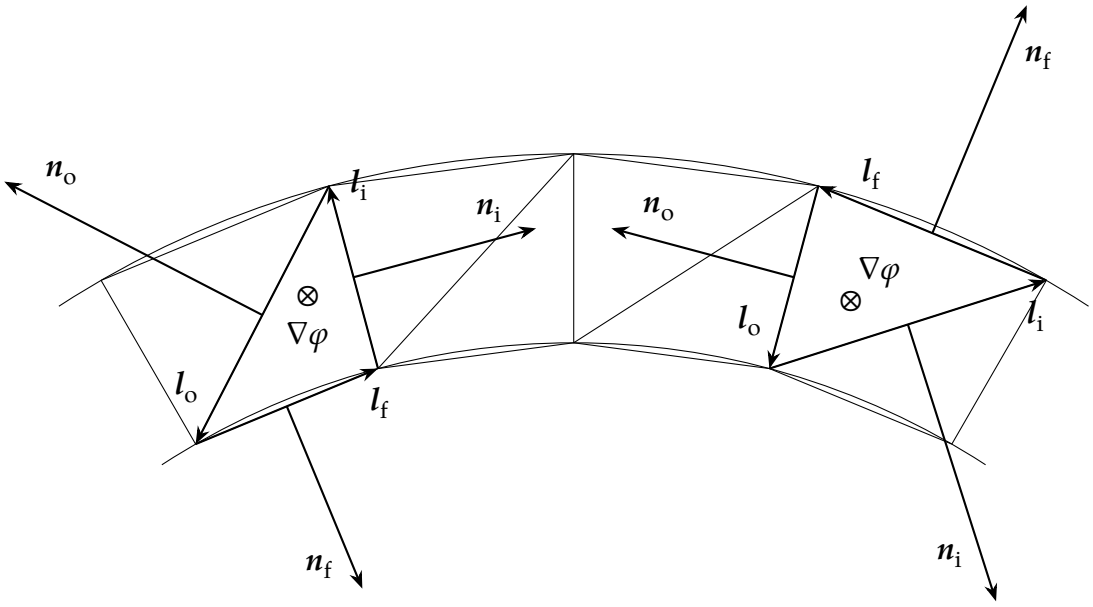

Figure 3.2: Schematic of the local coordinate system.

3.3 Representation of Fields on the Grid

Another approximation made in the finite element method is the choice of a *basis* to represent a scalar or vector field locally on one element of the grid. Scalar fields like the pressure perturbation can be approximated with Lagrange elements of the lowest order where the *degrees of freedom* are the values on the nodes, and any value within the triangle is interpolated from the values of its nodes. Many other choices are available, but this is the simplest option to implement, and it is sufficient for our needs. For vector fields, some more considerations are necessary; see chapter 4 for more details. We are mostly interested in the representation of the magnetic flux density and the current density, both of which characteristically show zero divergence. Thus it is necessary to choose a basis that yields a well-defined divergence. This is guaranteed by Raviart–Thomas elements, where, in the lowest-order case, the degrees of freedom are the fluxes of the vector field across the triangle edges:

$$\Psi_k = \int_{\Gamma_k} R\boldsymbol{B}_n^{\mathrm{pol}} \cdot \hat{\boldsymbol{n}}\,\mathrm{d}l \approx R(\Gamma_k)\boldsymbol{B}_n^{\mathrm{pol}}(\Gamma_k) \cdot \boldsymbol{n}_k, \tag{3.44}$$

$$I_k = \int_{\Gamma_k} R\boldsymbol{J}_n^{\mathrm{pol}} \cdot \hat{\boldsymbol{n}}\,\mathrm{d}l \approx R(\Gamma_k)\boldsymbol{J}_n^{\mathrm{pol}}(\Gamma_k) \cdot \boldsymbol{n}_k. \tag{3.45}$$

There are a few things to note here. Firstly, the factor R is included due to the metric in cylindrical coordinates and the fact that the integrand derives from the divergence theorem. Secondly, $\hat{\boldsymbol{n}}$ is normalized, but $\boldsymbol{n}$ is not, so the length of the edge is included as a factor. Lastly, the integral is approximated by evaluation at only a single point, the edge midpoint Γ_k. Conversely, to interpolate the value at given point $\boldsymbol{r}$ within a triangle, each degree of freedom Ψ_k or I_k is multiplied by the vectorial basis formed by the vector connecting $\boldsymbol{r}$ and the node

opposing edge k, weighted with the triangle area S_Ω:

$$\boldsymbol{B}_n(\boldsymbol{r}) = \frac{\Psi_\mathrm{f}(\boldsymbol{r}-\boldsymbol{r}_\mathrm{F}) + \Psi_\mathrm{i}(\boldsymbol{r}-\boldsymbol{r}_\mathrm{I}) + \Psi_\mathrm{o}(\boldsymbol{r}-\boldsymbol{r}_\mathrm{O})}{2S_\Omega}, \tag{3.46}$$

$$\boldsymbol{J}_n(\boldsymbol{r}) = \frac{I_\mathrm{f}(\boldsymbol{r}-\boldsymbol{r}_\mathrm{F}) + I_\mathrm{i}(\boldsymbol{r}-\boldsymbol{r}_\mathrm{I}) + I_\mathrm{o}(\boldsymbol{r}-\boldsymbol{r}_\mathrm{O})}{2S_\Omega}, \tag{3.47}$$

Note that the value is well-defined only within the triangle but not on the edge: while the flux across the edge, i.e. the normal component of the field is consistent with the neighbouring triangle, the component *along* the edge is not necessarily continuous across triangles.

On a general note, we indicate the point of evaluation in parentheses after the field in question: $\boldsymbol{r}^{(k)}$ refers to the node with number k, as in $p_n(\boldsymbol{r}^{(k)})$, $\Gamma_e^{(k)}$ refers to the midpoint of edge e on triangle with number k, as in $p_n(\Gamma_e^{(k)})$ or $\boldsymbol{B}_n(\Gamma_k^{(k)})$, and $\Omega^{(k)}$ refers to a "shifted centroid", as in $p_n(\Omega^{(k)})$ or $\boldsymbol{B}_n(\Omega^{(k)})$. This shifted centroid is calculated by assigning double weight to node F, i.e. $\left(\frac{1}{2}, \frac{1}{4}, \frac{1}{4}\right)$ in barycentric coordinates where the first coordinate is defined relative to node F. This assures that this shifted centroid is halfway between flux surfaces, as the actual centroid is closer to the flux surface on which nodes I and O lie, thus alternating between the two flux surfaces from one triangle to the next. To get an idea of this behaviour, refer to fig. 3.2, where the $\otimes$ symbols indicating the $\nabla\varphi$ basis vectors are placed at these shifted centroids.

Furthermore, toroidal components of vector fields are approximated by a single value, evaluated at the aforementioned shifted centroid:

$$\Psi_\varphi = \int_\Omega R B_n^\varphi \,\mathrm{d}S \approx S_\Omega R(\Omega) B_n^\varphi(\Omega), \tag{3.48}$$

$$I_\varphi = \int_\Omega R J_n^\varphi \,\mathrm{d}S \approx S_\Omega R(\Omega) J_n^\varphi(\Omega). \tag{3.49}$$

These degrees of freedom are usually set to a value that assures zero divergence in conjunction with the degrees of freedom of the associated triangle in the poloidal plane.

Some further interpolations will become necessary, using the approximations now established. In the formulae derived in chapter 5, terms of the form $\boldsymbol{v}\cdot\nabla\psi$ appear, where $\boldsymbol{v}$ is an arbitrary vector, usually the vector of a triangle edge or some field quantity. In the latter case, this reduces to the projection on the normal vector of an edge, since we represent perturbed vector fields by Raviart–Thomas elements. The relation of the degrees of freedom to the contravariant ψ component of the magnetic perturbation on edge f is derived here as an example, as we use it for computations in sections 5.1 and 7.1. The general expression on a given triangle is given by

$$B_n^\psi(\Gamma_\mathrm{f}) = \boldsymbol{B}_n(\Gamma_\mathrm{f})\cdot\nabla\psi(\Gamma_\mathrm{f}) = \boldsymbol{B}_n(\Gamma_\mathrm{f})\cdot\hat{\boldsymbol{n}}_\mathrm{f}\frac{\partial\psi}{\partial n_\mathrm{f}}(\Gamma_\mathrm{f}). \tag{3.50}$$

Here we used the fact that the gradient of ψ is parallel to $\boldsymbol{n}_\mathrm{f}$. To approximate the directional derivative on Γ_f, first consider fig. 3.3. The indices ±1 here refer to the adjacent outer and inner flux surface that are realized on grid points. Likewise, $\Omega^{(\pm1)}$ refers to the triangles that

touch the adjacent flux surfaces and edge f in question. a_f refers to the altitude of edge f on a given triangle. Since $\boldsymbol{n}_\mathrm{f}$ is pointing toward the outer flux surface, i.e. it is defined in regard to

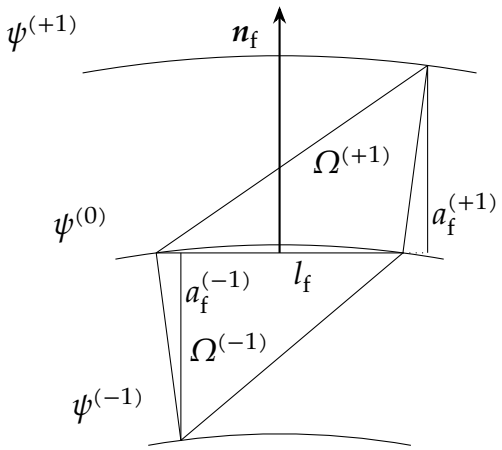

Figure 3.3: Geometrical considerations in the calculation of $B_n^\psi(\Gamma_\mathrm{f})$.

$\Omega^{(-1)}$, the difference in ψ is computed in the same direction, while the distance between the flux surfaces is approximated by the sum of the altitudes:

$$\frac{\partial\psi}{\partial n_\mathrm{f}}(\Gamma_\mathrm{f}) \approx \frac{\psi^{(+1)} - \psi^{(-1)}}{a_\mathrm{f}^{(+1)} + a_\mathrm{f}^{(-1)}}. \tag{3.51}$$

The altitudes can be calculated via triangle area and edge length,

$$S_{\Omega^{(\pm1)}} = \frac{l_\mathrm{f} a_\mathrm{f}^{(\pm1)}}{2}, \tag{3.52}$$

yielding

$$\frac{\partial\psi}{\partial n_\mathrm{f}}(\Gamma_\mathrm{f}) \approx \frac{l_\mathrm{f}}{2}\frac{\psi^{(+1)} - \psi^{(-1)}}{S_{\Omega^{(+1)}} + S_{\Omega^{(-1)}}}. \tag{3.53}$$

Now, remembering that $\boldsymbol{n}_\mathrm{f} = l_\mathrm{f}\hat{\boldsymbol{n}}_\mathrm{f}$ and that the degrees of freedom are given by $\Psi_\mathrm{f} = R(\Gamma_\mathrm{f})\boldsymbol{B}_n(\Gamma_\mathrm{f}) \cdot \boldsymbol{n}_\mathrm{f}$, we can put everything together and arrive at a direct relation between B_n^ψ and the degrees of freedom:

$$B_n^\psi(\Gamma_\mathrm{f}) \approx \frac{\boldsymbol{B}_n(\Gamma_\mathrm{f}) \cdot l_\mathrm{f}\hat{\boldsymbol{n}}_\mathrm{f}}{2}\frac{\psi^{(+1)} - \psi^{(-1)}}{S_{\Omega^{(+1)}} + S_{\Omega^{(-1)}}} = \frac{\Psi_\mathrm{f}}{2R}\frac{\psi^{(+1)} - \psi^{(-1)}}{S_{\Omega^{(+1)}} + S_{\Omega^{(-1)}}}. \tag{3.54}$$

When $\boldsymbol{n}_\mathrm{f}$ and Ψ_f are defined in regard to $\Omega^{(+1)}$ instead, both quantities switch sign. Since B_n^ψ does not depend on the choice of triangle, the sign on the right-hand side of eq. (3.54) would also change in this case.

Another useful quantity is the covariant ϑ component of a vector field, here derived for the

example of the current perturbation,

$$J_{n\vartheta} = \boldsymbol{J}_n \cdot \boldsymbol{e}_\vartheta = \boldsymbol{J}_n \cdot \sqrt{g}\,(\boldsymbol{e}^\varrho \times \boldsymbol{e}^\varphi) = -\boldsymbol{J}_n \cdot \sqrt{g}(\nabla\psi \times \nabla\varphi) = \boldsymbol{J}_n \cdot \frac{q\boldsymbol{B}_0^{\mathrm{pol}}}{B_0^\varphi}, \tag{3.55}$$

where we used eq. (3.31) in the last step.

Chapter 4

Numerical Treatment of the Magnetic Field Perturbation

In this chapter, the calculation of the magnetic field from the current density is described, i.e. the explicit form of $\hat{M}$ in eq. (2.11). The implementation uses `FreeFem++` by Hecht [6], while the mathematical background is outlined in section 4.1, which is based on the book by Jin [9]. For a more specific discussion and thorough derivations for the problem at hand, see Seeber [13]. Finally, the application of the Fourier transform is elaborated in section 4.2, based on the papers by Heyn et al. [7] and Albert et al. [1].

The finite element method can be used to numerically solve partial differential equations, specifically boundary value problems. Before delving into the details of the method, we shall look at how this applies to eq. (2.8). Using an identity from vector analysis, we get

$$\nabla \times (\nabla \times \boldsymbol{A}) = \nabla(\nabla \cdot \boldsymbol{A}) - (\nabla \cdot \nabla)\boldsymbol{A} = \frac{4\pi}{c}\boldsymbol{J}. \tag{4.1}$$

Without loss of generality, we use the Coulomb gauge with

$$\nabla \cdot \boldsymbol{A} = 0 \tag{4.2}$$

and eq. (4.1) reduces to

$$(\nabla \cdot \nabla)\boldsymbol{A} =: \Delta \boldsymbol{A} = -\frac{4\pi}{c}\boldsymbol{J}, \tag{4.3}$$

where Δ is the Laplacian. For vector arguments, the latter only takes on a simple form for Cartesian coordinates:

$$\left(\frac{\partial^2}{\partial x^2} + \frac{\partial^2}{\partial y^2} + \frac{\partial^2}{\partial z^2}\right) A_k = -\frac{4\pi}{c} J_k \quad \forall k = x, y, z. \tag{4.4}$$

Thus the differential equation for the Cartesian components of the magnetic vector potential

is of the Poisson type,

$$\Delta\Phi = f. \tag{4.5}$$

This is an elliptical partial differential equation of second order, so the solution shall be twice continuously differentiable on the given domain, i.e. $\Phi \in C^2(\Omega)$. For this type of PDE, a unique solution exists when one of the following boundary conditions is imposed on the boundary $\Gamma = \partial\Omega$.

- A Dirichlet boundary condition imposes functional values on the boundary:

$$\Phi(\boldsymbol{r}) = \gamma_\mathrm{D}(\boldsymbol{r}) \quad \forall \boldsymbol{r} \in \Gamma.$$

- A Neumann boundary condition imposes normal derivatives on the boundary:

$$\nabla\Phi(\boldsymbol{r}) \cdot \boldsymbol{n}(\boldsymbol{r}) = \gamma_\mathrm{N}(\boldsymbol{r}) \quad \forall \boldsymbol{r} \in \Gamma.$$

  There is an additional compatibility condition that has to be satisfied by the inhomogeneities of Poisson's equation and the boundary condition:

$$\oint_\Gamma \gamma_\mathrm{N}(\boldsymbol{r})\,\mathrm{d}\Gamma = \int_\Omega f(\boldsymbol{r})\,\mathrm{d}\Omega.$$

- A Robin boundary condition imposes a weigehted sum of Dirichlet and Neumann boundary conditions:

$$C_\mathrm{D}\Phi(\boldsymbol{r}) + C_N\nabla\Phi(\boldsymbol{r}) \cdot \boldsymbol{n}(\boldsymbol{r}) = \gamma_\mathrm{R}(\boldsymbol{r}) \quad \forall \boldsymbol{r} \in \Gamma.$$

  This has to be distinguished from a Cauchy boundary condition where Dirichlet and Neumann boundary conditions are imposed on the same point independently of each other. For elliptical PDEs, this usually is not a well-posed problem and may lead to an overdetermined set of equations.

- Mixed boundary conditions are enforced when any of the above is imposed on each piece of the boundary, e.g. Dirichlet boundary conditions on Γ_D and Neumann boundary conditions on Γ_N. In the latter example, it is necessary that

$$\Gamma_\mathrm{N} \cup \Gamma_\mathrm{D} = \Gamma, \quad \Gamma_\mathrm{N} \cap \Gamma_\mathrm{D} = \emptyset$$

  holds to avoid the aforementioned problem with Cauchy boundary conditions.

Even though we applied this categorization to Cartesian components, it holds in any coordinate system since a simple geometrical coordinate transform does not change the type of the PDE and thus the finite element method is applicable. It should be noted, however, that we can not prescribe all vector components at the same time; according to Bíró [3], the normal and

tangential components have to be separated. For the normal components, we can prescribe the magnetic surface charge density b,

$$\boldsymbol{B} \cdot \boldsymbol{n} = -b, \tag{4.6}$$

which has to fulfill the additional condition that

$$\oint_\Gamma b \, \mathrm{d}\Gamma = -\oint_\Gamma \boldsymbol{B} \cdot \boldsymbol{n} \, \mathrm{d}\Gamma = -\int_\Omega \nabla \cdot \boldsymbol{B} \, \mathrm{d}\Omega = 0.$$

For the tangential component, the magnetic surface current density $\boldsymbol{K}$ can be prescribed,

$$\boldsymbol{B} \times \boldsymbol{n} = \frac{4\pi}{c}\boldsymbol{K}, \tag{4.7}$$

which has to fulfill the additional condition that

$$\frac{4\pi}{c}\oint_\Gamma \boldsymbol{K} \, \mathrm{d}\Gamma = \oint_\Gamma \boldsymbol{B} \times \boldsymbol{n} \, \mathrm{d}\Gamma = -\int_\Omega \nabla \times \boldsymbol{B} \, \mathrm{d}\Omega = -\frac{4\pi}{c}\int_\Omega \boldsymbol{J} \, \mathrm{d}\Omega.$$

When deriving the weak formulation in the following section, these two options will be assigned to their corresponding boundary conditions.

4.1 Outline of the Ritz and Galerkin Methods

The finite element method is used to solve problems of the general form

$$\mathcal{L}\Phi = f, \tag{4.8}$$

where Φ and f are arbitrary functions and $\mathcal{L}$ is a differential operator. For the Ritz method, $\mathcal{L}$ is assumed to be a real differential operator that is self-adjoint and positive definite, i.e.

$$\langle \mathcal{L}u, v \rangle = \langle u, \mathcal{L}v \rangle, \tag{4.9}$$

$$\langle \mathcal{L}u, u \rangle \begin{cases} > 0 & u \neq 0, \\ = 0 & u = 0 \end{cases} \tag{4.10}$$

in regard to a scalar product defined by

$$\langle u, v \rangle = \int_\Omega u v^* \, \mathrm{d}\Omega. \tag{4.11}$$

The solution of the differential equation corresponds to the minimum of the functional

$$F(\Phi) = \tfrac{1}{2}\langle \mathcal{L}\Phi, \Phi \rangle - \tfrac{1}{2}\langle \Phi, f \rangle - \tfrac{1}{2}\langle f, \Phi \rangle, \tag{4.12}$$

i.e. $\delta F = 0$ and $\delta(\delta F) > 0$, where δF is the variation. Now, the problem is discretized by projecting Φ into a finite subspace of the full solution space, i.e. it is approximated by

$$\tilde{\Phi} = \sum_{k=1}^{N} C_k v_k = \boldsymbol{C} \cdot \boldsymbol{v}, \tag{4.13}$$

where C_k are constant expansion coefficients or *degrees of freedom* and v_k are *basis functions* which will be defined later. Now, the variational form in eq. (4.12) can be cast into an algebraic form,

$$\frac{\partial}{\partial C_k} F(\tilde{\Phi}) = 0 \quad \forall k = 1, 2, \dots, N. \tag{4.14}$$

This results in a system of N linear equations of N unknowns,

$$\hat{K}\boldsymbol{C} = \boldsymbol{s}. \tag{4.15}$$

Here, $\hat{K}$ is the *stiffness matrix*[1] given by

$$K_{jk} = \frac{1}{2}\int_\Omega v_j \mathcal{L} v_k + v_k \mathcal{L} v_j \,\mathrm{d}\Omega = \int_\Omega v_j \mathcal{L} v_k \,\mathrm{d}\Omega \quad \forall j, k = 1, 2, \dots, N, \tag{4.16}$$

where we used eq. (4.9) in the last equality. The *load vector*[1] $\boldsymbol{s}$ is given by

$$s_k = \int_\Omega v_k f \,\mathrm{d}\Omega \quad \forall k = 1, 2, \dots, N. \tag{4.17}$$

Now, describing the whole domain Ω by a limited set of basis functions $\boldsymbol{v}$ would entail the construction of complicated basis function to cover the whole domain. Instead, we discretize the computational domain into the eponymous *finite elements*, which we already discussed in section 3.2. The basis functions are then defined to extend only over one element and to be zero on all others. This allows a reasonable approximation of almost arbitrary functions by simple polynomial basis functions over arbitrary domains. Equation (4.15) is then defined for each of the M finite elements, yielding a set of MN linear equations in MN unknowns. Since only a few neighboring finite elements are connected, $\hat{K}$ then takes the shape of a band matrix, for which efficient numerical solutions are available.

The conventional Ritz method also has its shortcomings. When $\mathcal{L}$ is not self-adjoint or positive definite, the Ritz method has to be modified. For example, complex $\mathcal{L}$ are not self-adjoint with the scalar product defined in eq. (4.11). Furthermore, if inhomogeneous boundary conditions are applied, the functional F has to be extended by a function that fulfills this boundary condition. For all these generalized cases, the Galerkin method may be used instead, which also does not require the construction of a variational form. Observing that $\tilde{\Phi}$ is only an approximation to Φ, inserting the former into the original differential eq. (4.8) will leave a

[1] These quantities derive their names from the application of the method to problems of solid mechanics in civil engineering.

residue, i.e.

$$\mathcal{L}\tilde{\Phi} - f \neq 0. \tag{4.18}$$

Now, another approach to approximate the minimum of the functional F is to minimize the residues r_k with regard to weighting functions w_k,

$$r_k = \int_\Omega w_k \underbrace{(\mathcal{L}\tilde{\Phi} - f)}_{\neq 0} \, \mathrm{d}\Omega. \tag{4.19}$$

For the Galerkin method, the weighting functions w_k are the same as the basis functions v_k. This approach also results in a system of N linear equations of N unknowns, as in eq. (4.15). Here, $\hat{K}$ is only symmetric if $\mathcal{L}$ is self-adjoint, in which case the equations are the same as with the Ritz method.

The weighting functions w_k are also called *test functions* in the context of the *weak formulation* of the differential equation, where they are used to apply integration by parts or analogs thereof, such as Green's identities or the divergence theorem. This allows the enforcement of the boundary conditions since integrals on the boundary will appear. As an illustration, we shall derive the weak formulation of eq. (2.8) based on the treatment by Bíró [3]. To this end, we take a dot product of eq. (2.8) with a vectorial test function $\boldsymbol{w}$, integrate over Ω, and apply the divergence theorem:

$$\begin{aligned}
\int_\Omega \boldsymbol{w} \cdot (\nabla \times (\nabla \times \boldsymbol{A})) \, \mathrm{d}\Omega &= \frac{4\pi}{c} \int_\Omega \boldsymbol{w} \cdot \boldsymbol{J} \, \mathrm{d}\Omega, \\
\int_\Omega (\nabla \times \boldsymbol{w}) \cdot (\nabla \times \boldsymbol{A}) \, \mathrm{d}\Omega - \int_\Omega \nabla \cdot (\boldsymbol{w} \times (\nabla \times \boldsymbol{A})) \, \mathrm{d}\Omega &= \frac{4\pi}{c} \int_\Omega \boldsymbol{w} \cdot \boldsymbol{J} \, \mathrm{d}\Omega, \\
\int_\Omega (\nabla \times \boldsymbol{w}) \cdot (\nabla \times \boldsymbol{A}) \, \mathrm{d}\Omega - \oint_\Gamma (\boldsymbol{w} \times (\nabla \times \boldsymbol{A})) \cdot \boldsymbol{n} \, \mathrm{d}\Gamma &= \frac{4\pi}{c} \int_\Omega \boldsymbol{w} \cdot \boldsymbol{J} \, \mathrm{d}\Omega, \\
\int_\Omega (\nabla \times \boldsymbol{w}) \cdot (\nabla \times \boldsymbol{A}) \, \mathrm{d}\Omega - \oint_\Gamma \boldsymbol{w} \cdot ((\nabla \times \boldsymbol{A}) \times \boldsymbol{n}) \, \mathrm{d}\Gamma &= \frac{4\pi}{c} \int_\Omega \boldsymbol{w} \cdot \boldsymbol{J} \, \mathrm{d}\Omega.
\end{aligned} \tag{4.20}$$

The second integral on the left-hand side shows that a Neumann boundary condition of the form

$$(\nabla \times \boldsymbol{A}) \times \boldsymbol{n} = \frac{4\pi}{c} \boldsymbol{K}, \tag{4.21}$$

corresponding to the tangential component in eq. (4.7), appears as a *natural boundary condition* of the weak form. Equation (4.21) can be used to replace the expression in the weak formulation to impose the boundary condition. For the Dirichlet boundary condition, we make the connection to eq. (4.6) via

$$\begin{aligned}
\boldsymbol{A} \times \boldsymbol{n} &= \boldsymbol{\alpha}, \\
\nabla \cdot (\boldsymbol{A} \times \boldsymbol{n}) &= \nabla \cdot \boldsymbol{\alpha} = -b,
\end{aligned} \tag{4.22}$$

$$\boldsymbol{n} \cdot (\nabla \times \boldsymbol{A}) - \boldsymbol{A} \cdot \underbrace{(\nabla \times \boldsymbol{n})}_{\mathbf{0}} = -b,$$
$$\boldsymbol{n} \cdot (\nabla \times \boldsymbol{A}) = \boldsymbol{B} \cdot \boldsymbol{n} = -b,$$

where $\boldsymbol{\alpha}$ is an auxiliary function also depending on the gauge of $\boldsymbol{A}$. Since it cannot be connected to the weak formulation in eq. (4.20), eq. (4.22) is an *essential boundary condition*; it poses direct restrictions on the degrees of freedom at the boundary elements in the form $C_j = \alpha_j$ (see eq. (4.15)) for all affected j. By setting

$$K_{jk} = \delta_{jk} \quad \forall k = 1, 2, \dots, MN, \tag{4.23}$$
$$s_j = \alpha_j, \tag{4.24}$$
$$s_k \to s_k - K_{kj} \quad \forall k \neq j, \tag{4.25}$$

we ensure $K_{kj} = \delta_{kj}$ and thus $\hat{K}$ stays symmetric. Now, the jth row and column can be omitted without changing the solution, reducing the dimension of the system of equations. A less sophisticated alternative is the *penalty method*, where we employ a sufficiently large value h and set

$$K_{jj} = h, \tag{4.26}$$
$$s_j = h\alpha_j. \tag{4.27}$$

This approximates the boundary condition eq. (4.22) and also leaves $\hat{K}$ symmetric.

Finally, we have to choose appropriate basis functions which approximate the underlying solution space. While we initially demanded that the solution be twice continuously differentiable, i.e., $A_k \in C^2(\Omega)$, the weak formulation suggests this is not strictly necessary. The integration by parts – or equivalently the divergence theorem used in eq. (4.20) – gives rise to the notion of the *weak derivative*. Applied to eq. (4.20), this means that there can be a valid solution with $\nabla \times \boldsymbol{A}$ even when $\nabla \times (\nabla \times \boldsymbol{A})$ only exists in the weak sense that the application of the divergence theorem is valid and the integral exists. Thus also *weak solutions* are allowed, and the underlying solution space is a Sobolev space. For our problem, the relevant Sobolev spaces are defined in relation to the L^2 norm

$$\|w\|_2 = \sqrt{\int_\Omega |w|^2 \, \mathrm{d}\Omega}, \tag{4.28}$$

so that they are at least square-integrable:

$$L^2(\Omega) = \{w : \Omega \to \mathbb{C} \mid \|w\|_2 < \infty\}. \tag{4.29}$$

Now the Sobolev space $H^1(\Omega)$ consists of functions whose first derivatives along all coordi-

nates u_k are also square-integrable:

$$H^1(\Omega) = \{w \in L^2(\Omega) \mid \frac{\partial}{\partial u^k} w \in L^2(\Omega)\}. \tag{4.30}$$

This is the appropriate function space for scalar functions whose gradient appears in the weak formulation. They are approximated by Lagrange elements whose degrees of freedom of lowest order are the values on nodes of the finite elements. An example would be the pressure p, if it were to appear in the weak formulation. Another important Sobolev space $H(\mathrm{div}, \Omega)$ which is defined for vector-valued functions $\boldsymbol{w}$ as

$$H(\mathrm{div}, \Omega) = \{w_i \in L^2(\Omega) \mid \nabla \cdot \boldsymbol{w} \in L^2(\Omega)\}. \tag{4.31}$$

Whenever we need the divergence of a vector field, e.g., for $\boldsymbol{J}$ and $\boldsymbol{B}$, this is the appropriate function space to consider. It is approximated by Raviart–Thomas elements with vector-valued basis functions and the perpendicular component of edges as degrees of freedom for lowest-order elements. This means that the perpendicular component is continuous across edges, which is important for the application of the divergence theorem. On the other hand, the parallel component on edges might be discontinuous across elements. While we have introduced these two function spaces and basis functions already in section 3.2, we still need a function space for $\boldsymbol{A}$ with a well-defined curl. $H(\mathbf{rot}, \Omega)$ is defined accordingly:

$$H(\mathbf{rot}, \Omega) = \{w_i \in L^2(\Omega) \mid (\nabla \times w)^{u_k} \in L^2(\Omega)\}. \tag{4.32}$$

The associated basis functions are the Nédélec elements. Like the Raviart–Thomas elements, they use vectorial basis function, but the degrees of freedom are the parallel components along edges, which is necessary for the application of Stokes' theorem. The continuity conditions are also reversed compared to Raviart–Thomas elements, i.e., parallel components are continuous across edges, but the perpendicular components might be discontinuous. Finally, another useful property of these function spaces is the de Rham complex, which shows the relation between these function spaces and the differential operators mediating between them. We can write it concisely as

$$H^1(\Omega) \xrightarrow{\mathbf{grad}} H(\mathbf{rot}, \Omega) \xrightarrow{\mathbf{rot}} H(\mathrm{div}, \Omega) \xrightarrow{\mathrm{div}} L^2(\Omega). \tag{4.33}$$

The interpretation is as follows: Applying the curl to a function from $H(\mathbf{rot}, \Omega)$ yields a result in $H(\mathrm{div}, \Omega)$. Thus when we take the curl of $\boldsymbol{A} \in H(\mathbf{rot}, \Omega)$, the result $\boldsymbol{B} \in H(\mathrm{div}, \Omega)$ meets our demand of a well-defined divergence.

4.2 Reduction to two dimensions

As a further simplification, we want to apply the poloidal-toroidal decomposition discussed in chapter 3. In the appendix of their paper, Heyn et al. [7] describe the basics of the procedure.

$\boldsymbol{A}(R, \varphi, Z)$ is split into an axisymmetric part $\bar{\boldsymbol{A}}(R, Z)$ and an non-axisymmetric part $\tilde{\boldsymbol{A}}(R, \varphi, Z)$. When we apply the FOURIER transform to the latter, there is no contribution from the mode $n = 0$ by definition. Following that, we gauge $\tilde{\boldsymbol{A}}$ so that $\tilde{A}_\varphi = 0$, which is accomplished by the transformation

$$\tilde{\boldsymbol{A}} \to \tilde{\boldsymbol{A}} - \nabla \int_{\varphi_{\min}}^{\varphi} \tilde{A}_\varphi \, \mathrm{d}\varphi', \tag{4.34}$$

which reduces to

$$\tilde{\boldsymbol{A}} \to \tilde{\boldsymbol{A}} - \frac{\nabla \tilde{A}_{n\varphi}}{\mathrm{i}n} \tag{4.35}$$

since we only consider a single harmonic $n \neq 0$. The magnetic field perturbation $\boldsymbol{B}_n$ is then given as

$$B_n^R = \frac{\mathrm{i}n}{R} A_{nZ}, \qquad B_n^\varphi = \frac{1}{R}\left(\frac{\partial A_{nR}}{\partial Z} - \frac{\partial A_{nZ}}{\partial R}\right), \qquad B_n^Z = -\frac{\mathrm{i}n}{R} A_{nR}. \tag{4.36}$$

This reduces the problem to the poloidal plane and we only need to solve

$$-R\frac{\partial}{\partial Z}\left(\frac{\partial A_{nR}}{\partial Z} - \frac{\partial A_{nZ}}{\partial R}\right) + \frac{n^2}{R} A_{nR} = \frac{4\pi}{c} R J_n^R, \tag{4.37}$$

$$R\frac{\partial}{\partial R}\left(\frac{\partial A_{nR}}{\partial Z} - \frac{\partial A_{nZ}}{\partial R}\right) + \frac{n^2}{R} A_{nZ} = \frac{4\pi}{c} R J_n^Z. \tag{4.38}$$

Integration by parts in coordinate space yields the weak formulation as

$$\int_\Omega R\left(\frac{\partial A_{nR}}{\partial Z} - \frac{\partial A_{nZ}}{\partial R}\right)\left(\frac{\partial w_R}{\partial Z} - \frac{\partial w_Z}{\partial R}\right) + \frac{n^2}{R}(A_{nR} w_R + A_{nZ} w_Z)\,\mathrm{d}R\,\mathrm{d}Z = \\ = \frac{4\pi}{c}\int_\Omega R(J_n^R w_R + J_n^Z w_Z)\,\mathrm{d}R\,\mathrm{d}Z, \tag{4.39}$$

where $\boldsymbol{w}$ is a test function with the restriction $w_\varphi = 0$. Note that the integral on the boundary is already omitted, as we impose a homogeneous NEUMANN boundary condition. As Albert et al. [1] note: "If Ω is [extended] with a large enough current-free region around the actual domain of interest, this description is suited to approximately describe the decay of the magnetic field at infinite distance."

Chapter 5

Linearized MHD Force Balance

In this chapter, we derive a solution of the linearized MHD force balance from eq. (3.4) in the field-aligned geometry described in chapter 3. This corresponds to the application of the $\hat{P}$ operator in eq. (2.10) occurring in the iterations outlined in section 2.1. Section 5.1 concerns the intermediate step of computing the pressure perturbation from the magnetic field perturbation, which is necessary for the computation of the current perturbation derived in section 5.2. Finally, in section 5.3, we discuss the extension of the ideal MHD model by the inclusion of sheet currents.

5.1 Pressure Perturbation

Multiplying eq. (3.4) by $\boldsymbol{B}_0$ yields

$$\begin{aligned} c\boldsymbol{B}_0 \cdot \nabla p_n + \mathrm{i}nc p_n \boldsymbol{B}_0 \cdot \nabla\varphi &= -\boldsymbol{B}_n \cdot (\boldsymbol{J}_0 \times \boldsymbol{B}_0) = -c\boldsymbol{B}_n \cdot \nabla p_0 \\ \boldsymbol{B}_0^{\mathrm{pol}} \cdot \nabla p_n + \mathrm{i}n p_n B_0^{\varphi} &= -B_n^{\psi} p_0'(\psi). \end{aligned} \tag{5.1}$$

To solve this equation on one flux surface, we use a lowest-order finite difference method. Nodes are indexed by superscript (k) and $\boldsymbol{r}^{(k)}$ is the position of node (k), whereas $\boldsymbol{l}_{\mathrm{f}}^{(k)} = \boldsymbol{r}^{(k+1)} - \boldsymbol{r}^{(k)}$ is the counter-clockwise vector between nodes on edge $\Gamma_{\mathrm{f}}^{(k)}$. ∇p_n is approximated at the midpoint of edge $\Gamma_{\mathrm{f}}^{(k)}$ as finite difference of p_n at nodes (k) and $(k+1)$. p_n is accordingly approximated at the midpoint as the arithmetic mean of the values at these nodes. With a shorthand $p_n^{(k)} = p_n(\boldsymbol{r}^{(k)})$ for the degrees of freedom we get

$$\boldsymbol{B}_0^{\mathrm{pol}}(\Gamma_{\mathrm{f}}^{(k)}) \cdot \frac{\boldsymbol{l}_{\mathrm{f}}^{(k)}}{l_{\mathrm{f}}^{(k)}} \frac{p_n^{(k+1)} - p_n^{(k)}}{l_{\mathrm{f}}^{(k)}} + \mathrm{i}nB_0^{\varphi}(\Gamma_{\mathrm{f}}^{(k)}) \frac{p_n^{(k+1)} + p_n^{(k)}}{2} = -\frac{\mathrm{d}p_0}{\mathrm{d}\psi}(\Gamma_{\mathrm{f}}^{(k)}) B_n^{\psi}(\Gamma_{\mathrm{f}}^{(k)}), \tag{5.2}$$

where a unit vector along the edge is used to get the correct sign for the gradient in the direction of the poloidal magnetic field. Reordering in terms of the unknowns yields

$$(b_k + a_k)p_n^{(k+1)} + (b_k - a_k)p_n^{(k)} = s_k \tag{5.3}$$

with

$$a_k = \boldsymbol{B}_0^{\mathrm{pol}}(\Gamma_{\mathrm{f}}^{(k)}) \cdot \frac{\hat{\boldsymbol{l}}_{\mathrm{f}}^{(k)}}{l_{\mathrm{f}}^{(k)}}, \tag{5.4}$$

$$b_k = \frac{\mathrm{i}nB_0^{\varphi}(\Gamma_{\mathrm{f}}^{(k)})}{2}, \tag{5.5}$$

$$s_k = -\frac{\mathrm{d}p_0}{\mathrm{d}\psi}(\Gamma_{\mathrm{f}}^{(k)})B_n^{\psi}(\Gamma_{\mathrm{f}}^{(k)}). \tag{5.6}$$

In matrix form this scheme is written as

$$K_{jk}p_n^{(k)} = s_j, \tag{5.7}$$

where the elements of the matrix $\hat{K}$ are

$$K_{jk} = (b_j + a_j)\delta_{j-1,k} + (b_j - a_j)\delta_{jk}. \tag{5.8}$$

Note that for N nodes with periodic boundary conditions $p_n^{(0)} = p_n^{(N)}$, indices "wrap around", resulting in the following shape for the stiffness matrix:

$$\hat{K} = \begin{pmatrix} b_1 - a_1 & b_1 + a_1 & 0 & \dots & 0 \\ 0 & b_2 - a_2 & b_2 + a_2 & \dots & 0 \\ 0 & 0 & b_3 - a_3 & \dots & 0 \\ \vdots & \vdots & \vdots & \ddots & \vdots \\ b_N + a_N & 0 & 0 & \dots & b_N - a_N \end{pmatrix}.$$

5.2 Current Perturbation

To derive an expression for the degrees of freedom of $\boldsymbol{J}_n$, we start from the linear force balance in eq. (3.4) and put the unknown current perturbation on one side:

$$\underbrace{\boldsymbol{J}_n \times \boldsymbol{B}_0}_{\text{(I)}} = \underbrace{c(\nabla p_n + \mathrm{i}np_n\nabla\varphi)}_{\text{(II)}} - \underbrace{\boldsymbol{J}_0 \times \boldsymbol{B}_n}_{\text{(III)}}. \tag{5.9}$$

Taking a scalar product of some edge $\boldsymbol{l}$ – in the course of this derivation, we don't indicate evaluation at the edge midpoint Γ to avoid cluttering up the equations – with term (I) in eq. (5.9) yields

$$\boldsymbol{l} \cdot (\boldsymbol{J}_n \times \boldsymbol{B}_0) = \boldsymbol{l} \cdot (\boldsymbol{J}_n \times (\nabla\psi \times \nabla\varphi + B_{0\varphi}\nabla\varphi)) \tag{5.10}$$

with the definiton of the equilibrium field from eq. (3.24). Cyclic permutation gives

$$\boldsymbol{l} \cdot (\boldsymbol{J}_n \times \boldsymbol{B}_0) = \boldsymbol{J}_n \cdot ((\nabla\psi \times \nabla\varphi) \times \boldsymbol{l} + B_{0\varphi} \nabla\varphi \times \boldsymbol{l}), \tag{5.11}$$

where another triple product formula and the definition of the local coordinates from eq. (3.41) can be applied:

$$\boldsymbol{l} \cdot (\boldsymbol{J}_n \times \boldsymbol{B}_0) = \boldsymbol{J}_n \cdot \left((\boldsymbol{l} \cdot \nabla\psi)\nabla\varphi + \frac{B_{0\varphi}}{R}\boldsymbol{n} \right). \tag{5.12}$$

Changing from co- to contravariant coordinates and carrying out the scalar product yields

$$\boldsymbol{l} \cdot (\boldsymbol{J}_n \times \boldsymbol{B}_0) = (\boldsymbol{l} \cdot \nabla\psi) J_n^{\varphi} + R B_0^{\varphi} \boldsymbol{J}_n^{\mathrm{pol}} \cdot \boldsymbol{n}. \tag{5.13}$$

On the right-hand side, we can insert the definition from eq. (3.40), reorder and in the result replace the definition from eq. (3.25), giving

$$\boldsymbol{l} \cdot \nabla\psi = (\boldsymbol{n} \times R\nabla\varphi) \cdot \nabla\psi = -R\boldsymbol{B}_0^{\mathrm{pol}} \cdot \boldsymbol{n}. \tag{5.14}$$

Finally,

$$\boldsymbol{l} \cdot (\boldsymbol{J}_n \times \boldsymbol{B}_0) = R B_0^{\varphi} \boldsymbol{J}_n^{\mathrm{pol}} \cdot \boldsymbol{n} - R J_n^{\varphi} \boldsymbol{B}_0^{\mathrm{pol}} \cdot \boldsymbol{n}. \tag{5.15}$$

Multiplying term (II) of eq. (5.9) by $\boldsymbol{l}$ simply gives

$$\boldsymbol{l} \cdot (\nabla p_n + \mathrm{i} n p_n \nabla\varphi) = \boldsymbol{l} \cdot \nabla p_n. \tag{5.16}$$

We repeat the same procedure for term (III) of eq. (5.9) and expand the cross product by poloidal-toroidal decomposition:

$$\boldsymbol{l} \cdot (\boldsymbol{J}_0 \times \boldsymbol{B}_n) = \boldsymbol{l} \cdot (B_{n\varphi} \boldsymbol{J}_0^{\mathrm{pol}} \times \nabla\varphi + J_{0\varphi} \nabla\varphi \times \boldsymbol{B}_n^{\mathrm{pol}}). \tag{5.17}$$

For the second term in parentheses, we again use cyclic permutation and the definition from eq. (3.41):

$$\begin{aligned} \boldsymbol{l} \cdot (\nabla\varphi \times \boldsymbol{B}_n^{\mathrm{pol}}) &= \boldsymbol{B}_n^{\mathrm{pol}} \cdot (\boldsymbol{l} \times \nabla\varphi) \\ &= -\frac{1}{R} \boldsymbol{B}_n^{\mathrm{pol}} \cdot \boldsymbol{n}. \end{aligned} \tag{5.18}$$

To simplify the first term in parentheses, we start from the equilibrium in eq. (2.1) and apply some of the previously used identities:

$$\begin{aligned} c\nabla p_0 &= \boldsymbol{J}_0 \times \boldsymbol{B}_0 \\ &= \boldsymbol{J}_0^{\mathrm{pol}} \times (B_{0\varphi} \nabla\varphi) + J_{0\varphi} \nabla\varphi \times (\nabla\psi \times \nabla\varphi) \end{aligned}$$

$$
\begin{aligned}
&= \boldsymbol{J}_0^{\mathrm{pol}} \times (B_{0\varphi} \nabla\varphi) + \frac{J_{0\varphi}}{R^2} \nabla\psi \\
&= \boldsymbol{J}_0^{\mathrm{pol}} \times (B_{0\varphi} \nabla\varphi) + J_0^{\varphi} \nabla\psi.
\end{aligned} \tag{5.19}
$$

Rearrangement yields

$$
\boldsymbol{J}_0^{\mathrm{pol}} \times \nabla\varphi = \frac{1}{B_{0\varphi}} \left(c\nabla p_0 - J_0^{\varphi} \nabla\psi \right). \tag{5.20}
$$

The intermediate result is

$$
\boldsymbol{l} \cdot (\boldsymbol{J}_0 \times \boldsymbol{B}_n) = \frac{B_{n\varphi}}{B_{0\varphi}} \left(c\nabla p_0 - J_0^{\varphi} \nabla\psi \right) \cdot \boldsymbol{l} - \frac{J_{0\varphi}}{R} \boldsymbol{B}_n^{\mathrm{pol}} \cdot \boldsymbol{n}. \tag{5.21}
$$

Reusing eq. (5.14) and rearranging, we get

$$
\boldsymbol{l} \cdot (\boldsymbol{J}_0 \times \boldsymbol{B}_n) = \frac{B_{n\varphi}}{B_{0\varphi}} c\nabla p_0 \cdot \boldsymbol{l} + R J_0^{\varphi} \left(\frac{B_{n\varphi}}{B_{0\varphi}} \boldsymbol{B}_0^{\mathrm{pol}} \cdot \boldsymbol{n} - \boldsymbol{B}_n^{\mathrm{pol}} \cdot \boldsymbol{n} \right). \tag{5.22}
$$

Combining eqs. (5.15), (5.16) and (5.22), eq. (5.9) is transformed to eq. (5.23):

$$
R B_0^{\varphi} \boldsymbol{J}_n^{\mathrm{pol}} \cdot \boldsymbol{n} - R J_n^{\varphi} \boldsymbol{B}_0^{\mathrm{pol}} \cdot \boldsymbol{n} = c \left(\nabla p_n - \frac{B_{n\varphi}}{B_{0\varphi}} \nabla p_0 \right) \cdot \boldsymbol{l} - R J_0^{\varphi} \left(\frac{B_{n\varphi}}{B_{0\varphi}} \boldsymbol{B}_0^{\mathrm{pol}} \cdot \boldsymbol{n} - \boldsymbol{B}_n^{\mathrm{pol}} \cdot \boldsymbol{n} \right). \tag{5.23}
$$

On edges i and o where $\boldsymbol{B}_0^{\mathrm{pol}} \cdot \boldsymbol{n} \neq 0$, we can divide by this term and we obtain an expression for J_n^{φ} in terms of $\boldsymbol{J}_n^{\mathrm{pol}} \cdot \boldsymbol{n}$ and quantities which are known at this point:

$$
R J_n^{\varphi} = J_{n(\varphi)} = R B_0^{\varphi} \frac{\boldsymbol{J}_n^{\mathrm{pol}} \cdot \boldsymbol{n}}{\boldsymbol{B}_0^{\mathrm{pol}} \cdot \boldsymbol{n}} + \frac{c}{\boldsymbol{B}_0^{\mathrm{pol}} \cdot \boldsymbol{n}} \left(\frac{B_{n\varphi}}{B_{0\varphi}} \nabla p_0 - \nabla p_n \right) \cdot \boldsymbol{l} + R J_0^{\varphi} \left(\frac{B_{n\varphi}}{B_{0\varphi}} - \frac{\boldsymbol{B}_n^{\mathrm{pol}} \cdot \boldsymbol{n}}{\boldsymbol{B}_0^{\mathrm{pol}} \cdot \boldsymbol{n}} \right). \tag{5.24}
$$

On edge f, $\boldsymbol{B}_0^{\mathrm{pol}} \cdot \boldsymbol{n} = 0$ and $\nabla p_0 \cdot \boldsymbol{l} = 0$ (compare eq. (5.14)), thus from eq. (5.23), no connection between J_n^{φ} and $\boldsymbol{J}_n^{\mathrm{pol}} \cdot \boldsymbol{n}$ can be made, but the latter expression can be given in terms of already known quantities:

$$
R \boldsymbol{J}_n^{\mathrm{pol}} \cdot \boldsymbol{n} = \frac{c \nabla p_n \cdot \boldsymbol{l}}{B_0^{\varphi}} + R \frac{J_0^{\varphi}}{B_0^{\varphi}} \boldsymbol{B}_n^{\mathrm{pol}} \cdot \boldsymbol{n}. \tag{5.25}
$$

With these relations established, we now consider the divergence of the perturbation current from eq. (3.5). In cylindrical coordinates it reads, after multiplication by R,

$$
\frac{\partial}{\partial R} (R J_n^k) + \mathrm{i} n R J_n^{\varphi} + \frac{\partial}{\partial Z} (R J_n^k) = 0. \tag{5.26}
$$

Using the divergence theorem this can also be written in integral form in a specific triangular mesh element $\Omega^{(k)}$ as

$$\oint_{\partial\Omega^{(k)}} R\boldsymbol{J}_n^{\mathrm{pol}} \cdot \hat{\boldsymbol{n}}\,\mathrm{d}l + \mathrm{i}n \int_{\Omega^{(k)}} RJ_n^{\varphi}\,\mathrm{d}R\,\mathrm{d}Z = 0. \tag{5.27}$$

Here the first integral is performed over the 1-dimensional element boundary $\partial\Omega^{(k)} = \Gamma^{(k)}$. The first term is split into three contributions,

$$\oint_{\partial\Omega^{(k)}} R\boldsymbol{J}_n^{\mathrm{pol}} \cdot \hat{\boldsymbol{n}}\,\mathrm{d}l = \int_{\Gamma_{\mathrm{i}}^{(k)},\Gamma_{\mathrm{o}}^{(k)}} R\boldsymbol{J}_n^{\mathrm{pol}} \cdot \hat{\boldsymbol{n}}\,\mathrm{d}l + \int_{\Gamma_{\mathrm{f}}^{(k)}} R\boldsymbol{J}_n^{\mathrm{pol}} \cdot \hat{\boldsymbol{n}}\,\mathrm{d}lx, \tag{5.28}$$

where edge f is tangential to an adjacent flux surface and edges i and o are not. Using the notation for currents established in eq. (3.45), we have

$$I_{\mathrm{i}} + I_{\mathrm{o}} + \mathrm{i}n \int_{\Omega} RJ_n^{\varphi}\,\mathrm{d}S = -I_{\mathrm{f}}. \tag{5.29}$$

I_{f} is already known from eq. (5.25) and therefore acts as a source on the right-hand side. We take the remaining currents I_{i} and I_{o} as unknowns. Since the current I_{o} flowing out of one triangle is equal to the current $-I_{\mathrm{i}}$ flowing into the next triangle, these unknowns are connected on one strip of triangles, and we expect a system of equations similar to the one in section 5.1. The degrees of freedom and the unknowns are illustrated in fig. 5.1 with the unknowns marked in red, along with the indexing described further below.

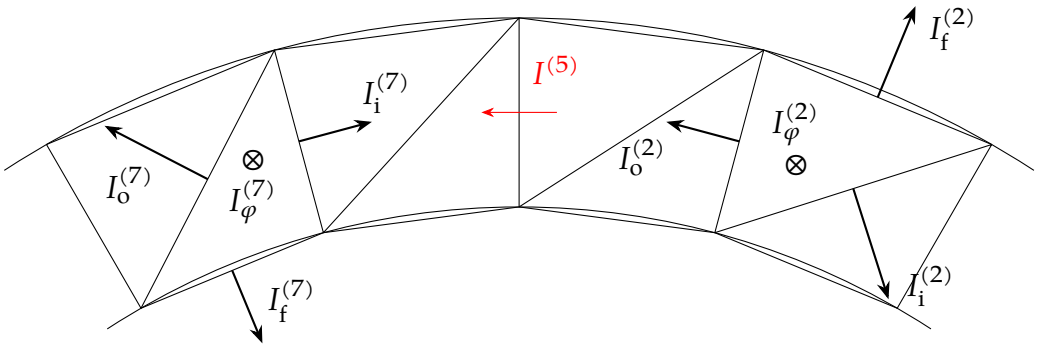

Figure 5.1: Schematic of the degrees of freedom and unknowns in the calculation of currents.

Now, we deviate from eq. (3.49) and use a different approximation for the remaining integral:

$$\mathrm{i}nI_{\varphi} = \mathrm{i}n \int_{\Omega} RJ_n^{\varphi}\,\mathrm{d}S \approx \mathrm{i}nS_{\Omega} \frac{R(\Gamma_{\mathrm{i}})J_n^{\varphi}(\Gamma_{\mathrm{i}}) + R(\Gamma_{\mathrm{o}})J_n^{\varphi}(\Gamma_{\mathrm{o}})}{2}. \tag{5.30}$$

In this approximation, a term $R(\Gamma_{\mathrm{f}})J_n^{\varphi}(\Gamma_{\mathrm{f}})$ is neglected because within one strip of triangles, edge f alternates between the inner and outer flux surface and this "oscillation" of sample points would carry over to the approximation values, which is similar to the argument regarding the shifted centroid in section 3.3. Furthermore, $J_n^{\varphi}(\Gamma_{\mathrm{f}}) \cdot \boldsymbol{n}$ can't be reformulated in terms of $\boldsymbol{J}_n^{\mathrm{pol}}(\Gamma_{\mathrm{f}})$ via eq. (5.24), which would introduce the former as another unknown

and lead to an overdetermined set of equations, possibly violating divergence-freeness. So instead, I_φ on each triangle is given by

$$\mathrm{i}nI_\varphi = \mathrm{i}n \int_\Omega RJ_n^\varphi \,\mathrm{d}S \approx \frac{\mathrm{i}nS_\Omega}{2} \left(\frac{B_0^\varphi(\Gamma_\mathrm{i})}{\boldsymbol{B}_0^\mathrm{pol}(\Gamma_\mathrm{i}) \cdot \boldsymbol{n}_\mathrm{i}} I_\mathrm{i} + \frac{B_0^\varphi(\Gamma_\mathrm{o})}{\boldsymbol{B}_0^\mathrm{pol}(\Gamma_\mathrm{o}) \cdot \boldsymbol{n}_\mathrm{o}} I_\mathrm{o} + \cdots \right), \tag{5.31}$$

where we effectively reduced I_φ to I_i, I_o and already known terms by the relation between $\boldsymbol{J}_n^\mathrm{pol} \cdot \boldsymbol{n}$ and J_n^φ in eq. (5.24). The remaining terms are moved to the right-hand-side as sources s, so the discretized equation in each triangle Ω is

$$\left(1 + \frac{\mathrm{i}nS_\Omega}{2} \frac{B_0^\varphi(\Gamma_\mathrm{i})}{\boldsymbol{B}_0^\mathrm{pol}(\Gamma_\mathrm{i}) \cdot \boldsymbol{n}_\mathrm{i}} \right) I_\mathrm{i} + \left(1 + \frac{\mathrm{i}nS_\Omega}{2} \frac{B_0^\varphi(\Gamma_\mathrm{o})}{\boldsymbol{B}_0^\mathrm{pol}(\Gamma_\mathrm{o}) \cdot \boldsymbol{n}_\mathrm{o}} \right) I_\mathrm{o} = s. \tag{5.32}$$

The source term is given by

$$s = -I_\mathrm{f} - \frac{\mathrm{i}nS_\Omega}{2} \sum_{k=\mathrm{i,o}} \frac{c}{\boldsymbol{B}_0^\mathrm{pol} \cdot \boldsymbol{n}_k} \left(\frac{B_{n\varphi}}{B_{0\varphi}} \nabla p_0 - \nabla p_n \right) \cdot \boldsymbol{l}_k + RJ_0^\varphi \left(\frac{B_{n\varphi}}{B_{0\varphi}} - \frac{\boldsymbol{B}_n^\mathrm{pol} \cdot \boldsymbol{n}_k}{\boldsymbol{B}_0^\mathrm{pol} \cdot \boldsymbol{n}_k} \right), \tag{5.33}$$

where we again ommited evaluation at Γ_k for the sake of brevity. Note that $\boldsymbol{B}_n(\Gamma_k) \cdot \boldsymbol{n}_k$ can be directly retrieved from Ψ_k, while $B_{n\varphi}(\Gamma_k)$ has to be calculated by averaging adjacent $B_{n\varphi}(\Omega)$. The directional derivatives $\boldsymbol{l}_k \cdot \nabla p_n(\Gamma_k)$ are approximated by a difference quotient with values taken at the nodes (for indexing see fig. 3.1),

$$\boldsymbol{l}_\mathrm{i} \cdot \nabla p_n(\Gamma_\mathrm{i}) = l_\mathrm{i} \hat{\boldsymbol{l}}_\mathrm{i} \cdot \nabla p_n(\Gamma_\mathrm{i}) = l_\mathrm{i} \frac{\partial p_n}{\partial \boldsymbol{l}_\mathrm{i}}(\Gamma_\mathrm{i}) \approx l_\mathrm{i} \frac{p_n(\boldsymbol{r}_\mathrm{O}) - p_n(\boldsymbol{r}_\mathrm{F})}{\|\boldsymbol{r}_\mathrm{O} - \boldsymbol{r}_\mathrm{F}\|} = p_n(\boldsymbol{r}_\mathrm{O}) - p_n(\boldsymbol{r}_\mathrm{F}), \tag{5.34}$$

$$\boldsymbol{l}_\mathrm{o} \cdot \nabla p_n(\Gamma_\mathrm{o}) = l_\mathrm{o} \hat{\boldsymbol{l}}_\mathrm{o} \cdot \nabla p_n(\Gamma_\mathrm{o}) = l_\mathrm{o} \frac{\partial p_n}{\partial \boldsymbol{l}_\mathrm{o}}(\Gamma_\mathrm{o}) \approx l_\mathrm{o} \frac{p_n(\boldsymbol{r}_\mathrm{F}) - p_n(\boldsymbol{r}_\mathrm{I})}{\|\boldsymbol{r}_\mathrm{F} - \boldsymbol{r}_\mathrm{I}\|} = p_n(\boldsymbol{r}_\mathrm{F}) - p_n(\boldsymbol{r}_\mathrm{I}), \tag{5.35}$$

where the sign has to be reversed for the type of triangle with node F on the outer flux surface. This is actually a shortcoming of the convention that nodes are named according to their opposite edges; in the implementation, we use a subroutine that gives the nodes of edges in consistent counter-clockwise order, so this case distinction is not necessary at this level. The same logic applies to $\boldsymbol{l} \cdot \nabla p_0$ terms.

For the global[1] indexing scheme, we call the ingoing current into triangle (k) counted in counter-clockwise direction $I^{(k)}$. In triangle (k), this is equal to $I_\mathrm{i} = -I^{(k)}$ and $I_\mathrm{o} = I^{(k+1)}$. This is also illustrated in fig. 5.1, where triangles are counted from one starting at the right end of the sketch. The matrix form of eq. (5.32) is then

$$K_{jk} I^{(k)} = s_j, \tag{5.36}$$

[1] in this case only referring to the current triangle strip, as opposed to the local indexing of individual triangles

where the elements of the stiffness matrix $\hat{K}$ are

$$K_{jk} = -\left(1 + \frac{\mathrm{i}nS_{\Omega^{(j)}}}{2} \frac{B_0^{\varphi}(\Gamma_{\mathrm{i}}^{(j)})}{\boldsymbol{B}_0^{\mathrm{pol}}(\Gamma_{\mathrm{i}}^{(j)}) \cdot \boldsymbol{n}_{\mathrm{i}}^{(j)}}\right) \delta_{jk} + \left(1 + \frac{\mathrm{i}nS_{\Omega^{(j)}}}{2} \frac{B_0^{\varphi}(\Gamma_{\mathrm{o}}^{(j)})}{\boldsymbol{B}_0^{\mathrm{pol}}(\Gamma_{\mathrm{o}}^{(j)}) \cdot \boldsymbol{n}_{\mathrm{o}}^{(j)}}\right) \delta_{j+1,k}. \tag{5.37}$$

5.3 Current Sheets

We have not considered one aspect of resonances yet. Starting from the static MHD equilibrium in eq. (2.1), we see that only the normal component of the current density is relevant, i.e.

$$\nabla p = \frac{1}{c} \boldsymbol{J}^{\perp} \times \boldsymbol{B}, \tag{5.38}$$

while the parallel component $\boldsymbol{J}^{\parallel} = J^{\parallel} \boldsymbol{h}$ is not fixed. Nevertheless, $\boldsymbol{J}$ must have zero divergence:

$$-\nabla \cdot \boldsymbol{J}^{\perp} = \nabla \cdot \frac{J^{\parallel} \boldsymbol{B}}{B} = \boldsymbol{B} \cdot \nabla \frac{J^{\parallel}}{B}. \tag{5.39}$$

Expanding in flux symmetry coordinates gives

$$-\nabla \cdot \boldsymbol{J}^{\perp} = \left(B^{\vartheta} \frac{\partial}{\partial \vartheta} + B^{\varphi} \frac{\partial}{\partial \varphi}\right) \frac{J^{\parallel}}{B} = B^{\vartheta} \left(\frac{\partial}{\partial \vartheta} + q \frac{\partial}{\partial \varphi}\right) \frac{J^{\parallel}}{B}, \tag{5.40}$$

which is rearranged to

$$-\frac{\nabla \cdot \boldsymbol{J}^{\perp}}{B^{\vartheta}} = \left(\frac{\partial}{\partial \vartheta} + q \frac{\partial}{\partial \varphi}\right) \frac{J^{\parallel}}{B} \tag{5.41}$$

and Fourier transformed to

$$s_{mn} = \mathrm{i}(m + nq) \left[\frac{J^{\parallel}}{B}\right]_{mn}, \tag{5.42}$$

where the left-hand side has been grouped together in the Fourier coefficient s_{mn}. Rearranging yields

$$\frac{s_{mn}}{\mathrm{i}(m + nq)} = \left[\frac{J^{\parallel}}{B}\right]_{mn}. \tag{5.43}$$

For comparison, translation to the conventions of this thesis of eq. (1) in the paper by Waelbroeck [14] gives

$$\left[\frac{J^{\parallel}}{B}\right]_{mn} = \frac{4\pi p'(\varrho)}{\langle B^2 \rangle} \sum_{m,n} \frac{\mathcal{G}_{mn}(\varrho)}{q(\varrho) - \frac{m}{n}} + C_{mn} \delta\left(q(\varrho) - \frac{m}{n}\right), \tag{5.44}$$

where the $\mathcal{G}_{mn}$ are geometric factors and the C_{mn} are integration constants. The additional delta distribution term in eq. (5.44) is apparently missing from eq. (5.43) and we […] to add it in order to better capture the physical behaviour of the sheet currents. To approximate the delta distribution, we consider the distortion $\delta\psi$ of flux surfaces, specifically eq. (7.5). A similar expression can be derived by expanding eq. (5.1) in flux symmetry coordinates, giving

$$B_0^\vartheta \frac{\partial}{\partial\vartheta} p_n + \mathrm{i}np_n B_0^\varphi = -B_n^\psi p_0'(\psi), \tag{5.45}$$

which is again rearranged to

$$\frac{\partial}{\partial\vartheta} p_n + \mathrm{i}nqp_n = -p_0'(\psi)\frac{B_n^\psi}{B_0^\vartheta} \tag{5.46}$$

and Fourier transformed to

$$\mathrm{i}mp_{mn} + \mathrm{i}nqp_{mn} = -p_0'(\psi)\left[\frac{B_n^\psi}{B_0^\vartheta}\right]_m, \tag{5.47}$$

which is finally rearranged to

$$p_{mn} = \frac{-p_0'(\psi)}{\mathrm{i}(m+nq)}\left[\frac{B_n^\psi}{B_0^\vartheta}\right]_m. \tag{5.48}$$

When a resonance occurs at poloidal mode number m_0, around the affected flux surface the pressure perturbation is dominated by the associated Fourier coefficient,

$$p_{m_0 n} \gg p_{mn} \quad \forall m \neq m_0 \tag{5.49}$$

and thus

$$p_n \approx \mathrm{e}^{\mathrm{i}m_0\vartheta} p_{m_0 n}. \tag{5.50}$$

Putting everything together, we approximate the sheet current by

$$\left[\frac{J^\parallel}{B}\right]_{mn} = C_{mn}p_{mn}\delta_{mm_0}, \tag{5.51}$$

or, after an inverse Fourier transform,

$$J_n^\parallel = C_{m_0 n}B_0 p_n. \tag{5.52}$$

For a given set of C_{mn} values, we project $J_n^\parallel$ onto currents I_i and I_o, which we add to the values computed in section 5.2 in between the flux surfaces where q is closest to the respective m/n resonance. I_f has no contribution from this parallel current, so I_φ is modified to uphold divergence-freeness.

Chapter 6

Preprocessing of Input Data

Prior to starting iterations, some input data has to be supplied, namely the following:

- coordinates of grid points, the numbering of grid points, and triangles including edge adjacency list – described in section 6.1;
- the equilibrium magnetic field $\boldsymbol{B}_0$ from which the grid is generated;
- the vacuum perturbation field $\delta\boldsymbol{B}_\mathrm{v}$ and
- optionally the equilibrium pressure p_0.

Additionally, a configuration file exists to specify the behavior of the implemented algorithms and data input/output.

The equilibrium field $\boldsymbol{B}_0$ is assumed to be available in GEQDSK format, shortly summarized by Lao [11]. It consists of data points given on a rectangular grid which are fitted from measurements to the Grad–Shafranov equation. Parts of already existing code import such a file and generate a field-aligned grid as described in section 3.2 and specified in section 6.1. It also supplies values of $\boldsymbol{B}_0$ and its partial derivatives on arbitrary R, Z coordinates by interpolation with bicubic splines in R and Z based on eqs. (3.28) and (3.29). In the implementation of NEO-EQ, the necessary values on edge midpoints and shifted centroids are cached once before calculations start as to avoid repeated function calls to spline interpolation and possibly allow for other data sources. From $\boldsymbol{B}_0$, the safety factor q is computed as described in section 6.3.

While the equilibrium pressure p_0 should be available from the GEQDSK file and the equilibrium current $\boldsymbol{J}_0$ can be computed from the equilibrium field via Ampère's law as in eq. (2.2), another approach is possible. Since we have never used Ampère's law for equilibrium quantities, it is possible to choose a pressure profile and calculate J_0^φ to be consistent with the MHD equilibrium in eq. (2.1). The latter is the Pfirsch–Schlüter current and its calculation is outlined in section 6.2. The simplest approach to the pressure profile assumes a linear profile

for the particle density n and temperature T,

$$n^{(k)} = n_{\min} + \frac{\psi^{(k)} - \psi_{\min}}{\psi_{\text{axis}} - \psi_{\min}}(n_{\text{axis}} - n_{\min}), \tag{6.1}$$

$$T^{(k)} = T_{\min} + \frac{\psi^{(k)} - \psi_{\min}}{\psi_{\text{axis}} - \psi_{\min}}(T_{\text{axis}} - T_{\min}), \tag{6.2}$$

where k refers to the index of the flux surface. The subscripts "min" and "axis" indicate the value at the plasma edge and the magnetic axis, respectively. The configurable values are then n_{axis} and T_{axis} as well as $n_{\min}$ and $T_{\min}$. From these, the pressure is calculated by the ideal gas law:

$$p_0 = nk_{\text{B}}T. \tag{6.3}$$

Additionally, with the formulae given above, one can also derive an expression for the equilibrium pressure gradient:

$$p_0'(\psi) = n'(\psi)k_{\text{B}}T + nk_{\text{B}}T'(\psi) = \frac{(n_{\text{axis}} - n_{\min})k_{\text{B}}T + nk_{\text{B}}(T_{\text{axis}} - T_{\min})}{\psi_{\text{axis}} - \psi_{\min}}. \tag{6.4}$$

Thus all necessary equilibrium quantities are established.

The vacuum perturbation field $\delta\boldsymbol{B}_{\text{v}}$ is calculated beforehand from the external coil currents I_{c} by the Biot–Savart law (eq. (2.6)) on a regular grid in (R, φ, Z) coordinates, from which the fluxes through triangle edges are computed for representation as Raviart–Thomas elements.

6.1 Grid Implementation

Since the grid is field-aligned, there are a few conventions to be considered compared to more arbitrary grids. The code has to "find its way", so we make assumptions on numbering.

The number of flux surfaces realized on the grid is known and referred to as n_{flux}. The numbers increase going outward from the magnetic axis, which is *not* included and thus gets the index 0. Flux variables like ψ, p_0 and $p_0'(\psi)$ are calculated at these flux surfaces and use the same indexing scheme. Others, like q, are calculated *between* flux surfaces and are called half-grid quantities. In this case, the index refers to the outer or enclosing flux surface and starts at 1. When we need half-grid quantities at full-grid positions or vice versa, we use linear interpolated between neighboring values, with one exception: If an interpolation point lies outside the separatrix, we use an appropriate interpolation point on the separatrix instead.

Node numbering starts from 1 at the magnetic axis, increasing towards the separatrix. Then, the nodes on the enclosing flux surface (index 1) are enumerated counter-clockwise, starting with the node lying on the line connecting the magnetic axis and the X point. Then the next enclosing flux surface (index 2) is enumerated, and so on. This way, a simple bijection

between "global" node numbering and the "local" numbering on a specific flux surface can be implemented. The flux surface indexing is the same as for full-grid quantities, and the number of nodes per flux surface needs to be known. Figure 6.1a illustrates global node numbering.

Triangle numbering operates on similar assumptions, albeit with flux surface indexing akin to half-grid quantities. The innermost triangle strip (index 1) is enumerated first, starting at index 1 for the triangle formed by nodes 1, 2, and 3. It also goes counter-clockwise, and on each flux surface it starts with the triangle whose edge i lies on the line between the magnetic axis and the X point, i.e., it follows node numbering. Again, local numbering on a triangle strip can be converted to global numbering when the number of triangles is known. Figure 6.1b illustrates global triangle numbering.

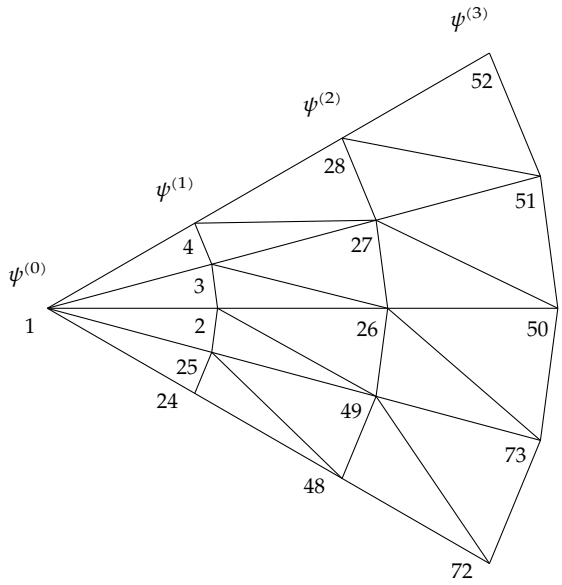

(a) Global numbering scheme for nodes. Local indices refer to the flux surfaces on which the nodes reside. The mapping from local to global numbering would then produce, for example, $(0,1) \to 1$, $(1,1) \to 2$, $(1,24) \to 25$, $(2,1) \to 26$, $(2,24) \to 49$, $(3,1) \to 50$ and so on.

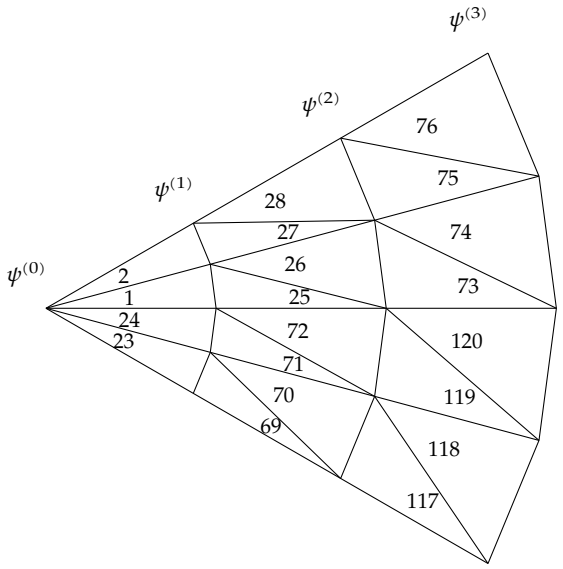

(b) Global numbering scheme for triangles. Local indices refer to the *enclosing* flux surface of the triangle. The mapping from local to global numbering would then produce, for example, $(1,1) \to 1$, $(1,24) \to 24$, $(2,1) \to 25$, $(2,48) \to 72$, $(3,1) \to 73$ and so on.

Figure 6.1: Juxtaposition of numbering schemes for nodes and triangles. In both drawings, the flux surfaces are indicated by $\psi^{(k)}$ with k being the index of the flux surface. There are 24 nodes on each flux surface and the horizontal line connects to the X point, which means numbering on each flux surface starts there.

Associated with each triangle are local indices, i.e., 1 to 3, for nodes and edges. The global node number is saved for each local node number. The edges do not have a global index, and they are numbered in a fashion that edge 1 connects node 1 to 2, edge 2 connects node 2 to 3, and edge 3 connects node 3 to 1. When the index of node F is known and the aforementioned conventions are followed, we can map the symbolic designations f, i, o to the local edge index,

F, I, O to the local (and global) node index and edge vectors $\boldsymbol{l}$ can be given in counter-clockwise direction. Furthermore, an adjacency list is constructed, giving any triangle's neighbor on a given edge and the local edge number in the neighboring triangle.

Scalar quantities like p_n are indexed by global node number and vector quantities like $\boldsymbol{B}_n$ and $\boldsymbol{J}_n$ are indexed by global triangle number and local edge number. The latter convention involves some redundancy as it takes twice the storage that would be necessary, but it also allows for consistency checks and more straightforward implementation.

6.2 Toroidal Unperturbed Current

Since $\boldsymbol{B}_0$ and p_0 are directly available as input data, but $\boldsymbol{J}_0$ is not, the latter will be derived below from eq. (2.1), the condition of divergence-freeness and symmetry considerations.

We take a cross-product of eq. (2.1) by $\boldsymbol{B}_0$:

$$\begin{aligned}\boldsymbol{B}_0 \times (\boldsymbol{J}_0 \times \boldsymbol{B}_0) &= B_0^2 \boldsymbol{J}_0 - (\boldsymbol{B}_0 \cdot \boldsymbol{J}_0)\boldsymbol{B}_0 \\ &= B_0^2 (\boldsymbol{J}_0 - J_0^{\parallel} \boldsymbol{h}_0) \\ &= B_0^2 \boldsymbol{J}_0^{\perp}. \end{aligned} \tag{6.5}$$

Therefore

$$\boldsymbol{J}_0^{\perp} = \frac{-c \nabla p_0 \times \boldsymbol{B}_0}{B_0^2}, \tag{6.6}$$

which is the diamagnetic current density. For the parallel current density we use

$$\begin{aligned} 0 = \nabla \cdot \boldsymbol{J}_0 &= \nabla \cdot \boldsymbol{J}_0^{\perp} + \nabla \cdot (J_0^{\parallel} \boldsymbol{h}_0) \\ &= -c \nabla \cdot \frac{\nabla p_0 \times \boldsymbol{B}_0}{B_0^2} + \boldsymbol{B}_0 \cdot \nabla \frac{J_0^{\parallel}}{B_0}. \end{aligned} \tag{6.7}$$

In symmetry flux coordinates $(\varrho, \varphi, \vartheta)$ and Jacobian $\sqrt{g}$ outlined in section 3.1, the divergence of the diamagnetic current is

$$\begin{aligned} \nabla \cdot \boldsymbol{J}_0^{\perp} &= -\frac{c}{\sqrt{g}} \frac{\partial}{\partial u^k} \left[\frac{\sqrt{g}}{B_0^2} \left(\nabla p_0 \times \boldsymbol{B}_0 \right)^k \right] \\ &= -\frac{c}{\sqrt{g}} \frac{\partial}{\partial u^k} \left(\frac{\sqrt{g}}{B_0^2} \frac{\varepsilon^{ijk}}{\sqrt{g}} \frac{\partial p_0}{\partial u^i} B_{0j} \right) \\ &= -\frac{c p_0'(\varrho) B_{0\varphi}}{\sqrt{g}} \frac{\partial}{\partial \vartheta} \frac{1}{B_0^2}, \end{aligned} \tag{6.8}$$

since p_0 and $B_{0\varphi}$ are constant on a flux surface, $\frac{\partial p_0}{\partial \vartheta} = 0$ and due to axisymmetry $\frac{\partial}{\partial \varphi} = 0$ for

equilibrium quantities. The divergence of the parallel current is

$$\nabla \cdot (J_0^{\parallel} \boldsymbol{h}_0) = \boldsymbol{B}_0 \cdot \nabla \frac{J_0^{\parallel}}{B_0} = B_0^{\vartheta} \frac{\partial}{\partial \vartheta} \frac{J_0^{\parallel}}{B_0}. \tag{6.9}$$

With $\sqrt{g} B_0^{\vartheta} = \psi'(\varrho) = -1$ as a flux surface quantity, there are no dependencies of ϑ in front of the derivatives:

$$-c p_0'(\varrho) B_{0\varphi} \frac{\partial}{\partial \vartheta} \frac{1}{B_0^2} + \psi'(\varrho) \frac{\partial}{\partial \vartheta} \frac{J_0^{\parallel}}{B_0} = 0. \tag{6.10}$$

Direct integration and a change of variables and notation as in

$$\frac{p_0'(\varrho)}{\psi'(\varrho)} = \frac{\frac{\partial p_0}{\partial \varrho}}{\frac{\partial \psi}{\partial \varrho}} = \frac{\partial p_0}{\partial \psi} = p_0'(\psi) \tag{6.11}$$

yields

$$\frac{-c p_0'(\psi) B_{0\varphi}}{B_0^2} + \frac{J_0^{\parallel}}{B_0} = C(\psi). \tag{6.12}$$

With the extra condition of the flux surface average[1] $\left\langle J_0^{\parallel} B_0 \right\rangle = 0$ for testing without bootstrap and inductive current, we obtain

$$-c p_0'(\psi) B_{0\varphi} = C(\psi) \left\langle B_0^2 \right\rangle. \tag{6.13}$$

In general,

$$C(\psi) = -\frac{c p_0'(\psi) B_{0\varphi}}{\left\langle B_0^2 \right\rangle} D(\psi), \tag{6.14}$$

with $D(\psi)$ set to 1 for now and modified for the more general case $\left\langle J_0^{\parallel} B_0 \right\rangle \not\equiv 0$. Inserting this back into eq. (6.12) yields

$$J_0^{\parallel} = \frac{c p_0'(\psi) B_{0\varphi}}{B_0} \left(1 - \frac{B_0^2}{\left\langle B_0^2 \right\rangle} D(\psi) \right). \tag{6.15}$$

For the unperturbed toroidal current density, we have

$$J_0^{\varphi} = J_0^{\parallel} h_0^{\varphi} + \boldsymbol{J}_0^{\perp} \cdot \nabla \varphi, \tag{6.16}$$

[1] See eq. (3.38), but note that it is not actually evaluated here.

where

$$\begin{aligned} J_0^{\parallel} h_0^{\varphi} &= \frac{c p_0'(\psi) B_{0\varphi}}{B_0} \frac{B_0^{\varphi}}{B_0} \left(1 - \frac{B_0^2}{\left\langle B_0^2 \right\rangle} D(\psi) \right) \\ &= c p_0'(\psi) \frac{\left(B_0^{\text{tor}} \right)^2}{B_0^2} \left(1 - \frac{B_0^2}{\left\langle B_0^2 \right\rangle} D(\psi) \right) \\ &= c p_0'(\psi) \left(B_0^{\text{tor}} \right)^2 \left(\frac{1}{B_0^2} - \frac{D(\psi)}{\left\langle B_0^2 \right\rangle} \right). \end{aligned} \tag{6.17}$$

and

$$\begin{aligned} \boldsymbol{J}_0^{\perp} \cdot \nabla \varphi &= \frac{-c p_0'(\psi) \nabla \varphi \cdot (\nabla \psi \times \boldsymbol{B}_0)}{B_0^2} \\ &= \frac{-c p_0'(\psi) \boldsymbol{B}_0 \cdot (\nabla \varphi \times \nabla \psi)}{B_0^2} \\ &= \frac{c p_0'(\psi)}{B_0^2} \boldsymbol{B}_0^{\text{pol}} \cdot \boldsymbol{B}_0 \end{aligned} \tag{6.18}$$

$$= c p_0'(\psi) \frac{\left(B_0^{\text{pol}} \right)^2}{B_0^2}. \tag{6.19}$$

It follows that

$$J_0^{\varphi} = c p_0'(\psi) \left(\frac{\left(B_0^{\text{pol}} \right)^2 + \left(B_0^{\text{tor}} \right)^2}{B_0^2} - \frac{\left(B_0^{\text{tor}} \right)^2}{\left\langle B_0^2 \right\rangle} D(\psi) \right) = c p_0'(\psi) \left(1 - \frac{\left(B_0^{\text{tor}} \right)^2}{\left\langle B_0^2 \right\rangle} D(\psi) \right). \tag{6.20}$$

6.3 Safety Factor

Computing the safety factor from eq. (3.30) would require the calculation of ϑ coordinate lines from $\boldsymbol{B}_0$. An equivalent definition from D'haeseleer et al. [4] involves the toroidal flux ψ_{tor}, which in our choice of coordinates is given by

$$\psi_{\text{tor}} = \frac{1}{(2\pi)^2} \int \mathrm{d}V \, \boldsymbol{B}_0 \cdot \nabla \varphi = \frac{1}{2\pi} \int \mathrm{d}R \, \mathrm{d}Z \, R B_0^{\varphi} = \frac{1}{2\pi} \int \mathrm{d}R \, \mathrm{d}Z \, B_{0(\varphi)}. \tag{6.21}$$

Note that $\psi_{\text{tor}} < 0$ and $\psi_{\text{tor}}'(\varrho) < 0$. The safety factor is then given by

$$q = \frac{\psi_{\text{tor}}'(\varrho)}{\psi_{\text{pol}}'(\varrho)} = \frac{-\psi_{\text{tor}}'(\psi)}{-\psi_{\text{pol}}'(\psi)} = \frac{\mathrm{d}\psi_{\text{tor}}}{\mathrm{d}\psi} = \frac{1}{2\pi} \frac{\mathrm{d}}{\mathrm{d}\psi} \int \mathrm{d}R \, \mathrm{d}Z \, B_{0(\varphi)}. \tag{6.22}$$

This flux quantity can be evaluated numerically at half-grid steps by adding up $B_{0(\varphi)}$ inside the volume between two flux surfaces and dividing by the the difference in ψ:

$$q \approx \frac{1}{2\pi\Delta\psi} \sum_k B_{0(\varphi)}(\Omega^{(k)}) S_{\Omega^{(k)}}, \tag{6.23}$$

where the sum is taken over all triangles Ω inside a triangle strip, and S_Ω is the respective triangle surface area. Note that both $B_{0(\varphi)}$ and $\Delta\psi$ are negative, so q is positive overall.

Chapter 7

Construction of Test Cases

Along with comparison to results from kinetic computations, we consider special test cases altering different components of the calculation. In section 7.1, $\delta \boldsymbol{B}_{\mathrm{v}}$ is not taken from Biot–Savart calculations of currents in external coils as per eq. (2.6) and chapter 6, but constructed directly to avoid resonances, at least in the first iteration step. Section 7.2 instead looks at the analytical solution in the cylindrical limit on a circular cross-section obtained from KiLCA [8], effectively changing the grid geometry.

7.1 Generating a Non-Resonant Vacuum Perturbation

The axisymmetric equilibrium field $\boldsymbol{B}_0$ lies on nested flux surfaces $\psi = \text{const.}$, meaning

$$\boldsymbol{B}_0 \cdot \nabla \psi = B_0^{\psi} = 0.$$

If the perturbed field shall still lie on distorted, but not broken, flux surfaces (non-resonant, without magnetic islands), a new flux surface label $\psi + \delta\psi$ must exist fulfilling

$$(\boldsymbol{B}_0 + \delta \boldsymbol{B}) \cdot \nabla (\psi + \delta\psi) = 0$$

for the perturbed magnetic field $\boldsymbol{B}_0 + \delta \boldsymbol{B}$, where $\delta\psi$ remains small and continuous within the plasma. In that case we can use a linear order expansion

$$\underbrace{\boldsymbol{B}_0 \cdot \nabla \psi}_{=0} + \boldsymbol{B}_0 \cdot \nabla \delta\psi + \delta \boldsymbol{B} \cdot \nabla \psi + \mathcal{O}(\delta^2) = 0, \tag{7.1}$$

or in coordinate form with symmetry flux coordinates $(\varrho, \varphi, \vartheta)$ outlined in section 3.1,

$$B_0^{\vartheta} \frac{\partial}{\partial \vartheta} \delta\psi + B_0^{\varphi} \frac{\partial}{\partial \varphi} \delta\psi + \delta B^{\varrho} \psi'(\varrho) = 0. \tag{7.2}$$

Here we have used $\nabla\psi = \psi'(\varrho)\nabla\varrho$. Further, $\psi'(\varrho) = -1$. With safety factor

$$q = \frac{B_0^\varphi}{B_0^\vartheta}$$

and dividing by B_0^ϑ, we obtain

$$\left(\frac{\partial}{\partial\vartheta} + q\frac{\partial}{\partial\varphi}\right)\delta\psi = \frac{\delta B^\varrho}{B_0^\vartheta} = -\sqrt{g}\delta B^\varrho = \sqrt{g}\delta B^\psi. \tag{7.3}$$

Written in terms of toroidal Fourier harmonics m, n in ϑ, φ the equation becomes

$$\psi_{mn} = \frac{\left[\sqrt{g}\delta B^\psi\right]_{mn}}{\mathrm{i}(m+nq)} = \frac{\left[\sqrt{g}B_n^\psi\right]_m}{\mathrm{i}(m+nq)}.$$

$\sqrt{g}$ depends also on ϑ, so poloidal harmonics m have to be taken outside the bracket here. In order to fulfill the original requirement not to break flux surfaces, ψ_{mn} must never diverge, so $m + nq$ must not become zero. We can avoid such resonant surfaces if

$$\left[\sqrt{g}B_n^\psi\right]_m \stackrel{!}{=} 0 \tag{7.4}$$

for all possible m that could lead to a resonance. The simplest way to do so is to make $\sqrt{g}B_n^\psi$ a flux function, possessing only the poloidally symmetric harmonic $m = 0$. More generally, also $-m < nq_{\min}$ and $-m > nq_{\max}$ are possible, but for nonzero m a transformation to the flux angle ϑ has to be computed explicitly.

Using the Jacobian of symmetry flux coordinates from eq. (3.31), we obtain

$$\psi_{mn} = \frac{q}{\mathrm{i}(m+nq)}\left[\frac{R^2}{B_{0\varphi}}B_n^\psi\right]_m \tag{7.5}$$

and so, to generate a non-resonant field, we are allowed to use any value

$$B_n^\psi = C(\psi)\frac{B_{0\varphi}}{R^2}, \tag{7.6}$$

where $C(\psi)$ is a flux function. The other components of $\delta\boldsymbol{B}$ are not relevant for the resonance condition and just need to fulfill divergence-freeness. Thus we proceed as in section 5.2 and find fluxes through triangle edges:

$$\int_{\Gamma_\mathrm{i},\Gamma_\mathrm{o}} R\boldsymbol{B}_n^\mathrm{pol}\cdot\boldsymbol{n}\,\mathrm{d}l = -\int_{\Gamma_\mathrm{f}} R\boldsymbol{B}_n^\mathrm{pol}\cdot\boldsymbol{n}\,\mathrm{d}l - \mathrm{i}n\int_\Omega RB_n^\varphi\,\mathrm{d}R\,\mathrm{d}Z. \tag{7.7}$$

As for currents we use the notation Ψ_k for weighted magnetic fluxes through edges as in

eq. (3.44),

$$\Psi_k = \int_{\Gamma_k} R\boldsymbol{B}_n^{\mathrm{pol}} \cdot \boldsymbol{n}\,\mathrm{d}l \approx R(\Gamma_k)\boldsymbol{B}_n^{\mathrm{pol}}(\Gamma_k) \cdot \boldsymbol{n}_k, \tag{7.8}$$

and, differing from the procedure in section 5.2, the same for the weighted toroidal magnetic flux Ψ_φ as per eq. (3.48),

$$\Psi_\varphi = \int_\Omega RB_n^\varphi\,\mathrm{d}R\,\mathrm{d}Z \approx S_\Omega\, R(\Omega)B_n^\varphi(\Omega), \tag{7.9}$$

resulting in a shortened notation for eq. (7.7) where the system of equations to be assembled is more apparent:

$$\Psi_\mathrm{i} + \Psi_\mathrm{o} = -\Psi_\mathrm{f} - \mathrm{i}n\Psi_\varphi. \tag{7.10}$$

Again, the flux through edge f is fixed, so we rearrange eq. (3.54) and get

$$\Psi_\mathrm{f} \approx 2R(\Gamma_\mathrm{f})B_n^\psi(\Gamma_\mathrm{f})\frac{S_{\Omega^{(+1)}} + S_{\Omega^{(-1)}}}{\psi^{(+1)} - \psi^{(-1)}}, \tag{7.11}$$

where B_n^ψ is given by eq. (7.6).

The system of linear equations to solve is

$$K_{jk}\Psi^{(k)} = s_j \quad \forall j,k = 1,2,\dots,N, \tag{7.12}$$

with

$$K_{jk} = \delta_{j-1,k} - \delta_{jk} \to \hat{K} = \begin{pmatrix} -1 & 1 & 0 & \dots & 0 \\ 0 & -1 & 1 & \dots & 0 \\ 0 & 0 & -1 & \dots & 0 \\ \vdots & \vdots & \vdots & \ddots & \vdots \\ 1 & 0 & 0 & \dots & -1 \end{pmatrix} \tag{7.13}$$

and

$$s_j = -\Psi_\mathrm{f}^{(j)} - \mathrm{i}n\Psi_\varphi^{(j)}. \tag{7.14}$$

Since any one column in $\hat{K}$ is a linear combination of all other columns, $\hat{K}$ is of rank $N-1$ and thus singular. To construct a solution, we first consider the homogenous case with $\boldsymbol{s} = \boldsymbol{0}$, which also determines the toroidal flux. The non-zero solution for the remaining degrees of freedom then assumes the simple form

$$\Psi^{(k)} = C_0 \quad \forall k = 1,2,\dots,N, \tag{7.15}$$

with an arbitrary constant C_0. With local indices, the degrees of freedom are written as

$$\Psi_{\mathrm{i}}^{(k)} = -C_0, \qquad \Psi_{\mathrm{o}}^{(k)} = C_0 \qquad \Psi_{\varphi}^{(k)} = \frac{\mathrm{i}}{n}\Psi_{\mathrm{f}}^{(k)} \quad \forall k = 1, 2, \ldots, N. \tag{7.16}$$

This means that flux conservation, i.e. divergence-freeness, is fulfilled by balancing Ψ_φ with Ψ_{f} on each individual triangle and assigning a constant flux C_0 in poloidal direction to Ψ_{i} and Ψ_{o} over the entire triangle strip.

A consistent solution according to the Rouché-Capelli theorem can also be constructed for the inhomogeneous case, i.e. non-zero $\boldsymbol{s}$, as long as $\boldsymbol{s}$ is a linear combination of columns of K. Starting from the trivial (zero) solution to the homogeneous case and for a fixed k, we add to $\boldsymbol{s}$ the $(k+1)$-th column of $\hat{K}$, multiplied by another arbitrary constant C_k, resulting in

$$s_k = -\Psi_{\mathrm{f}}^{(k)} - \mathrm{i}n\Psi_{\varphi}^{(k)} = C_k, \tag{7.17}$$

$$s_{k+1} = -\Psi_{\mathrm{f}}^{(k+1)} - \mathrm{i}n\Psi_{\varphi}^{(k+1)} = -C_k. \tag{7.18}$$

Considering the two equations affected compared to the homogeneous case,

$$-\Psi^{(k-1)} + \Psi^{(k)} = C_k, \tag{7.19}$$

$$-\Psi^{(k)} + \Psi^{(k+1)} = -C_k, \tag{7.20}$$

we arrive at a particular solution

$$\Psi^{(k)} = C_k, \quad \Psi^{(j)} = 0 \quad \forall j \neq k. \tag{7.21}$$

The degrees of freedom differing from the solution to the zero solution (eq. (7.16) with $C_0 = 0$) are, given with local indices:

$$\Psi_{\mathrm{i}}^{(k)} = 0, \qquad \Psi_{\mathrm{o}}^{(k)} = C_k, \qquad \Psi_{\varphi}^{(k)} = \frac{\mathrm{i}}{n}\Psi_{\mathrm{f}}^{(k)} - \frac{\mathrm{i}}{n}C_k, \tag{7.22}$$

$$\Psi_{\mathrm{i}}^{(k+1)} = -C_k, \qquad \Psi_{\mathrm{o}}^{(k+1)} = 0, \qquad \Psi_{\varphi}^{(k+1)} = \frac{\mathrm{i}}{n}\Psi_{\mathrm{f}}^{(k+1)} + \frac{\mathrm{i}}{n}C_k. \tag{7.23}$$

This means that, compared to the zero solution, a change C_k in the flux across the associated edge of adjacent triangles in one triangle strip is accomodated by a change in the toroidal flux of these triangles.

We can repeat the approach outlined above for different values of k. Linear superposition of the solutions to the homogeneous and inhomogeneous cases then yields the most general solution,

$$\Psi_{\mathrm{i}}^{(k)} = -C_0 - C_{k-1}, \quad \Psi_{\mathrm{o}}^{(k)} = C_0 + C_k, \quad \Psi_{\varphi}^{(k)} = \frac{\mathrm{i}}{n}\Psi_{\mathrm{f}}^{(k)} + \frac{\mathrm{i}}{n}C_{k-1} - \frac{\mathrm{i}}{n}C_k \quad \forall k = 1, 2, \ldots, N. \tag{7.24}$$

Now, to assign sensible values to the arbitrary constants, consider the solution to the homogeneous sytem of equations. Since edge f alternates between inner and outer flux surface for all but the innermost triangle strip, $\boldsymbol{n}_\mathrm{f}$ will also alternate between pointing inwards and outwards. Thus Ψ_f will alternate signs too, but it is consistent along one flux surface. Since Ψ_φ depends linearly on Ψ_f, on any one triangle the sign of $B_{n(\varphi)}$ will differ from all three adjacent triangles, except for the innermost triangle strip. The resulting field is then clearly dependent on the choice of the grid. The procedure described before can be used to alleviate this problem. On every pair of triangles $\Omega^{(2k)}$ and $\Omega^{(2k+1)}$ – which originally result from diagonally dividing a more regular quadrilateral – we average Ψ_φ and set C_{2k} to the deviation to counterbalance the change:

$$C_{2k} = \frac{\mathrm{i}}{2n}\left(\Psi_\mathrm{f}^{(2k)} - \Psi_\mathrm{f}^{(2k+1)}\right) \quad \forall k = 0, 1, \dots, \frac{N}{2} - 1. \tag{7.25}$$

7.2 Analytical Solution for Very Large Aspect Ratios

To derive an analytical approximation, a very large major radius R_0 – and thus aspect ratio – is considered for a ring torus, i.e., with a circular cross-section. The torus is "unbent" and the toroidal geometry is effectively transformed to cylindrical geometry with a very thin and elongated cylinder and periodic boundary conditions. To distinguish this cylinder from the cylindrical coordinates (R, φ, Z) established in section 3.1, we use coordinates (r, θ, z) for the former:

$$R = R_0 + r\cos\theta, \qquad Z = r\sin\theta, \qquad \varphi = \frac{z}{R_0}. \tag{7.26}$$

Thus r corresponds to the minor radius and the pseudoradial component ϱ, z points in the φ direction in the infinitesimal limit and θ corresponds to the poloidal angle ϑ, albeit defined as a geometrical angle and not field-aligned. As for toroidal geometry, a Fourier series expansion is possible for periodic coordinates:

$$\delta\boldsymbol{B}(r, \theta, z) = \sum_{n=-\infty}^{\infty}\sum_{m=-\infty}^{\infty} \boldsymbol{B}_{mn}(r)\mathrm{e}^{\mathrm{i}m\theta}\mathrm{e}^{\mathrm{i}k_z z}. \tag{7.27}$$

Here, k_z is a wavenumber given by

$$k_z = \frac{n}{R_0}, \tag{7.28}$$

ensuring the same same periodicity $2\pi R_0$ as for the toroidal geometry. In the same sense, the wavenumber k_θ is defined as

$$k_\theta = \frac{m}{r} \tag{7.29}$$

and both are combined in the wavevector $\boldsymbol{k}$ as

$$\boldsymbol{k} = k_z \hat{\boldsymbol{e}}_z + k_\theta \hat{\boldsymbol{e}}_\theta. \tag{7.30}$$

Note that, due to the cylindrical geometry, there is no mode coupling among poloidal modes. As before, we only consider a single toroidal mode number n.

The general solution for the radial component in this geometry, on which KiLCA code is based, is given by eq. (5) in the paper by Heyn et al. [7]. For the vacuum perturbation $\delta\boldsymbol{B}_\mathrm{v}$ it reduces to

$$\frac{\partial}{\partial r}\frac{r}{k^2}\frac{\partial B_{mnr}}{\partial r} - rB_{mnr}\left(1 - \frac{\partial}{\partial r}\frac{1}{rk^2}\right) = 0 \tag{7.31}$$

Before attempting to solve eq. (7.31), we consider the constraints on the remaining components. Applying Ampère's law and taking into account the lack of associated current in the plasma volume, we get

$$0 = \frac{4\pi}{c}\sqrt{g}J^\theta = \sqrt{g}\left(\nabla \times \delta\boldsymbol{B}_\mathrm{v}\right)^\theta = \frac{\partial}{\partial z}\delta B_{\mathrm{v}r} - \frac{\partial}{\partial r}\delta B_{\mathrm{v}z}. \tag{7.32}$$

Taking the Fourier transform as $\frac{\partial}{\partial z} \to \mathrm{i}k_z$ yields

$$0 = \mathrm{i}k_z B_{mnr} - \frac{\partial}{\partial r}B_{mnz}. \tag{7.33}$$

The condition of zero divergence then gives a relation for the third component $\delta B^\theta_\mathrm{v}$:

$$0 = \sqrt{g}\nabla \cdot \delta\boldsymbol{B}_\mathrm{v} = \frac{\partial}{\partial r}(r\delta B^r_\mathrm{v}) + r\frac{\partial}{\partial\theta}\delta B^\theta_\mathrm{v} + r\frac{\partial}{\partial z}\delta B^z_\mathrm{v}. \tag{7.34}$$

Applying the Fourier again with $\frac{\partial}{\partial\theta} \to \mathrm{i}m$ yields

$$0 = \frac{\partial}{\partial r}(rB_{mnr}) + \mathrm{i}mB^\theta_{mn} + \mathrm{i}k_z rB_{mnz}. \tag{7.35}$$

For problems in cylindrical geometry, the radial solution typically involves Bessel functions. We start with

$$B_{mnz} = \mathrm{i}CI_m(k_z r), \tag{7.36}$$

where I_m is the modified Bessel function of the first kind of order m and C is an arbitrary integration constant that scales the magnitude of the solution. Inserting this into eq. (7.33), we get at

$$B_{mnr} = -\frac{\mathrm{i}}{k_z}\frac{\partial}{\partial r}B_{mnz} = \frac{C}{k_z}\frac{\partial}{\partial r}I_m(k_z r) = CI'_m(k_z r), \tag{7.37}$$

where the derivative of I_m is taken with respect to the entire argument, not only r. By insertion[1], one can check that eq. (7.37) solves eq. (7.31), so we proceed to calculate $\delta B_{\mathrm{v}}^{\theta}$ from eq. (7.35). Using functional identities of the Bessel functions[2], one arrives at

$$B_{mn\theta} = \mathrm{i}\frac{m}{k_z} C I_m(k_z r). \tag{7.38}$$

Since $I_{-m}(k_z r) = I_m(k_z r)$, this is the only vector component that changes with a negative mode number m. Even though there is no mode coupling in this geometry, our calculations are done in toroidal geometry, hence mode coupling is expected; thus we restrict ourselves to a single poloidal mode number m and take the Fourier transform, i.e.

$$\boldsymbol{B}_n(r, \vartheta) = \boldsymbol{B}_{mn}(r)\mathrm{e}^{\mathrm{i}m\theta}. \tag{7.39}$$

To convert back to (R, φ, Z) vector components, we use eq. (7.26) and arrive at

$$B_n^R = B_n^r \frac{\partial R}{\partial r} + B_n^\theta \frac{\partial R}{\partial \theta} = B_n^r \cos\theta - r B_n^\theta \sin\theta, \tag{7.40}$$

$$B_n^Z = B_n^r \frac{\partial Z}{\partial r} + B_n^\theta \frac{\partial Z}{\partial \theta} = B_n^r \sin\theta + r B_n^\theta \cos\theta, \tag{7.41}$$

$$B_n^\varphi = B_n^z \frac{\partial \varphi}{\partial z} = \frac{1}{R_0} B_n^z. \tag{7.42}$$

Note that the same conversions apply in the secondary cylindrical coordinate system analogously, e.g. $r B_n^\theta = B_{n(\theta)}$. Furthermore, since R_0 is large and $R \approx R_0$, the physical components in eq. (7.42) are approximately equal:

$$B_{n(\varphi)} = R B_n^\varphi = \frac{R}{R_0} B_n^z \approx B_n^z. \tag{7.43}$$

Up to this point, calculations have been performed in the cylindrical geometry used by KiLCA code where the torus is explicitly bent into a cylinder. To approximate this geometry in NEO-EQ code, we multiply R_0 by a scaling factor γ and implement the change by shifting the computational domain in the EFIT file (see chapter 6) to that value. Equation (7.26) then reads

$$\bar{R} = \gamma R_0 + r\cos\theta, \qquad \bar{Z} = r\sin\theta, \qquad \bar{\varphi} = \frac{z}{\gamma R_0}. \tag{7.44}$$

Effectively, the torus is stretched by "stitching together" γ cylinders with periodic boundary conditions. Consequently, we use wavenumbers

$$k_z = \frac{\bar{n}}{\gamma R_0}, \tag{7.45}$$

[1] into Mathematica
[2] again, Mathematica

which must be identical to the value from eq. (7.28), so we have

$$\bar{n} = \gamma n. \tag{7.46}$$

Furthermore, the fluxes in the EFIT file have to be scaled,

$$\bar{\psi} = \gamma \psi, \tag{7.47}$$

which results in an unchanged magnetic field and an inversely scaled safety factor,

$$\bar{q} = \frac{q}{\gamma}, \tag{7.48}$$

which is in turn consistent with a scaled toroidal mode number n and an unscaled poloidal mode number m. The solution computed by NEO-EQ code then has to be transformed to the cylindrical geometry of KiLCA code to allow for a comparison. Using trigonometric identities, we can invert eqs. (7.40) to (7.42) to yield

$$B_n^r = B_n^R \cos\theta + B_n^Z \sin\theta, \tag{7.49}$$

$$rB_n^\theta = B_n^Z \cos\theta - B_n^R \sin\theta, \tag{7.50}$$

$$B_n^z = R_0 B_n^\varphi \approx R B_n^\varphi = B_{n(\varphi)}. \tag{7.51}$$

The poloidal spectrum of this result is then approximated by a discrete Fourier transform:

$$\boldsymbol{B}_{mn}(r) = \frac{1}{N} \sum_{k=1}^{N} \boldsymbol{B}_n(r, \theta_k) \mathrm{e}^{-\mathrm{i}m\theta_k}, \quad \theta_k = \frac{2\pi k}{N}. \tag{7.52}$$

Here, N is the number of sample points, which is taken to be one per triangle in the triangle strip at given r.

Chapter 8

Test Results

In this chapter, some selected results from test cases are presented. The convergence of the iterative scheme from section 2.1 and the validity of the preconditioner from section 2.2 is examined. Results for the initial pressure response and poloidal modes are compared to those by Albert et al. [1, 2]. Finally, the large aspect ratio test case outlined in section 7.2 is explored in comparison with KiLCA code [8].

For test cases in ASDEX geometry, shot number 17151 and the time slice at 3.800 s is used for the equilibrium configuration. Figures 8.1 to 8.3 show ψ, p_0, and q from eqs. (3.27), (6.3) and (6.23), respectively. Density and temperature are proportional to ψ via eqs. (6.1) and (6.2). The values displayed here are for the high-density configuration with

$$n_{\text{axis}} = 5 \times 10^{13}\,\text{cm}^{-3}, \qquad n_{\text{min}} = 10^{11}\,\text{cm}^{-3}, \tag{8.1}$$

$$T_{\text{axis}} = 3\,\text{keV}, \qquad T_{\text{min}} = 2 \times 10^{1}\,\text{eV}, \tag{8.2}$$

while for the low-density configuration used in some test cases, the central density is lowered to

$$n_{\text{axis}} = 5 \times 10^{11}\,\text{cm}^{-3}. \tag{8.3}$$

If not noted otherwise, these are are the values used when referring to high-density and low-density test cases. Note that in all test cases, we use the toroidal mode number

$$n = 2. \tag{8.4}$$

8.1 Initial pressure response

Albert et al. [2] investigate the pressure response p_n to the vacuum perturbation $\delta \boldsymbol{B}_{\text{v}}$, i.e., without performing any iterations. We try to reproduce these results as a way to confirm

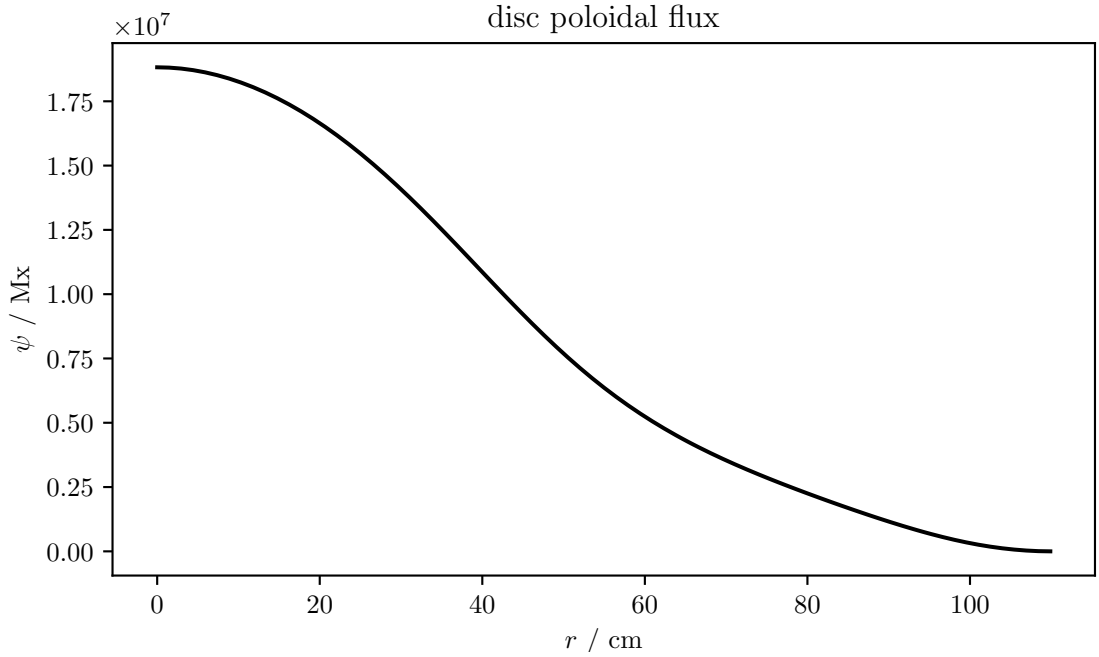

Figure 8.1: Disc poloidal flux of the equilibrium configuration. r is the minor radius measured from the magnetic axis to the X point.

the validity of our code. The first test case uses a non-resonant vacuum perturbation, as considered in section 7.1. Figure 8.4 shows the result from the reference, while fig. 8.5 shows our reproduction. For the real part, the relative error is on the order of machine precision – we expect a value of zero, as no resonances should occur. The imaginary parts show a gradient pattern and are visually indistinguishable. Hence, we consider the reconstruction of the non-resonant test case valid. The second test case involves the usual resonant vacuum perturbation, and in fig. 8.6 we compare the real parts, as only the real part is given in the reference. The positions of the resonances appear to agree; visual differences may be explained by the low picture resolution in the reference and possibly a different radial grid partitioning.

As a continuation of the work by Albert et al. [2], a self-consistent plasma response is obtained when current perturbation as per section 5.2 is taken into account and the preconditioner from section 2.2 is applied. The result after convergence of preconditioned iterations is depicted in fig. 8.7. The magnitude is reduced to about three quarters of the initial response pressure seen in fig. 8.6 and the imaginary part shows a similar resonant pattern as the real part. It should be noted that the values for density and temperature at the center that Albert et al. [2] report are actually the *difference* in density and temperature between the center and the separatrix. The effective values at the center are

$$n_{\text{axis}} = 7.2 \times 10^{13}\,\text{cm}^{-3}, \qquad T_{\text{axis}} = 4.3\,\text{keV}. \tag{8.5}$$

These values are used here for the sake of a meaningful comparison.

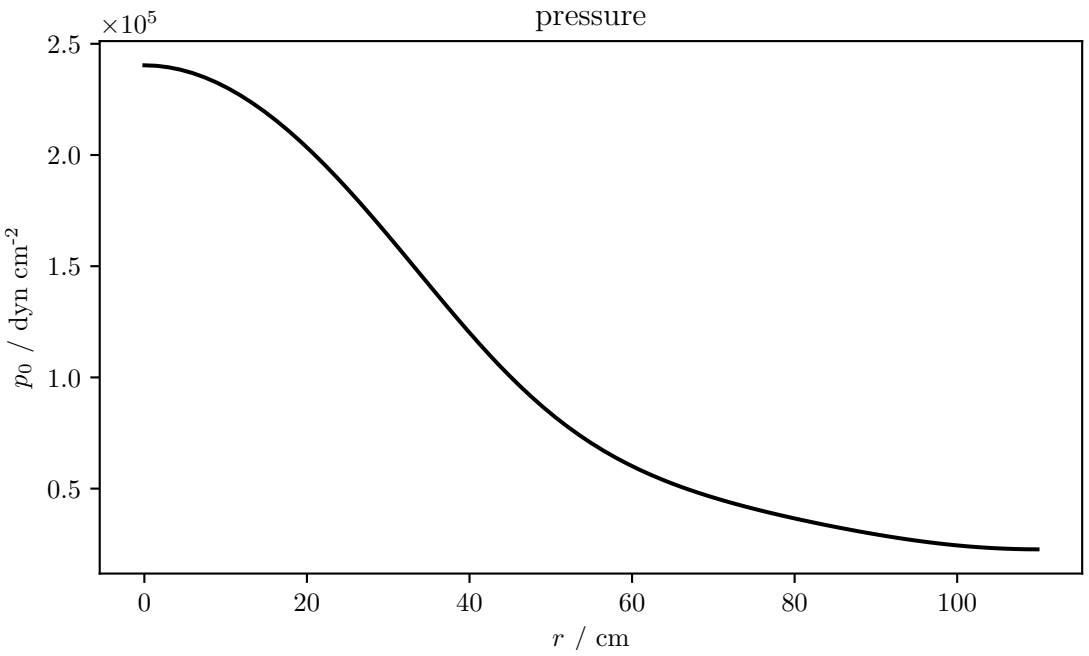

Figure 8.2: Pressure of the equilibrium configuration. r is the minor radius measured from the magnetic axis to the X point.

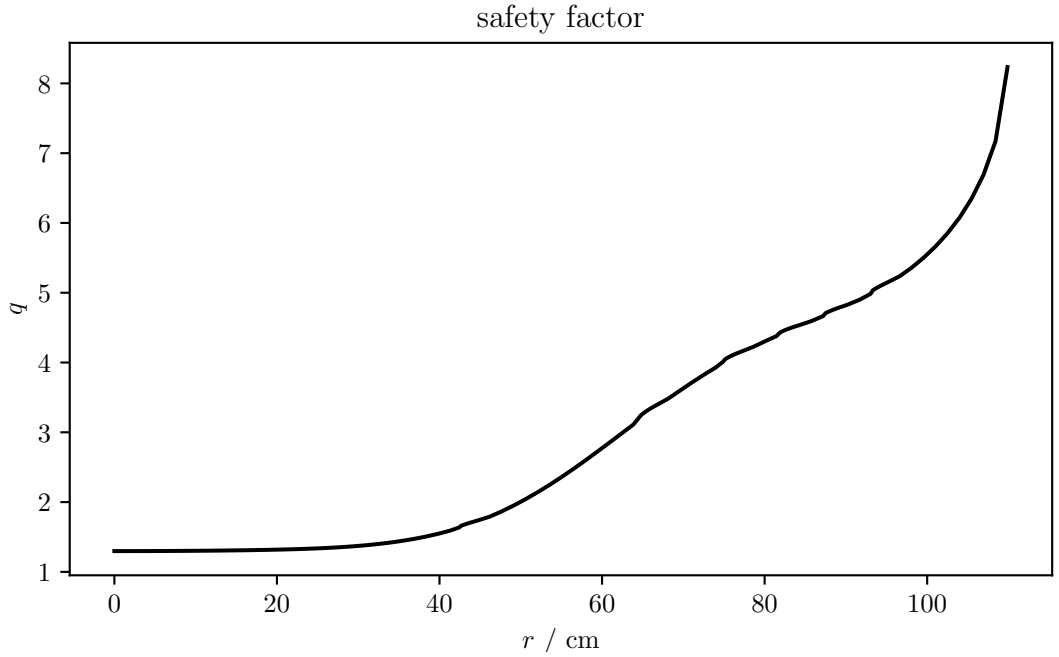

Figure 8.3: Safety factor of the equilibrium configuration. r is the minor radius measured from the magnetic axis to the X point.

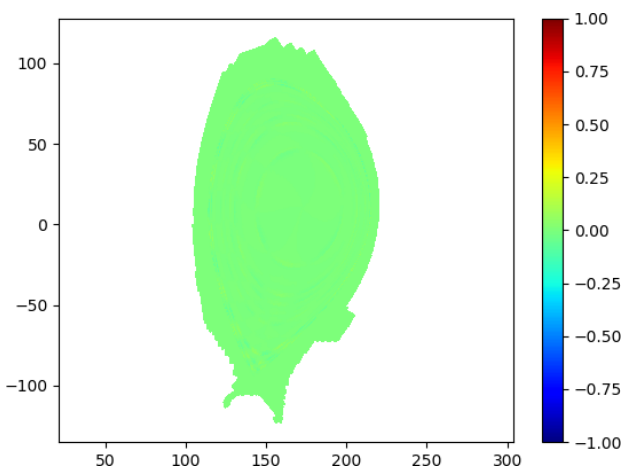

(a) Real part of response pressure p_n.

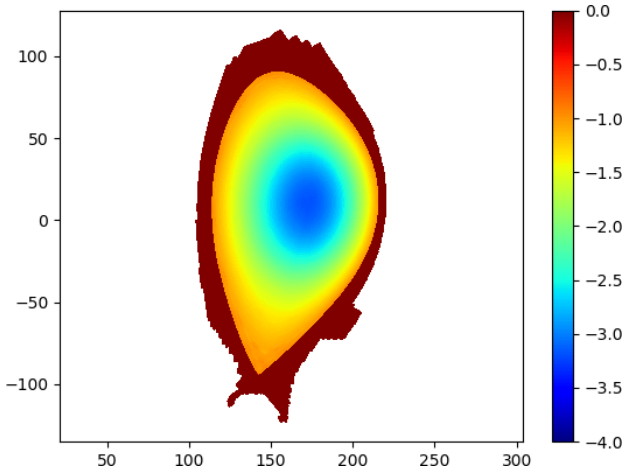

(b) Imaginary part of response pressure p_n.

Figure 8.4: Response pressure p_n for the non-resonant vacuum perturbation from fig. 1 in [2], which we aim to reproduce (see fig. 8.5). The real part of p_n is practically zero, while the imaginary part shows a gradient without any resonant effects. Values are given in Gaussian units.

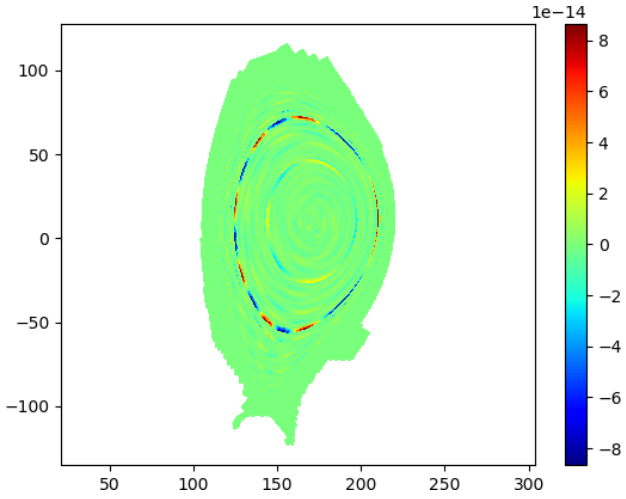

(a) Real part of response pressure p_n.

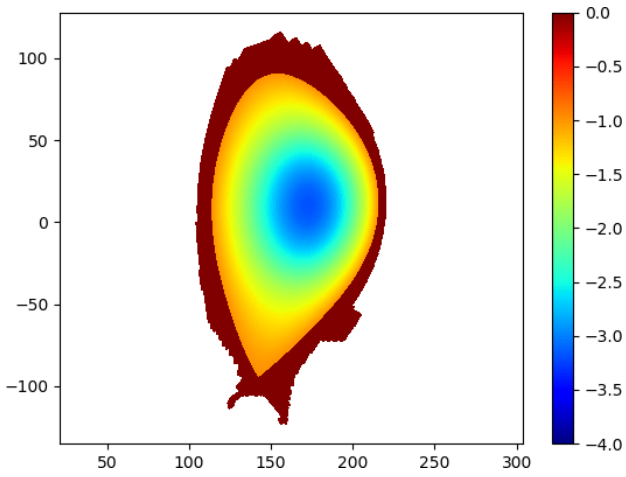

(b) Imaginary part of response pressure p_n.

Figure 8.5: Response pressure p_n for the non-resonant vacuum perturbation, reproducing fig. 8.4 – the imaginary part is visually indistinguishable. The real part has a relative magnitude of about 10^{-14}, showing that deviations from zero are on the order of machine precision, thus we can regard them as numerical noise. Values are given in Gaussian units.

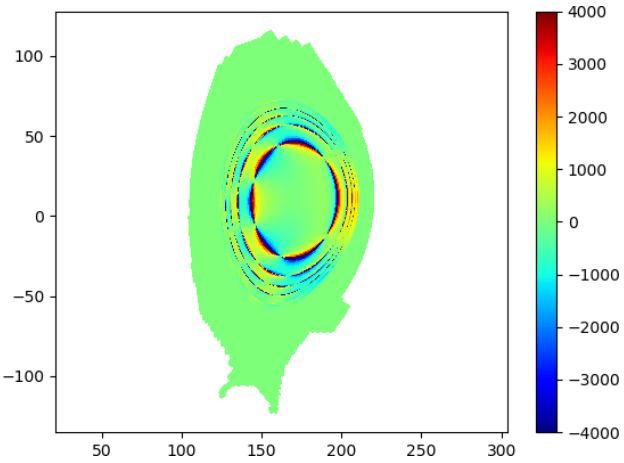

(a) Real part of response pressure p_n, taken from fig. 5 in [2].

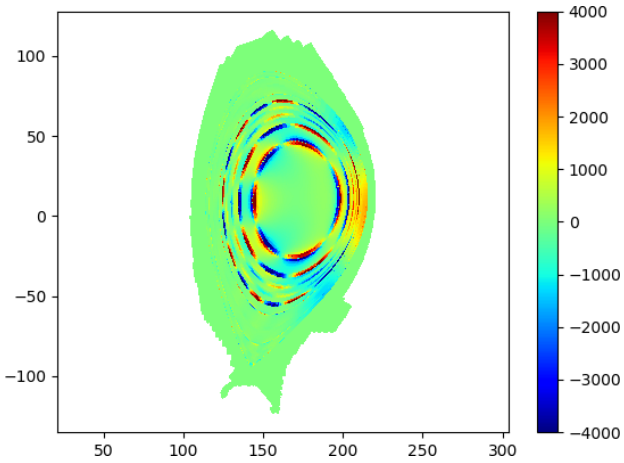

(b) Real part of response pressure p_n (reproduction).

Figure 8.6: Response pressure p_n for the resonant vacuum perturbation, comparing the result from [2] (left) to our reproduction (right). The positions of the resonances appear to agree; the visual difference in the width and color of the resonance may be due to different radial grid resolution. Values are given in Gaussian units.

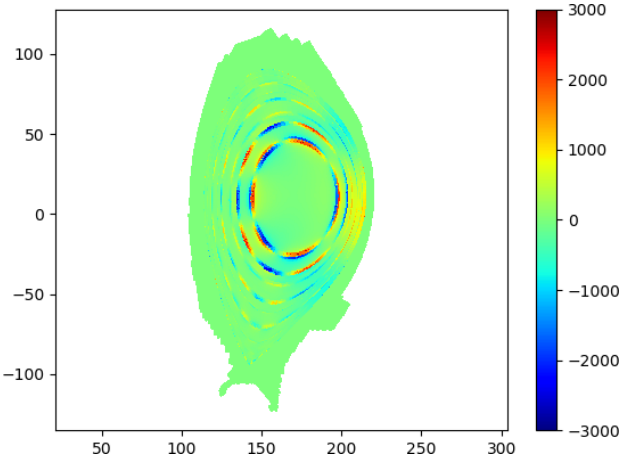

(a) Real part of response pressure p_n.

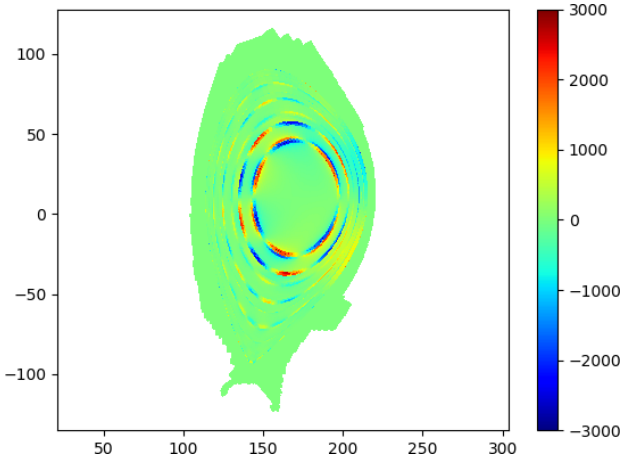

(b) Imaginary part of response pressure p_n.

Figure 8.7: Response pressure p_n after convergence of preconditioned iterations. Comparing the real part (left) to the real part of the initial pressure response (fig. 8.6), we see that the magnitude decreases after iterations. Comparing the imaginary part (right) to the imaginary part of the initial pressure response for the non-resonant test case (figs. 8.4b and 8.5b), we see that the gradient pattern is overshadowed by the much larger values at the resonant flux surfaces. Values are given in Gaussian units.

8.2 Convergence and Preconditioning

To estimate the convergence of the iterative scheme from section 2.1 and confirm the validity of the preconditioner from section 2.2, two low-density test cases shall be compared. For the low-density configuration, all eigenvalues λ of the iteration operator have absolute values less than one, so that convergence can be achieved without preconditioning – this is the first test case. For the second test case, the threshold $\lambda_{\max}$ of the preconditioner is set to a low value of 5×10^{-3}, so that a preconditioning matrix is constructed from eigenvalues above this threshold. This results in 4 eigenvalues, with the largest being $\lambda_1 \approx -0.09384 - 0.02109\mathrm{i}$. These two test cases are juxtaposed as en explicit test of the preconditioning algrorithm.

The quantity used for a comparison is the magnetic field perturbation $\delta\boldsymbol{B}$. To show convergence, the L^2 norm over the poloidal cross section is applied to this quantity for every iteration step k summarized in table 2.1:

$$\|\delta\boldsymbol{B}^{(k)}\|_2 = \sqrt{\int_\Omega |\delta\boldsymbol{B}^{(k)}|^2 \,\mathrm{d}\Omega}. \tag{8.6}$$

This allows us to assign a magnitude to the entire magnetic field, and indeed this quantity is proportional to the energy contained in the magnetic field. The L^2 norm after k iterations is expected to follow a geometric series of the largest eigenvalue, starting from the vacuum perturbation $\delta\boldsymbol{B}_\mathrm{v}$ for the "zeroth" iteration:

$$\|\delta\boldsymbol{B}^{(k)}\|_2 \approx |\lambda_{\max}|^k \|\delta\boldsymbol{B}^{(0)}\|_2. \tag{8.7}$$

When $\delta\boldsymbol{B}^{(k)}$ approaches machine precision, $\|\delta\boldsymbol{B}^{(k)}\|_2$ remains approximately constant and convergence is achieved. The results of these considerations can be seen in fig. 8.8. The preconditioned iterations converge faster, since the largest 4 eigenvalues are "removed" from the iterations.

To estimate any difference in the converged result depending on whether the preconditioner was used or not, the real part of the Z component of the magnetic field perturbation shall be compared as an example. As a reference for the orders of magnitude involved, fig. 8.9a shows the vacuum perturbation field $\delta\boldsymbol{B}_\mathrm{v}$, and fig. 8.9b shows the magnetic field $\delta\boldsymbol{B}_\mathrm{p}$ of the plasma response current for the high-density configuration. Both add up to the full magnetic perturbation field $\delta\boldsymbol{B}$, i.e., $\delta\boldsymbol{B} = \delta\boldsymbol{B}_\mathrm{v} + \delta\boldsymbol{B}_\mathrm{p}$. It can also be seen that $\delta\boldsymbol{B}_\mathrm{p}$ reaches the order of magnitude of $\delta\boldsymbol{B}_\mathrm{v}$ in some regions. In contrast, fig. 8.10a shows the magnetic field $\delta\boldsymbol{B}_\mathrm{p}$ of the plasma response current for the low-density test case with preconditioning. It is small compared to the plots in fig. 8.9, so a comparison between full perturbation fields is not feasible. Instead, fig. 8.10b depicts the *difference* between the result *with* preconditioner and the result *without* preconditioner. This suggests a relative error on the order of 10^{-6} and its magnitude is lower than the vacuum perturbation field by an order of 10^{-9}.

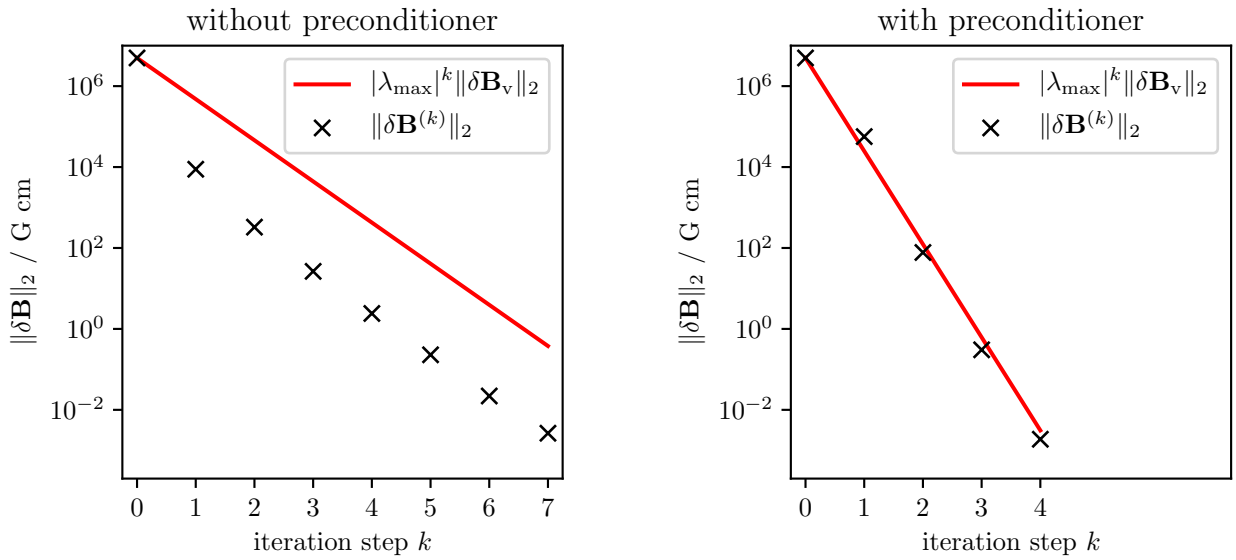

(a) Convergence estimation without preconditioner. $|\lambda_{\max}|$ refers to the largest eigenvalue $|\lambda_1| \approx 0.0962$.

(b) Convergence estimation with preconditioner. $|\lambda_{\max}|$ refers to the upper threshold of 5×10^{-3} the preconditioner considers.

Figure 8.8: Convergence estimation of low-density test cases. The quantity of interest is the L^2 norm of the magnetic field perturbation $\delta \boldsymbol{B}$ (see eq. (8.6)), which is proportional to the energy of the magnetic ffield and is plotted as black crosses. Its value after k iteration steps is expected to follow a geometric series of the largest eigenvalue $\lambda_{\max}$ (see eq. (8.7)), starting from the vacuum perturbation $\delta \boldsymbol{B}_\mathrm{v}$, which is plotted as a red line for comparison. While both test cases converge, the preconditioned test case needs fewer iteration steps k. Further iteration steps only change due to numerical noise and the norm stays approximately constant.

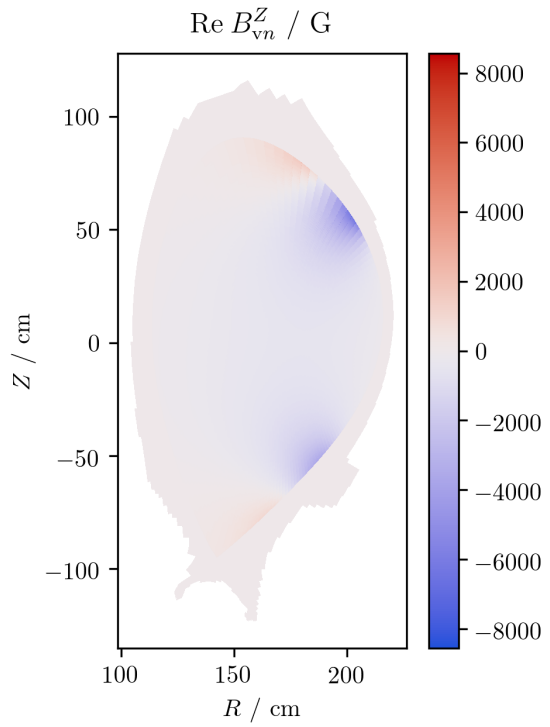

(a) Real part of the Z component of the vacuum perturbation $\delta \boldsymbol{B}_\mathrm{v}$.

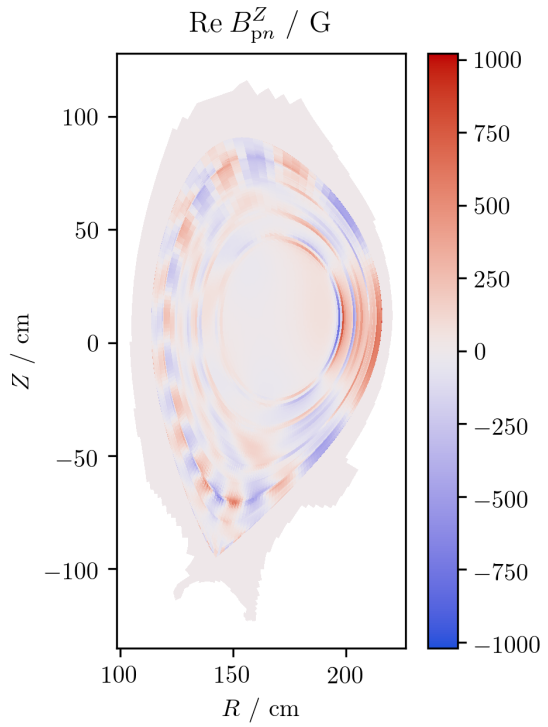

(b) Real part of the Z component of the magnetic field $\delta \boldsymbol{B}_\mathrm{p}$ of the plasma response current for the *high-density* test case.

Figure 8.9: Reference for the low-density test case in fig. 8.10, where the magnitude of the magnetic field $\delta \boldsymbol{B}_\mathrm{p}$ of the plasma response current is much smaller than for the high-density test case and the vacuum perturbation $\delta \boldsymbol{B}_\mathrm{v}$. The index n refers to the toroidal Fourier coefficient of the associated perturbation quantity, which is prefixed by δ. The colormap is chosen from [10].

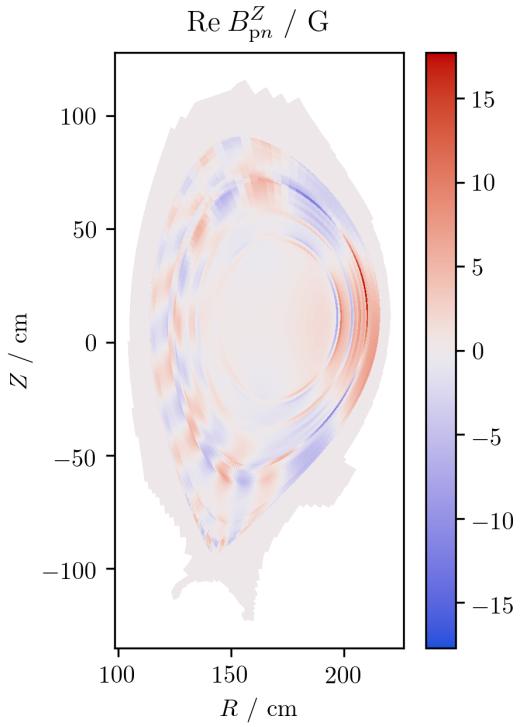

(a) Real part of the Z component of the magnetic field $\delta \boldsymbol{B}_\mathrm{p}$ of the plasma response current for the low-density test case *with* preconditioning.

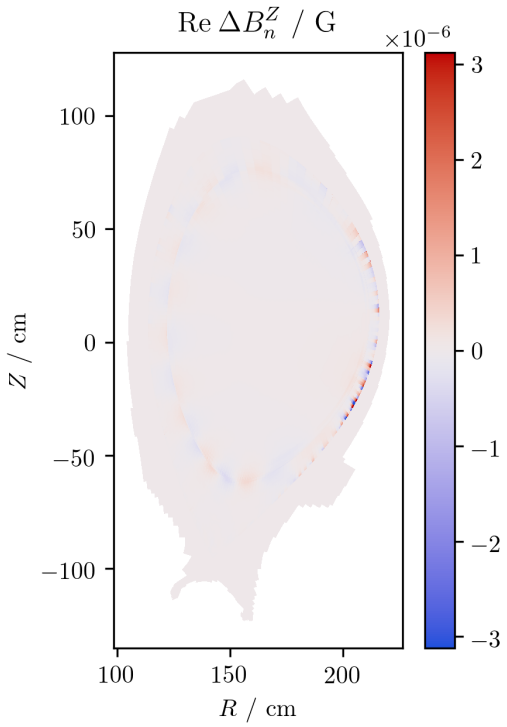

(b) Deviation $\Delta\delta \boldsymbol{B}_\mathrm{p}$ from fig. 8.10a when the preconditioner is not used. The relative error is on the order of 10^{-6}.

Figure 8.10: Effect of the preconditioner on the low-density test case. The magnetic field $\delta \boldsymbol{B}_\mathrm{p}$ of the plasma response current *with* preconditioning is compared to the *difference* to the result *without* preconditioner. This allows an estimation of the relative error. The index n refers to the toroidal Fourier coefficient of the associated perturbation quantity, which is prefixed by δ. The colormap is chosen from [10].

8.3 Resonances and Sheet Currents

After the validity of the initial pressure response and preconditioner have been established, these preconditioned iterations are now used on the high-density configuration to study the behaviour of the magnetic field at resonances, and the effects of sheet currents. For comparison with fig. 5 in [1], we utilize field line tracing for Fourier decomposition of poloidal modes in ϑ as per eq. (3.37). Note that the metric $\sqrt{g}$ is included in this quantity because it depends on ϑ. The quantity to be analyzed then is the weighted radial component $\sqrt{g}B^{\psi}_{mn}(\psi)$ of the magnetic field perturbation $\delta\boldsymbol{B}$, which has the dimension of magnetic flux because of the units of the basis vector $\boldsymbol{e}_{\psi}$ and the metric $\sqrt{g}$. We expect damping in the full perturbation $\delta\boldsymbol{B}$, which otherwise follows the vacuum perturbation $\delta\boldsymbol{B}_{\mathrm{v}}$. The radial flux variable ψ of the resonances are given by $m + nq(\psi) = 0$, where $n = 2$. We shall compare the results of the poloidal modes $m = \pm 3$, so the resonance is expected to occur where $q = \frac{3}{2}$, i.e., for negative m.

The effects of the sheet currents described in section 5.3 are also investigated in this context. One configuration omits sheet currents, and one configuration uses finite sheet currents. The constants C_{mn} from eq. (5.52) are arbitrarily set to

$$C_{32} = -1000, \tag{8.8}$$
$$C_{42} = 300 - 300\mathrm{i}, \tag{8.9}$$
$$C_{52} = -100 + 100\mathrm{i}, \tag{8.10}$$
$$C_{62} = -100 + 100\mathrm{i}, \tag{8.11}$$
$$C_{72} = -100 + 100\mathrm{i} \tag{8.12}$$

for the latter case, with all other coefficients set to zero. Due to mode coupling, changing one of these constants tends to affect more than one resonant flux surface. There is no constraint on the choice of the values in the given model apart from numerical stability.

Figure 8.11 shows the behavior at the resonance for the poloidal modes $m = \pm 3$ with and without sheet currents, respectively. Without additional sheet currents, the full magnetic field perturbation is increased at the resonance position instead of decreased. Thus, the addition of sheet currents is necessary to reproduce the expected behavior. Radial mesh refinement around resonant flux surfaces turns out to be crucial to capture the effects of these sheet currents.

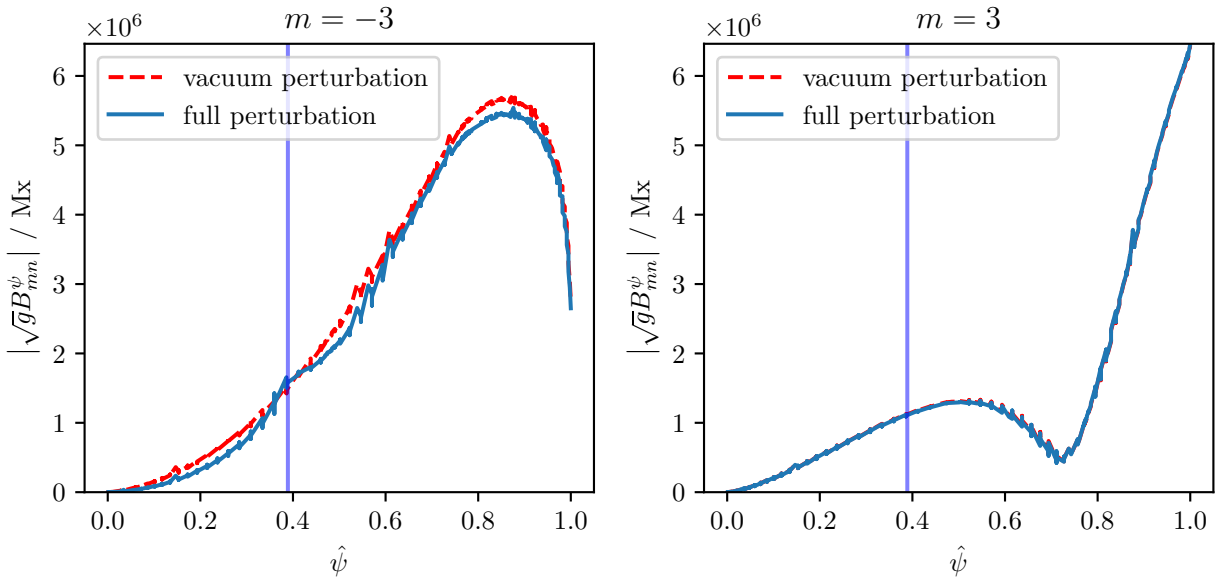

(a) Without sheet currents.

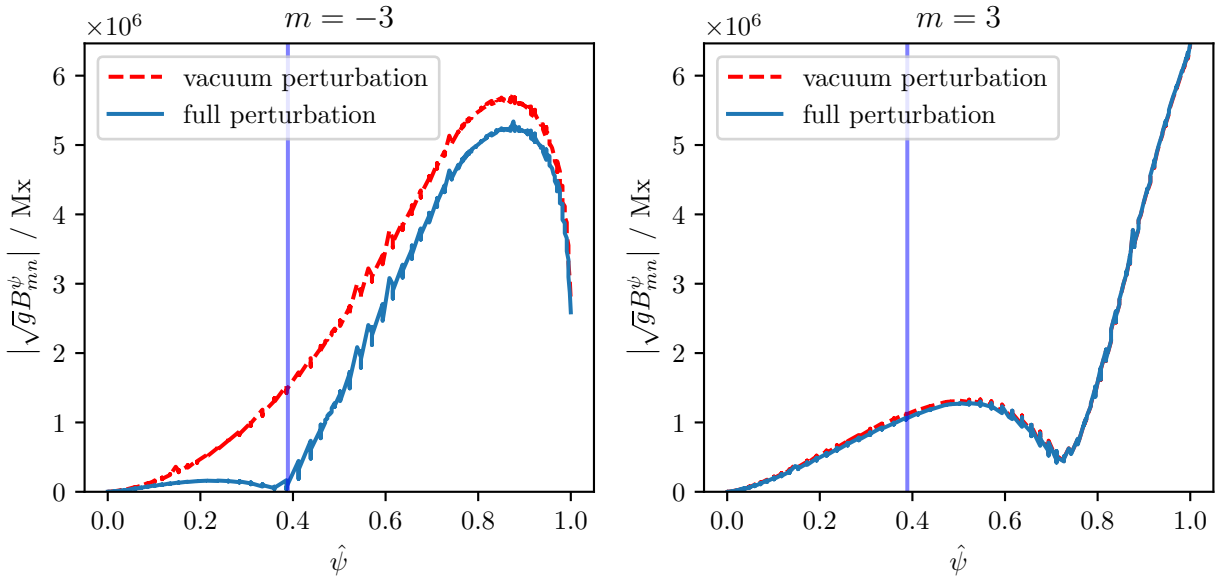

(b) With sheet currents.

Figure 8.11: Poloidal modes $m = \pm 3$ of the pseudoradial magnetic field perturbation $\sqrt{g}B^{\psi}_{mn}(\psi)$. $\hat{\psi}$ is the normalized flux ψ, used as a pseudoradial coordinate, so that $\hat{\psi} = 0$ at the magnetic axis and $\hat{\psi} = 1$ at the separatrix. The vertical line indicates the position where $q = \frac{3}{2}$, i.e., where the resonance is expected. In the test case without sheet currents (above), a slight increase of the full magnetic field perturbation can be seen at the resonance position for $m = -3$, compared to the vacuum perturbation. The test case with sheet currents (below) shows the expected damping of the full magnetic field perturbation by the sheet current at the resonance position for $m = -3$. The "ripples" in the graphs are a result of the field line tracing used to interpolate the angle ϑ: Many radial interpolation points are used per flux surface, but q is essentially a step function and stays constant between flux surfaces.

8.4 Large Aspect Ratio

The last test case is a comparison with KiLCA [8] results. The underlying geometry of the circular cross-section and the large aspect ratio is discussed in section 7.2. The grid is partitioned into $n_{\text{flux}} = 128$ flux surfaces. The scaling factor is set to $\gamma = 1000$, setting the major radius to $R_0 \approx 1.72\,\text{km}$. While superposition of poloidal modes is possible in both KiLCA and NEO-EQ code, only a single mode number $m = -4$ is used to construct the vacuum perturbation $\delta\boldsymbol{B}_{\text{v}}$ in order to avoid the effects of mode coupling in the toroidal geometry of NEO-EQ. In contrast to the case discussed in section 8.3, symmetry flux coordinates coincide with "common" cylindrical coordinates in this setup. Therefore, no field line tracing is necessary, and the discrete Fourier transform from eq. (7.52) is directly applied. Furthermore, the metric $\sqrt{g}$ does not depend on θ in this geometry, so it can be omitted as a constant factor. One low-density and one high-density configuration are simulated, and a single sheet current factor C_{42} for the given resonance is used, which is set to scale inversely with the ratio of the density of the two configurations.

The results of the NEO-EQ calculations are depicted in fig. 8.12 and are to be compared to the results from KiLCA in fig. 8.13. Damping occurs at the expected position, i.e., where $q = \frac{4}{2}$. While the low-density case in fig. 8.12a agrees well with the KiLCA result, the high-density case in fig. 8.12b displays a different shape around the resonance position, even though damping occurs at the resonance. This may be due to the neglect of bootstrap and inductive current in section 6.2 and will be studied in the near future.

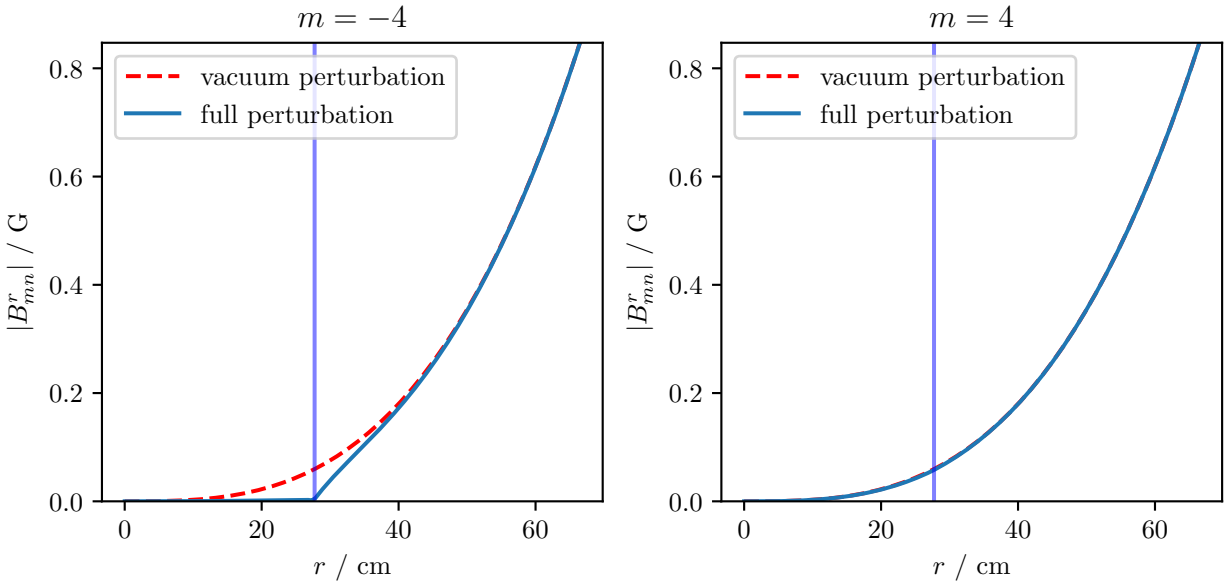

(a) Density at axis $n_{\text{axis}} = 5 \times 10^{11}\,\text{cm}^{-3}$, sheet current coefficient $C_{42} = -10^5 - 10^5\text{i}$.

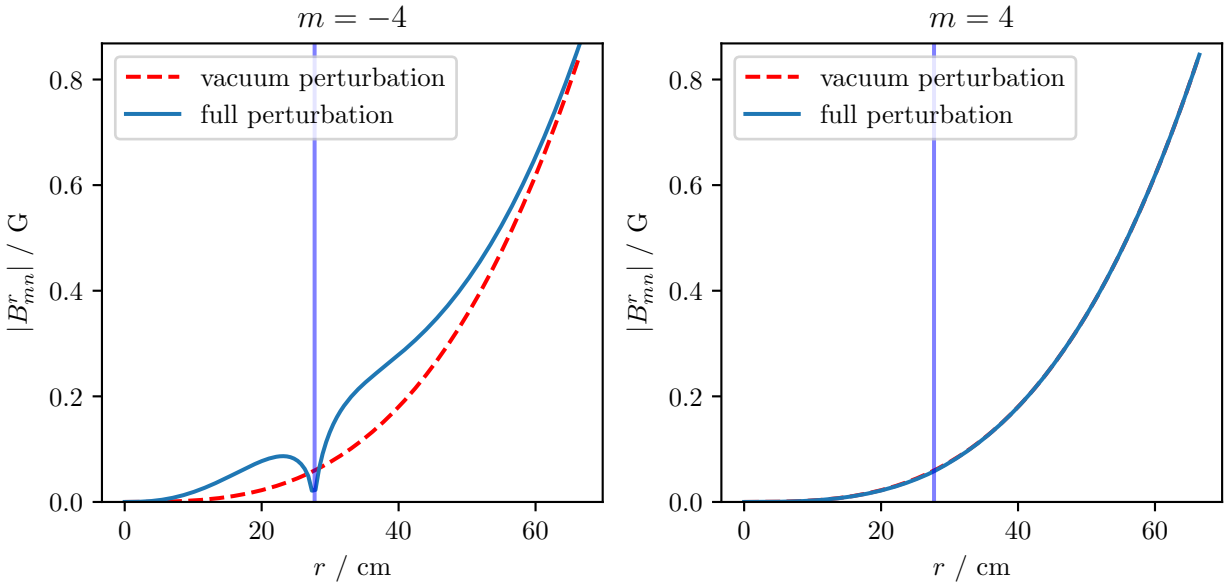

(b) Density at axis $n_{\text{axis}} = 5 \times 10^{13}\,\text{cm}^{-3}$, sheet current coefficient $C_{42} = -10^3 - 10^3\text{i}$.

Figure 8.12: Poloidal modes $m = \pm 4$ of the radial magnetic field $B^r_{mn}(r)$ for different central densities and sheet current factors, which is to be compared to the output of KiLCA [8] in fig. 8.13. The vertical line indicates the position where $q = \frac{4}{2}$, i.e., where the resonance is expected. While the low-density case (above) compares well to the KiLCA output, the high-density case (below) shows a markedly different shape around the resonance, even though shielding occurs at the expected position. r is the minor radius. Note that in contrast to fig. 8.11, the metric $\sqrt{g}$ is omitted, as it does not depend on θ due to the cylindrical geometry and is thus a constant factor.

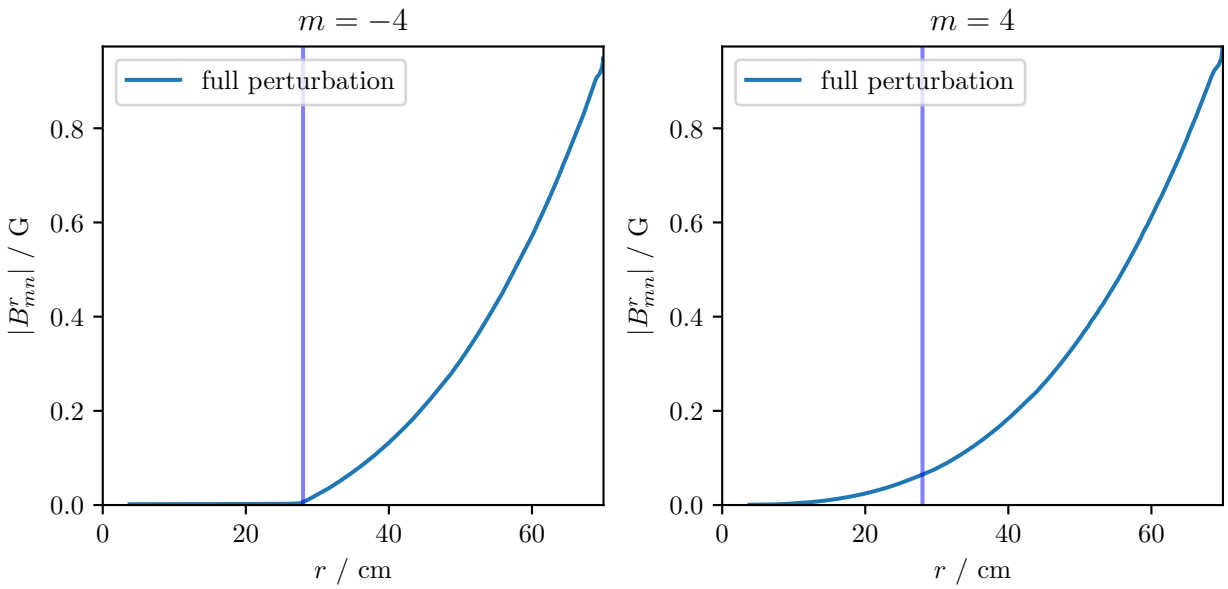

Figure 8.13: Poloidal mode $m = \pm 4$ of the radial magnetic field $B^r_{mn}(r)$, from KiLCA [8]. r is the minor radius. Note that in contrast to fig. 8.11, the metric $\sqrt{g}$ is omitted, as it does not depend on θ due to the cylindrical geometry and is thus a constant factor.

Chapter 9

Conclusion and Outlook

Over the course of this thesis, developed an iterative scheme (chapter 2) was developed to solve the linearized MHD force balance (chapter 5) and Ampère's equation (chapter 4) in a self-consistent manner. This is used to model the effects of a non-axisymmetric perturbation to an axisymmetric ideal MHD equilibrium (chapter 1). The symmetry in the toroidal angle of the tokamak device is taken into account (chapter 3) to simplify calculations. Two special configurations (chapter 7) were discussed for a comparison with previous publications. Selected results (chapter 8) demonstrate that the expected behavior of shielding by sheet currents can be reproduced at least qualitatively.

In the future, we intend to supplement kinetic code with results from these calculations, where the latter is used for accurate modeling of the effects that occur at resonant flux surfaces, while the former is used as a drop-in replacement for kinetic code away from resonant flux surfaces, as it is computationally less expensive. Furthermore, it may be used in conjunction with KiLCA code [8] to calculate the form factors discussed by Heyn et al. [7], in order to treat the effects of toroidal geometry more accurately. A combined model will be used for studies of the field penetration threshold in experimental conditions of ASDEX Upgrade.

Appendix A

Notational Conventions

In general, variables are printed in italic shape and constants in roman (upright) shape. Scalars are printed in normal weight, vectors are indicated by bold weight, matrices and operators by a hat, and tensors by sans-serif font. We only list symbols that appear in more than one chapter, or when they are used differently in different chapters. Symbols from appendix A.1 may appear decorated as listed in appendix A.2.

A.1 Base symbols

Notation	Description
$\hat{A}$	matrix applied to precondition iterations
$\boldsymbol{A}$	magnetic vector potential
$\boldsymbol{B}$	magnetic field strength, measured in Gauss
$\delta\boldsymbol{B}_\mathrm{p}$	perturbation field from *p*lasma current
$\delta\boldsymbol{B}_\mathrm{v}$	perturbation field in *v*acuum (from external coils)
C	arbitrary constant (of integration)
c	speed of light in centimetres per second
e	Euler's constant, base of natural logarithm
$\boldsymbol{e}$	basis vector
g	metric determinant
$\boldsymbol{h}_0$	unit vector of $\boldsymbol{B}_0$
i	imaginary unit, $\mathrm{i}^2 = -1$
$\hat{I}$	unit matrix
I	electric current
I_c	electric current produced by RMP *c*oils
$\boldsymbol{J}$	electric current density, measured in statampere
k_B	Boltzmann constant
$\hat{K}$	combined linear operator $\hat{M}\hat{P}$

Notation	Description
$\hat{K}$	stiffness matrix
l	length of edge
$\boldsymbol{l}$	edge vector in counter-clockwise direction
$\hat{M}$	linear operator representing computation of the magnetic field from the currents via Ampère's equation
m	poloidal mode number
N	dimension of system of linear equations
n	toroidal mode number
n	density of particles
$\boldsymbol{n}$	outward pointing normal vector
$\hat{P}$	linear operator representing computation of the currents from the magnetic field
p	pressure, measured in dyne per square centimetre
q	safety factor
R	radial coordinate in cylindrical coordinates
r	arbitrary point in a domain Ω
R_0	major radius of the tokamak
S	area in poloidal cross-section
$\boldsymbol{s}$	source term in systems of linear equations
T	temperature
Z	axial coordinate in cylindrical coordinates
Γ	border of a domain Ω, e.g. edge of a triangle
γ	scaling factor to approximate cylindrical geometry in toroidal geometry
δ_{ij}	Kronecker delta
ϑ	poloidal angle
λ	eigenvalue
ϱ	flux surface label
φ	toroidal angle
Ψ	magnetic flux
ψ	disc poloidal flux, used as flux surface label
Ω	domain of computation, e.g. a triangle

A.2 Symbol Decorations

Notation	Description
p_0	equilibrium p
δp	perturbation of p
p_n	FOURIER coefficient of perturbation of p with toroidal mode number n
p_{mn}	FOURIER coefficient of perturbation of p with poloidal mode number m and toroidal mode number n
$p^{(k)}$	k-th summand in series expansion of perturbed p / k-th degree of freedom of p in a particular loop
$p^{[k]}$	k-th partial sum in series expansion of perturbed p
$\boldsymbol{J}^{\text{pol}}$	poloidal component of $\boldsymbol{J}$
$\boldsymbol{J}^{\text{tor}}$	toroidal component of $\boldsymbol{J}$
$\boldsymbol{J}^{\parallel}$	component of $\boldsymbol{J}$ parallel to $\boldsymbol{B}_0$
$\boldsymbol{J}^{\perp}$	component of $\boldsymbol{J}$ perpendicular to $\boldsymbol{B}_0$
J^u	contravariant component of $\boldsymbol{J}$ w.r.t. coordinate u
J_u	covariant component of $\boldsymbol{J}$ w.r.t. coordinate u
$J_{(u)}$	physical component of $\boldsymbol{J}$ w.r.t. coordinate u
$\hat{\boldsymbol{n}}$	unit vector in direction of $\boldsymbol{n}$
$\boldsymbol{B}(\boldsymbol{r}^{(k)})$	$\boldsymbol{B}$ evaluated at node with index k
$\boldsymbol{B}(\Gamma_e^{(k)})$	$\boldsymbol{B}$ evaluated at midpoint of edge e of triangle k
$\boldsymbol{B}(\Omega^{(k)})$	$\boldsymbol{B}$ evaluated at weighted centroid of triangle k
$\langle\cdot\rangle$	flux surface average
$[\cdot]_{mn}$	FOURIER transform with poloidal and toroidal mode numbers
$\cdot^*$	complex conjugate

Appendix B

Arnoldi Iterations

For an $N \times N$ matrix $\hat{K}$, the Arnoldi algorithm gives the largest n_r Ritz eigenvalues λ_k and the associated eigenvectors $\boldsymbol{v}_k$ which span the Krylov subspace of $\hat{K}$. To accomplish this, $\hat{K}$ is repeatedly applied to an arbitrary initial vector $\boldsymbol{q}_1$. In each iteration step, the next Arnoldi vector $\boldsymbol{q}_k$ is generated and orthonormalized with respect to the previously generated vectors by Gram-Schmidt orthogonalization. Also, entries of an upper Hessenberg matrix $\hat{H}$ are constructed, as outlined in algorithm 1. Grouping together the $\boldsymbol{q}_k$ vectors in an $N \times n_r$ matrix

Algorithm 1 Arnoldi iterations

$\boldsymbol{q}_1 \leftarrow \frac{\boldsymbol{q}_1}{\|\boldsymbol{q}_1\|}$
for $k = 2, 3, \dots, n_r$ **do**
    $\boldsymbol{q}_k \leftarrow \hat{K}\boldsymbol{q}_{k-1}$
    for $j = 1, 2, \dots, k-1$ **do**
        $H_{j,k-1} \leftarrow \boldsymbol{q}_j^\dagger \boldsymbol{q}_k$
        $\boldsymbol{q}_k \leftarrow \boldsymbol{q}_k - H_{j,k-1}\boldsymbol{q}_j$
    end for
    $H_{k,k-1} \leftarrow \|\boldsymbol{q}_k\|$
    $\boldsymbol{q}_k \leftarrow \frac{\boldsymbol{q}_k}{H_{k,k-1}}$
end for

$\hat{Q}$, an approximation of $\hat{K}$ can be written out as

$$\hat{K} \approx \hat{Q}\hat{H}\hat{Q}^\dagger. \tag{B.1}$$

Diagonalization of $\hat{H}$ via the LAPACK routine `zhseqr` yields the Ritz eigenvalues λ_k and application of $\hat{Q}$ on the eigenvectors of $\hat{H}$ obtained via `zhsein` gives the eigenvectors $\boldsymbol{v}_k$ associated with $\hat{K}$.

Bibliography

[1] C G Albert, M F Heyn, S V Kasilov, W Kernbichler, A F Martitsch, A M Runov. "Kinetic modeling of 3D equilibria in a tokamak". In: *Journal of Physics: Conference Series* 775 (Nov. 2016), p. 012001. DOI: 10.1088/1742-6596/775/1/012001.

[2] C. G. Albert, M. F. Heyn, S. V. Kasilov, W. Kernbichler. "Kinetic modeling of plasma response to RMPs for a tokamak in full toroidal geometry". English. In: *45th EPS Conference on Plasma Physics, EPS 2018*. Vol. 2018-July. European Physical Society (EPS), Jan. 2018, pp. 709–712.

[3] Oszkár Bíró. "Variations- und Residuenmethoden in der Elektrotechnik". Lecture Notes at the Graz University of Technology. 2015.

[4] W.D. D'haeseleer, W.N.G. Hitchon, J.D. Callen, J.L. Shohet. *Flux Coordinates and Magnetic Field Structure. A Guide to a Fundamental Tool of Plasma Theory*. Springer Series in Computational Physics. Springer-Verlag, 1991.

[5] J.P. Freidberg. *Ideal MHD*. Cambridge University Press, 2014. ISBN: 9781107006256.

[6] F. Hecht. "New development in FreeFem++". In: *J. Numer. Math.* 20.3-4 (2012), pp. 251–265. ISSN: 1570-2820.

[7] Martin F. Heyn, Ivan B. Ivanov, Sergei V. Kasilov, Winfried Kernbichler, Ilon Joseph, Richard A. Moyer, Alexey M. Runov. "Kinetic estimate of the shielding of resonant magnetic field perturbations by the plasma in DIII-D". In: *Nuclear Fusion* 48.2 (Jan. 2008), p. 024005. DOI: 10.1088/0029-5515/48/2/024005.

[8] Martin F Heyn, Ivan B Ivanov, Sergei V Kasilov, Winfried Kernbichler. "Kinetic modelling of the interaction of rotating magnetic fields with a radially inhomogeneous plasma". In: *Nuclear Fusion* 46.4 (Mar. 2006), S159–S169. DOI: 10.1088/0029-5515/46/4/s07.

[9] Jianming Jin. *The Finite Element Method in Electromagnetics*. Second Edition. John Wiley & Sons, Inc., 2002.

[10] Peter Kovesi. *Good Colour Maps: How to Design Them*. 2015. arXiv: 1509.03700 [cs.GR].

[11] Lao. *G EQDSK FORMAT*. Feb. 1997. URL: https://w3.pppl.gov/ntcc/TORAY/G_EQDSK.pdf.

[12] O. Sauter, S.Yu. Medvedev. "Tokamak coordinate conventions: COCOS". In: *Computer Physics Communications* 184.2 (2013), pp. 293–302. DOI: 10.1016/j.cpc.2012.09.010.

[13] Florian Seeber. "Finite Element Method Applied to Magnetostatics in a Toroidal Domain with Open Boundary Conditions". Master's thesis. Institute of Theoretical and Computational Physics, Graz University of Technology, July 2018.

[14] F.L. Waelbroeck. "Theory and observations of magnetic islands". In: *Nuclear Fusion* 49.10 (Sept. 2009), p. 104025. DOI: 10.1088/0029-5515/49/10/104025.